UNIVERSITY OF CALIFORNIA SAN DIEGO

The release of bubbles and other small-scale processes at the ice-water boundary of marine-terminating glaciers

A dissertation submitted in partial satisfaction of the
requirements for the degree Doctor of Philosophy

in

Oceanography

by

Hayden Allen Johnson

Committee in charge:

Grant B. Deane, Chair
Michael J. Buckingham
Jamin S. Greenbaum
David Saintillan
Fiammetta Straneo

2025

The Dissertation of Hayden Allen Johnson is approved, and it is acceptable in quality and form for publication on microfilm and electronically.

University of California San Diego

2025

DEDICATION

I would like to dedicate this dissertation to my parents and grandparents, whose many years of hard work laid the foundation required for me to be able to pursue a Ph.D.

EPIGRAPH

The first rule of surfing is accept failure.

Ian Stokes

TABLE OF CONTENTS

LIST OF FIGURES

LIST OF TABLES

PREFACE

I would like to open with a remark about the motivation for studying small-scale processes at the ice-ocean boundary. While a telescopic introduction can explain in a few paragraphs how the specific focus of each of the three chapters of this thesis is related to big questions that matter to many people, it is not always obvious that the logic goes both ways. Spending time and resources to study small-scale processes at the ice-water boundary may result in an improvement of our understanding of those processes, and it may even be relevant to larger-scale changes that have tangible impacts on society. However, that does not guarantee that there are not more important aspects of the system, the study of which might better-serve our overall understanding, nor that the resources would not be better spent on something else entirely.

This tension is something that I personally have grappled with repeatedly over the course of my Ph.D. Spending years studying something that no one else has ever thought was worth investigating in detail, and that the average person may never even have thought of at all, naturally causes one to doubt the importance and significance of one's work, and wonder whether the time could have been put to better use. Ultimately I think that there is no magical answer for this anxiety. I do, however, take some solace in the fact that the problems of climate change, disappearing ice caps, and sea level rise are never going to be solved by a single Ph.D. thesis. The best that one scientist can hope to do in the face of such immense challenges is to chip away at them one publishable unit at a time. It is therefore my hope that each chapter of this thesis has made a small but measurable contribution towards something worthwhile.

ACKNOWLEDGEMENTS

I would like to acknowledge, first and foremost, my doctoral advisor and committee chair Dr. Grant B. Deane. His combination of a knack for storytelling with an unwavering commitment to scientific rigor has been a great inspiration to me, and his willingness to meet with me as often as I wanted should serve as an example for all academic advisors. I would also like to acknowledge the other members of my committee, Professor Michael Buckingham, Dr. Jamin Greenbaum, Professor David Saintillan, and Professor Fiammetta Straneo, for their continued guidance and support. Though his name does not appear on the list of committee members, Dr. Dale Stokes has in many ways served as an unofficial co-advisor throughout my time here, for which I am tremendously grateful. Professor Oskar Glowacki served as my mentor and companion during three seasons of fieldwork at the Polish Polar Station in Hornsund Fjord, Svalbard. His guidance and friendship improved the experience more than can be adequately described.

Much gratitude is also owed to the friendly and professional staff of the Polish Polar Station, without whom none of the research presented in this thesis could have been conducted. The International Partnership for Acoustic Monitoring of Glaciers has served as a reliable sounding board for ideas and wellspring of valuable feedback throughout my Ph.D. Their continued collaboration has resulted in the improvement of all of the work presented here. Finally, I would like to acknowledge my lab mates, the newly-minted Professor Elizabeth Reed-Weidner and Dr. Raymond Leibensperger III, for their unfailing friendship and support.

Chapter 1, with minor adjustments, is a full reprint of the material as it appears in EGU's *The Cryosphere* as "Brief communication: A technique for making in situ measurements at the ice–water boundary of small pieces of floating glacier ice", by H. A. Johnson, O. Glowacki, G. B. Deane, and M. D. Stokes. Chapter 2 is in preparation for submission to ASA's *Journal of the Acoustical Society of America* with H. A. Johnson, G. B. Deane, M. D. Stokes, O. Glowacki, M. Moskalik, M. Chitre, H. Vishnu, and C. Powell as co-authors. Chapter 3 is in preparation for submission to AGU's *Geophysical Research Letters* with H. A. Johnson, G. B. Deane, M. D.

Stokes, O. Glowacki, M. Moskalik, M. Chitre, and H. Vishnu as co-authors. The dissertation author was the primary investigator and author of all chapters.

VITA

2019	Bachelor of Science, Department of Physics University of Toronto
2020	Master of Science, Scripps Institution of Oceanography University of California San Diego
2025	Doctor of Philosophy, Scripps Institution of Oceanography University of California San Diego

PUBLICATIONS

Johnson, H. A., Glowacki, O., Deane, G. B., & Stokes, M. D. (2024). Brief communication: A technique for making in-situ measurements at the ice-water boundary of small pieces of floating glacier ice. *The Cryosphere, 18* (1), 265-272.

ABSTRACT OF THE DISSERTATION

The release of bubbles and other small-scale processes at the ice-water boundary of marine-terminating glaciers

by

Hayden Allen Johnson

Doctor of Philosophy in Oceanography

University of California San Diego, 2025

Grant B. Deane, Chair

The unifying theme of this thesis is the study of small-scale processes at the ice-water boundary of marine-terminating glaciers. The release of air bubbles from the melting ice into the water in particular is often, but not always, a common thread. Small-scale processes at this boundary have the potential to influence larger-scale behavior of the ice sheets, and, in the case of the release of bubbles, to also provide a useful tool with which to study other processes occurring at the boundary. Chapter 1 presents a technique for making in situ measurements at the ice-water boundary of small pieces of floating ice that has recently calved from a marine-terminating glacier. Chapter 2 presents theoretical and numerical modeling efforts to constrain the maximum

energy that can be radiated as sound by the bubbles released as glacier ice melts. Comparison with experimental data shows that this model does indeed provide an upper bound and explain some of the variability in the radiated sound of ice, which represents a step towards using passive acoustics as a tool to measure submarine melting. Chapter 3 presents measurements of the modification of the size distribution of bubbles that occurs during their release from the ice into the water. The results show that this modification can vary, with bubbles sometimes remaining largely intact upon their release into the water, while in other cases many of the bubbles in the ice are broken up into many smaller bubbles in the water. These results have implications for the influence of these bubbles in the water on submarine melting.

Introduction

Perhaps the most well-known consequence of climate change is the melting of the polar ice caps. As temperatures warm globally, and near the poles in particular, ice that is currently resting on land has the potential to flow into the ocean and melt (IPCC, 2021). In addition to causing changes in the local environment, this loss of ice contributes to global mean sea level rise, which is problematic for low-lying regions around the world (Nicholls and Cazenave, 2010). While technological innovations such as gravity anomaly measurements from Earth-orbiting satellites provide observations of the changes currently befalling the polar regions with remarkable resolution and accuracy (Chen et al., 2022; Velicogna, 2009), projecting the future of these changes remains a challenge, and there remains a great deal of uncertainty around the potential for the collapse of the ice sheets in particular (IPCC, 2021; Slater et al., 2020).

The ice sheets of Greenland and Antarctica are hundreds or thousands of kilometers across and kilometers thick, and the problem of sea level rise is global and felt on decadal timescales. It can therefore be easy to imagine that only processes that play out on similarly grand scales can have any relevance to efforts to understand and predict the behavior of these systems. On the contrary, part of what makes these problems so vexing is the interplay of processes occurring across scales, from the continental all the way down to the microscopic (Straneo and Cenedese, 2015; Rosevear et al., 2024).

As an example, consider the role of the millimeters-thick viscous boundary layer at the ice-water boundary in controlling heat flux from the water into the ice (Rosevear et al., 2022; Wells and Worster, 2008). Any doubt that processes on these small scales *can* influence this flux of heat, and therefore submarine melting, can be dispelled with a simple thought experiment.

Imagine replacing the millimeters-thick viscous boundary layer at the ice-water interface with a perfectly insulating layer. The result would be zero heat flux from the water into the ice, and therefore zero submarine melting, regardless of how much thermal energy is available in the water. While this scenario is obviously unrealistic and contrived, it nevertheless demonstrates that processes which alter the heat flux across the ice-water boundary layer have the potential to influence the behavior of marine terminating glaciers and ice sheets at larger scales. Of course, the question of whether, and when, mm-scale processes at the ice-water boundary layer actually *do* play a leading role in controlling the behavior of the larger-scale system is more difficult to answer.

The question of how to accurately measure and model heat flux and submarine melting at the ice-water boundary of tidewater glaciers in particular is an active area of research. Parameterizations developed within the last few decades (Jenkins et al., 2010; Jenkins, 2011; Hellmer and Olbers, 1989; Holland and Jenkins, 1999) have been hampered by the sparse availability of observational data. In recent years, new observational techniques have made it possible to probe the performance of these descriptions, and have often found that the real story of what is going on at small scales is more complicated than expected (Schmidt et al., 2023). The parameterizations that are in standard use in the literature have been shown to result in substantial underestimates of submarine melting in some cases at vertical termini of tidewater glaciers (Jackson et al., 2020; Sutherland et al., 2019), while at the same time overestimating submarine melting beneath Antarctic ice shelves (Davis et al., 2023).

There are many questions that need to be answered in order to improve upon our understanding of, and ability to model, the ice-water boundary of marine-terminating glaciers and ice sheets. This thesis does not answer all of them. Its unifying theme, however, is contributions to the study of small-scale processes at the ice-water boundary of these systems. Each chapter takes up this mantle in its own unique way.

Chapter 1 describes a methodology for obtaining in situ measurements at the ice-water boundary of growlers (small pieces of floating glacier ice roughly the size of a car). This allows

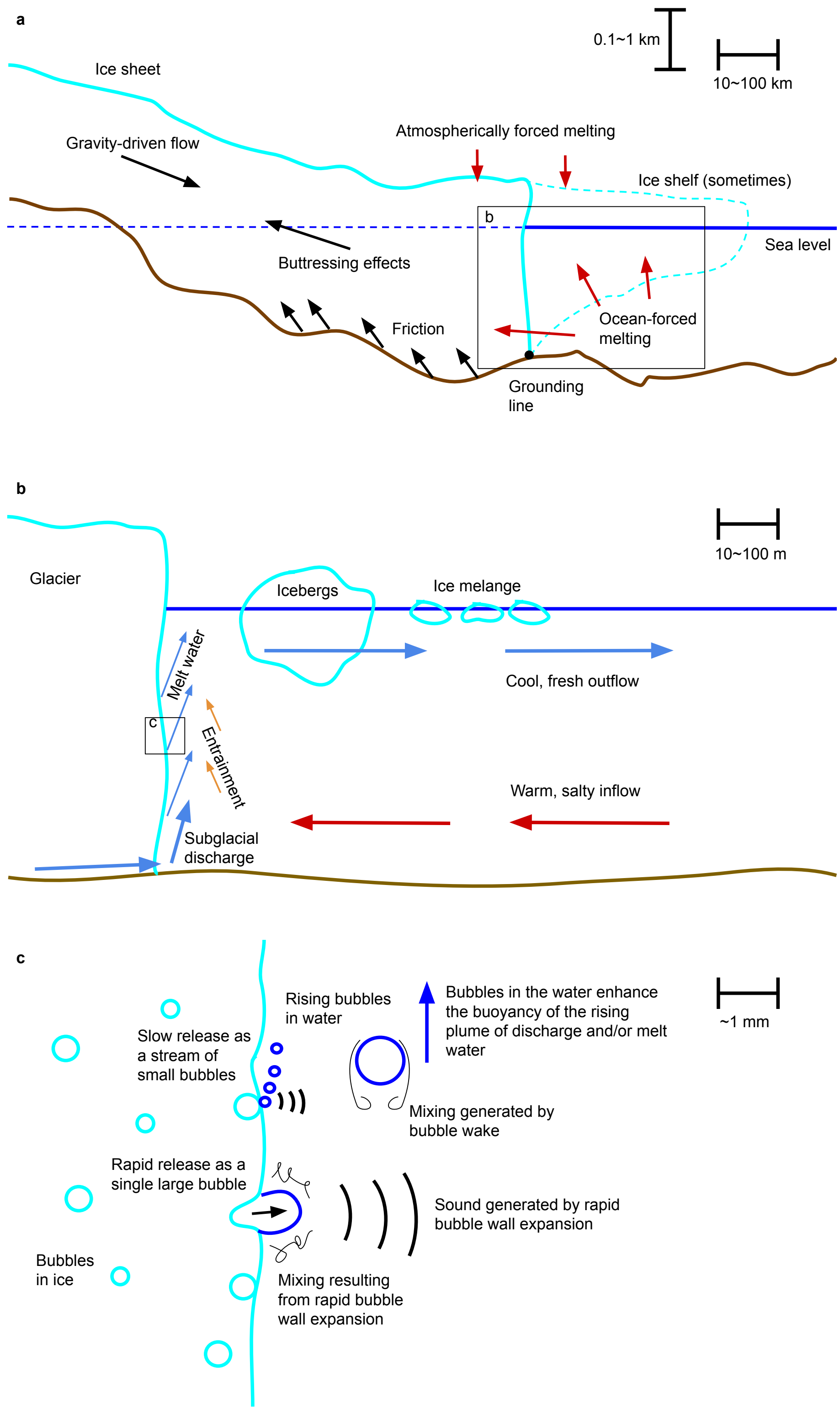

Figure 1. Illustration of the context for studying small scale processes at the ice-water boundary of marine-terminating glaciers and ice sheets.

the growlers to be used as a natural laboratory for the study of the ice-water boundary at the terminus itself, which is more realistic than can reasonably be achieved in a laboratory setting while avoiding the dangers and challenges of making in situ measurements at a submerged glacier terminus. Several examples of data collected with this method are presented, including cm-scale thermal gradients in the water, and synchronized underwater video and acoustic recordings of bubbles being released from the ice into the water.

Chapter 2 is a description of an attempt to answer a simple question about a process occurring at the ice-water boundary: how much sound is produced by the bubbles released from melting glacier ice? This work also represents one piece of a larger collective effort being undertaken by the International Partnership for Acoustic Observation and Monitoring of Glaciers to develop passive acoustics as a tool for measuring submarine melting. Such a tool would help improve our ability to measure submarine melting in a quasi-direct way, and therefore aid in efforts to understand, model, and ultimately predict the processes at play at glacial termini.

Chapter 3 addresses another simple question: what is the relationship between the size distribution of the bubbles in the ice and the size distribution of these bubbles once they have been released into the water? This work is motivated by recent findings that the presence of these bubbles enhances submarine melting at vertical tidewater glacier fronts, and by studies demonstrating that changes in the size distribution of bubbles rising through water can alter lateral heat transport. It turns out that, not only are acoustics a useful tool for answering the question of how the bubble size distribution is modified upon release into the water, but the total acoustic energy radiated by the ice is related to this transformation.

Chapter 1

A technique for making in-situ measurements at the ice-water boundary of small pieces of floating glacier ice

Abstract

This paper presents an apparatus and associated methods for making direct in-situ measurements of the ice-water boundary of small pieces of floating glacier ice. The method involves approaching ice pieces in a small boat and attaching a frame with instruments on it to them using ice screws. These types of measurements provide an opportunity to study small-scale processes at the ice-water interface which control heat flux across the boundary. Recent studies have suggested that current parameterizations of these processes may be performing poorly. Improving understanding of these processes may allow for more accurate theoretical and model descriptions of submarine melting.

1.1 Introduction

This paper presents an apparatus and associated methods for making in-situ measurements at the near ice-ocean boundary layer of small pieces of floating glacier ice (termed growlers). Here, the near ice-ocean boundary, or proximal boundary, refers to the region within 1 m of the ice surface. On these short scales, the behavior of the proximal boundary of growlers may be representative of other glacier ice-ocean boundaries subjected to similar forcing, such as the near-surface terminus of a glacier not subjected to plume forcing. The attention of this paper is restricted to vertical ice surfaces and is motivated by the role of the proximal boundary in melting glacier ice.

The proximal boundary consists of a solid-liquid interface, and the class of problems describing the diffusion of heat in a medium accompanied by a change of phase state are referred to as Stefan problems (Rubinštein, 1971). This particular Stefan problem is complicated by the presence of salt in the water, gas which moves from the ice into the water, and processes that play out across a wide range of scales, as shown in Fig. 1.1. Theoretical frameworks to describe the proximal boundary are an active area of research. Current theoretical descriptions are based on conservation of heat and salt at the ice-water interface (Hellmer and Olbers, 1989; Holland and Jenkins, 1999). This description is combined with buoyant plume theory to describe the effects of rising meltwater and, in the case of glacier termini, subglacial discharge water on the fluxes across the proximal boundary (Jenkins, 2011; Cowton et al., 2015; Slater et al., 2016). This framework is largely untested by direct observations (Straneo and Cenedese, 2015; Cenedese and Straneo, 2023), and does not include gas effects. A large number of laboratory experiments have been conducted to study processes occurring at the ice-water interface (McCutchan and Johnson, 2022). Many of these incorporate the effects of both heat and salt, but realistic effects of the pressurized bubbles present in glacier ice are difficult to reproduce in the laboratory. Wengrove et al. (2023) have suggested that processes related to the release of pressurized bubbles from the ice could impact the boundary layer and affect heat transport through the proximal boundary. Results from numerical modelling studies on the scale of the proximal boundary have shown general agreement with some laboratory studies in terms of the observed melt rates and the structure of the thermal and velocity boundary layers (Wells and Worster, 2011; Gayen et al., 2016), but neither the laboratory studies nor the numerical simulations include the effects of pressurized bubbles.

There are indications that the description of fluxes across the ice-water boundary currently in use need to be improved in order to allow for accurate estimates of submarine melt rates.

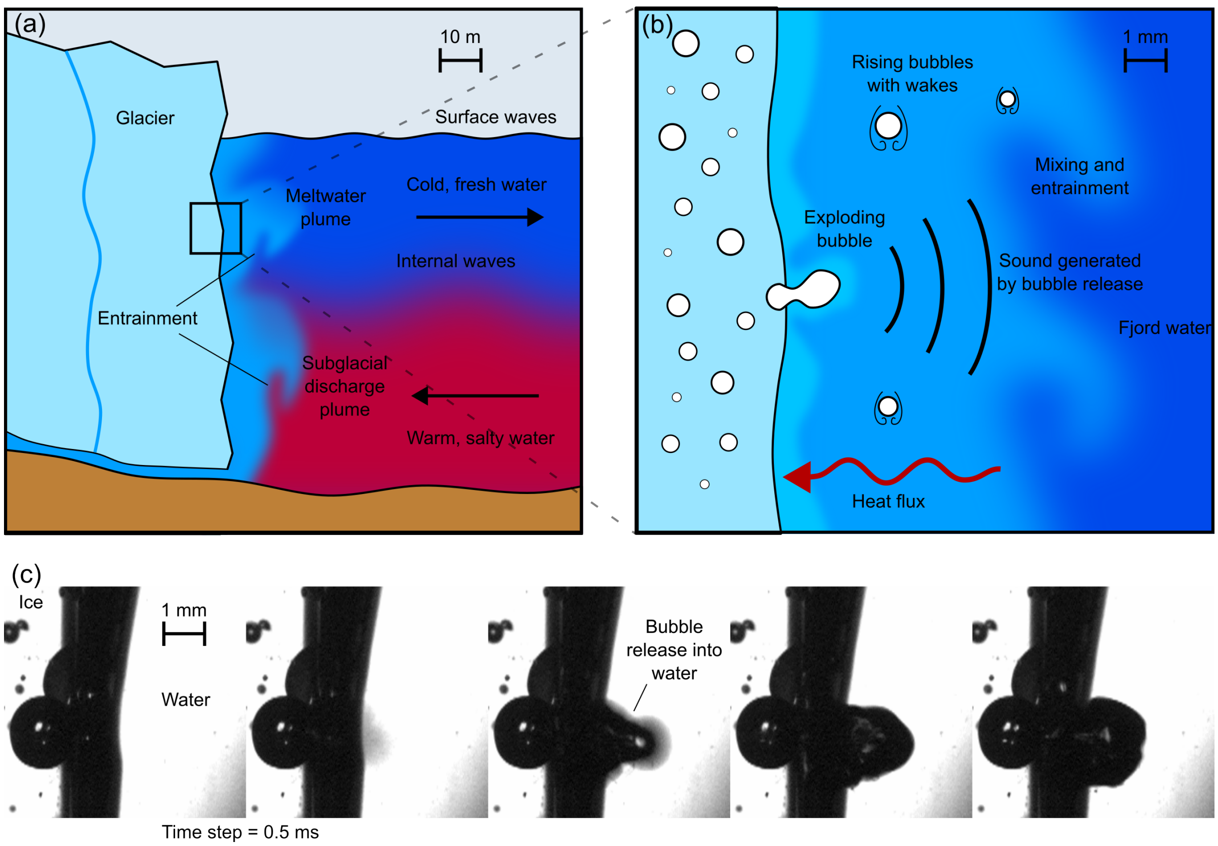

Figure 1.1. **a** A schematic of ice-ocean interactions at tidewater glaciers, including many processes that occur on scales of 10-100 m. These include subglacial discharge, water circulation in the fjord, and thermohaline structure. **b** An inset showing processes that occur within the proximal ice-water boundary, at scales ranging from roughly 0.1-100 mm. These include the release of air bubbles into the water, the rise of air bubbles through the water, and mixing within the proximal boundary. These smaller scale processes have the potential to control heat flux across the boundary and into the ice. **c** Still frames from high-speed video footage of a bubble being released from glacier ice in a laboratory experiment.

Recent observational studies comparing plume theory derived estimates of subglacial melting with direct observations of terminus ablation from acoustic surveys (Sutherland et al., 2019) and estimates of melting based on hydrographic data (Jackson et al., 2020) have suggested that the current theoretical framework underestimates submarine melting outside of subglacial discharge plumes. Laboratory studies have also indicated that the existing framework may perform poorly when water velocities are slower. Specifically, the existing framework implicitly assumes that the boundary layer thickness is governed by a shear instability, but at low flow speeds it may instead be controlled by a convective instability (McConnochie and Kerr, 2017).

Improving the description of fluxes across the ice-water boundary will require a combination of theoretical studies, laboratory experiments, and field observations. Several recent papers have suggested adjustments to the existing parameterizations in order to better match field observations (Jackson et al., 2022; Schulz et al., 2022). This is an excellent step, and should be supported by theoretical and laboratory studies. Direct observations of the proximal boundary at glacier termini are likely to remain elusive, due to the difficult and dangerous nature of conducting measurements near calving fronts of glaciers (Herrero, 2018). Recently, robotic vehicles have been used to make observations of water properties close to the termini of tidewater glaciers (Slater et al., 2018; Poulsen et al., 2022), or beneath floating ice shelves (Washam et al., 2023), but making measurements in the proximal boundary layer of vertical ice faces remains a challenge. Observations of the proximal boundary at small growlers can provide a natural laboratory, and a bridge to better understanding of the physical processes that may occur there. This paper describes an apparatus to make such observations, which we have termed “the ice frame”, and the associated methods for its use. It also briefly presents some example data that was collected using the ice frame.

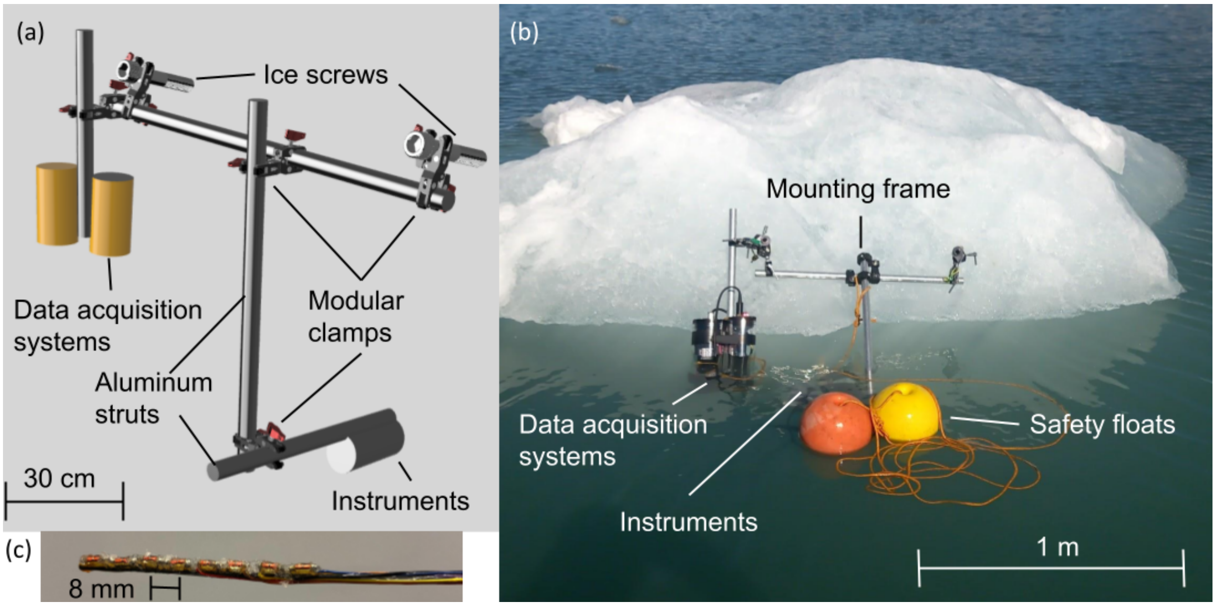

Figure 1.2. **a** A schematic of ice–ocean interactions at tidewater glaciers, including many processes that occur on scales of 10–100 m. These include subglacial discharge, water circulation in the fjord, and thermohaline structure. **b** An inset showing processes that occur within the proximal ice–water boundary, at scales ranging from roughly 0.1–100 mm. These include the release of air bubbles into the water, the rise of air bubbles through the water, and mixing within the proximal boundary. These smaller-scale processes have the potential to control heat flux across the boundary and into the ice. **c** Still frames from high-speed video footage of a bubble being released from glacier ice in a laboratory experiment.

1.2 Methods

1.2.1 Description of the ice frame

The ice frame consisted of a collection of aluminum tubes which could be fastened together using adjustable clamps. Ice screws were used to fasten the frame to a growler, and instruments could be attached to the frame using clamps and held within the proximal boundary. Figure 1.2a shows a schematic of the most successful configuration of the frame, and Fig. 1.2b is a picture of the frame deployed on a floating growler. Details of the specific hardware elements of the ice frame are given in Appendix A. A camera, hydrophone, and micro thermistor array were deployed on the frame. A detailed description of those sensors is given in Appendix B.

1.2.2 Design principles

There were four key principles that guided the design of the ice frame and the instruments deployed on it. First and foremost, the frame had to be simple to deploy. Attaching equipment to a piece of floating ice from a small boat is a difficult feat even in ideal conditions. Using only two ice screws, and placing them above the waterline, was key to keeping the frame deployment simple. Earlier iterations of the frame that included three or four points of contact with the ice, above and below the waterline, worked well during laboratory testing but proved to be too difficult to work with in the field. Second, the frame had to be adjustable in order to accommodate the natural variability in the surface of growlers. However, it also had to be easy to lock all of the moving parts into place once the frame was positioned correctly, in order to hold the instruments fixed relative to the ice face. Third, the frame, and instruments deployed on it, had to be sufficiently robust to hold up to inevitable bumping and banging during deployment and recovery. Finally, the components of the frame, and the instruments, had to be inexpensive and replaceable, because there was a non-trivial chance that the frame and any instruments on it could be damaged or lost during the deployment.

1.2.3 Deployment

The field campaign described here was conducted in Hornsund Fjord, Svalbard. The Polish Polar Station, which is located on the north side of the fjord near the mouth, was used as a base of operations for the duration of the campaign. The frame was deployed from a zodiac crewed by 2-3 people, on growlers that were floating in the water. Some of the growlers were in the bay of Hansbreen glacier, which is about 2 km northeast of the station, and others were near the northern shore of the main arm of the fjord, between the station and Hansbreen.

There were several criteria involved in the selection of growlers on which to deploy the frame, the most important being location. The chosen growler had to be a safe distance (at least a few hundred meters) from the glacier terminus and from any large icebergs, so that calving events or iceberg rolling or disintegrating would not pose a danger to the boat crew. It also had to be sufficiently far from shore that the boat would not be at risk of running aground. Attention had to be payed to the surface currents and wind, to predict whether a growler that was in a safe spot at the time of selection might move to an unsafe location over the expected duration of the deployment. Aside from safety concerns, it was also important to choose a growler that was fairly isolated, and not surrounded by thick melange or other growlers that would make navigating the boat difficult and could potentially damage the frame while it was deployed.

The other selection criteria were related to the size and shape of the growler itself. Deployment and recovery of the frame required the boat to be parked up against the growler for several minutes, with crew members leaning over the side of the boat holding it in position, fastening ice screws, and adjusting various elements of the frame. This involves an element of risk, which is exacerbated by the potential for floating ice to behave unpredictably, either rolling over or breaking apart. One way in which this risk was mitigated was by selecting growlers of appropriate size. The growler had to be large enough for the ice frame to fit onto it, and present an approximately vertical face extending at least a half a meter below the waterline and about 30 cm above it, but not so large as to pose a danger to the boat and crew in the event that it might suddenly break apart or roll over. The growlers that were selected were typically about 3-5 m in length and width, with a surface expression of about half a meter.

In addition to size, the geometry of the growlers played a role in the selection process. Growlers that were compact and looked sturdy were preferred over those that had protrusions or weak points that might have broken and caused sudden movement. Among growlers that seemed unlikely to break apart, it was also a priority to select those which seemed to be stable in the water, and not likely to roll over. This was assessed by observing the response of the growler to the ambient wave field, or to initial attempts to fasten ice screws to the growler.

Often it was useful to screw an extra ice screw into the growler initially to serve as hold to keep the boat in position while deploying the frame. The two ice screws to which the frame would be attached were then screwed into the ice. The instruments were attached to the frame and adjusted, based on visual estimation, to try to accommodate the geometry of the ice face to which the frame would be attached. The safety floats were fastened to the frame using a line. The frame was then lowered over the side of the boat, between the boat and the growler, and the crossbeam was attached to each of the two ice screws using pairs of SmallRig clamps. See Fig. 1.2 for a schematic and image of the frame.

Once the frame was successfully deployed, the boat would be moved some distance away (about 50-100 m) in order to minimize any unnecessary impacts on the environment that might influence the measurements, but would be kept close enough to monitor the growler and frame. The frame would be recovered in a similar manner to that in which it was deployed.

1.3 Results

1.3.1 Performance

As a mounting system, the ice frame has length, time, payload, and placement performance specifications. The frame is deployable on growlers ranging in size from 3-5 m across and provides access to the top 0.5-1 m of the ice-water interface. Instruments can be placed from the ice face up to about 0.5 m away. Under the conditions experienced during this field campaign, with air temperatures in the range of about 5-8 °C and water temperatures in the range of about 2-4 °C, and with ice screws of length 19 cm, the deployment time was limited to about 1-2 hours before melting around the ice screws would make the frame-to-growler connection unstable. This might be extended with longer screws or in colder temperatures. Practical experience with the frame and a boat suggests that payloads up to about 5 kg can be managed. Three different types of data were successfully collected using the frame: images of the ice face, acoustic recordings, and temperature array measurements. These are described in greater detail below. In principle, other types of data could also be collected using a similar apparatus, such as water salinity or flow speed, or the ablation of the ice face itself. The modular nature of the frame means that multiple instruments can be deployed at once, with the trade-off being increased weight and complexity.

1.3.2 Imaging of the ice face

The ice frame is well-suited to collecting direct-view images of the ice at close range. Using a camera mounted on the frame and positioned about 12 cm from the ice face, images of the ice face were successfully collected during this deployment. The camera resolution of about 25 um per pixel at the ice face (see Appendix 1.7.1 for camera specifications) was sufficient to resolve individual bubbles in the ice and in the water. It should be noted that, since the index of refraction for ice is much closer to that of water than to that of air, it is easy to view bubbles within the ice, but difficult to discern the ice-water boundary itself in direct-view images. A wider field of view could be obtained by mounting the camera further from the ice but this would create some difficulties: first, water clarity potentially becomes an issue, and second, the logistics of attaching a sensor to the frame increases in difficulty the further from the ice the sensor is.

Two still frames from the camera video data are presented in Fig. 1.3c and 1.3d. In panel c, the bubble annotated near the center of the frame is still fixed within the ice. In panel d, several frames later, it has been released into the water and has started to rise and move slightly to the right. The camera depth of field was very shallow, enabling an estimate of the size of objects which are in focus. The radius of this bubble was estimated to be 0.8 mm.

1.3.3 Acoustic recordings

The ice frame allowed the collection of acoustic data at close proximity to the ice face of a melting growler. (See Appendix 1.7.1 for instrumentation details.) Placing a hydrophone in such close proximity to the ice face allows for the clear identification of the pulses of sound released by individual bubbles of air as they are released from the melting ice. One difficulty that should be noted is that placing a hydrophone in such close proximity to the ice face results in absolute sound pressure levels that are too high for many off-the-shelf hydrophones to measure, resulting in clipped signals. Care needs to be taken to ensure that the sensitivity of the hydrophone and

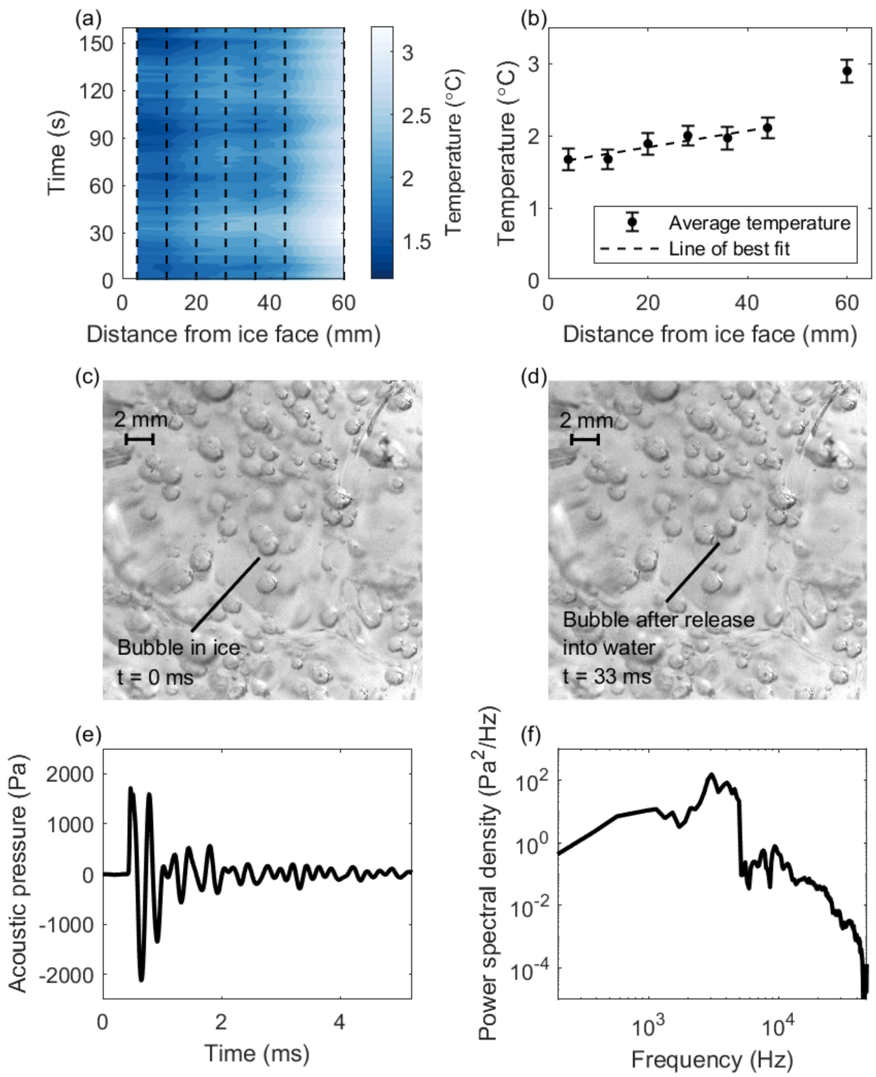

Figure 1.3. Example data collected using the ice frame. **a** Contour plot of the temperature observed in the proximal boundary of a floating growler, about 30 cm below the surface of the water. The x axis is distance from the ice face, and the position of individual thermistor elements is shown by the vertical dotted lines. **b** Average (circles) and standard deviation (bars) of the temperature measured at each thermistor for the data displayed in panel **a**. The linear least-squares fit to the first six elements (dashed line) has a slope of 0.01 mm $^{\circ}C^{-1}$. **c** Still frame from the underwater camera in which bubbles trapped in the ice are visible. **d** Another still frame from 33 ms later, just after the annotated bubble has been released from the ice. **e** Recording made by the hydrophone of the acoustic pulse released by the bubble shown in panels **c** and **d**. **f** Power spectrum of the acoustic signal shown in panel **e**, which has a broad peak centered around 4 kHz.

recording system is not too high. The hydrophone used in this study had a sensitivity of -208 dB re 1 Vrms per μPa, and it was used with no pre-amplifier.

The video and acoustic data were collected at the same time and the data streams were synchronized, allowing for the identification of bubbles visible in the video data in the acoustic record. The acoustic pulse emitted by the bubble seen in Fig. 1.3c and 1.3d is shown in Fig. 1.3e. The power spectrum of this pulse is presented in Fig 1.3f, and displays a broad peak centered around 4 kHz. This is roughly consistent with the expected natural frequency of 3.9 kHz of a bubble of radius 0.8 mm, based on the formula derived by Minnaert (1933).

1.3.4 Temperature measurements

The ice frame allowed for the successful collection of in-situ measurements of water properties in the proximal boundary. Using an array of calibrated thermistors (see Appendix 1.7.2 for details), the profile of the water temperature orthogonal to the ice face of a floating growler about 30 cm below the surface was measured over a span of about 20 minutes. A contour plot of a subset of this temperature data is shown in Fig. 1.3a. There is some temporal variability that may be related to wave action or changes in water flow past the ice face, but in the absence of any additional measurements, it is difficult to determine the cause or nature of these variations. It is also possible that these fluctuations could be caused by small motions of the frame and the sensors relative to the growler. Nevertheless, the overall thermal structure observed is quite consistent, as shown by Fig. 1.3b. The gradient across the 6 sensors nearest to the ice face is 0.01 °C mm^{-}1, with a steepening outside of this region. The temperature at the sensor 4 mm from the ice face is in excess of 1.5 °C, implying that the temperature gradient must be substantially greater within the first few mm of the ice face, since the temperature of the interface itself should be almost 0 °C.

1.4 Discussion and conclusions

The ice frame allows for direct in-situ measurements at the ice surface, and in the water up to about 0.5 m from the ice, at floating growlers. There are obvious differences between the ice-ocean boundary at floating growlers and at a glacier terminus, such as the vertical scale of the ice wall and the potential presence of subglacial discharge plumes. However, some of the physical processes and dynamics on sub-meter scales may be common between the two environments. These may include the release of air bubbles into the ice, or other processes that modulate heat flux within the proximal boundary. Floating growlers may therefore be an effective natural laboratory that can be used to study ice-ocean interactions at these scales, with relevance to glacial termini. This boundary is more realistic than one that can be recreated in the lab with artificial ice, and also more easily accessible than the terminus itself.

The study of floating ice in glacial bays is also consequential in its own right. This ice can play an important role in controlling conditions in glacial fjords (Davison et al., 2020). Understanding small-scale processes that modulate the interaction of floating ice with water in the fjord can aid understanding of the fjord-scale influence of floating ice.

Extension of the ice frame, or similar apparatuses, to allow for deployment at the terminus itself, and at greater depths below the surface, is a natural future direction of research. The risk of calving icebergs means that any such deployment will need to be carried out with uncrewed robotic vehicles. Uncrewed vehicles have been used recently to conduct surveys near glacial termini (Slater et al., 2018), but not to make measurements within the proximal boundary itself. Making these types of measurements is challenging, but may be necessary for the effort to accurately describe fluxes and melting at the termini of tidewater glaciers.

1.5 Acknowledgements

We would like to thank Meri Korhonen for her assistance with data collection in the field, and Christian Powell for his help with fabrication of ice frame components. We would also like to thank the members of the summer 2022 Polish Polar Station expedition. This research has been supported by the National Science Centre, Poland (grant no. 2021/43/D/ST10/00616), Ministry of Science and Higher Education of Poland (subsidy for the Institute of Geophysics, Polish Academy of Sciences), and the US Office of Naval Research (grant no. N00014-21-1-2304 and N00014-21-1-2316).

This chapter, with minor adjustments, is a full reprint of the material as it appears in EGU's *The Cryosphere* as "Brief communication: A technique for making in situ measurements at the ice–water boundary of small pieces of floating glacier ice", by H. A. Johnson, O. Glowacki, G. B. Deane, and M. D. Stokes. The dissertation author was the primary investigator and author of this paper.

1.6 Appendix A: Frame design

The ice frame consisted of several components, each of which is identified in Fig. 1.2a. The main structure was made up of hollow cylindrical aluminum tubes. The tubes were 75 cm long with a 1 inch outer diameter and 0.065 inch wall thickness. The tubes were held together with two different types of clamps. Off-road light bar mounting brackets, manufactured by Mosleyz, were used for joints that did not need to be adjusted in the field. Pairs of SmallRig Super Clamps, fastened to either end of a 3/8" stainless steel threaded rod, were used for connections that needed to be made or adjusted during the deployment process. Two Petzl 19 cm ice screws were used to fasten the frame to the ice. Finally, a pair of flotation spheres were used to prevent the frame from sinking. Marine grease was used to lubricate and protect any corrosion-sensitive elements, such as nuts, bolts, and threaded rods. When disassembled, the entire frame fit into a single Zarges box of dimensions 0.8 x 0.4 x 0.4 m. The total weight of the frame and instruments together was about 5 kg, which was sufficiently light as to be manageable for deployment by hand over the side of a small boat. The total cost of the frame hardware was about US$ 300, with the single most expensive component being the ice screws.

To deploy the frame, the ice screws were first screwed into the growler face about 20 cm above the waterline, with a horizontal separation of about 60 cm. A horizontal crossbeam was then attached to both screws with pairs of adjustable SmallRig clamps. A vertical beam with a length of 75 cm was fastened to this crossbeam at a right angle using the Mosleyz bar mounting brackets, and extended down below the surface of the water. The instruments were attached to the bottom of this vertical beam using pairs of adjustable SmallRig clamps. Since the top of the vertical beam was fastened to the cross beam within 5-10 cm of the ice, as long as the ice face was roughly vertical the force of gravity would act to pull the instruments down and in towards the ice. In some cases, the instruments themselves formed the third point of contact with the ice face. In other cases, an additional aluminum tube was connected to the bottom of the vertical beam and formed the third point of contact with the ice face, and the instruments were either attached to this tube or to the vertical beam. The flotation spheres were tied to one end of a 5-10 m long rope, with the other end tied to the main structure of the frame.

1.7 Appendix B: Instruments

1.7.1 Hydrophone and camera

An underwater camera and a hydrophone were used to make coincident optical and acoustic observations of air bubbles being released from the ice. The camera was a GoPro Hero 5, modified using a Back-Bone lens adapter and a Schneider 17 mm lens. A resolution of 1080p and framerate of 120 frames per second were used. A Voltaic V25 USB battery pack was used to extend the battery life of the GoPro. The camera and the battery pack were contained in a 4-inch diameter watertight enclosure from Blue Robotics. The total cost of the camera assembly and enclosure was about US$ 1000. The enclosure was attached to the bottom of the vertical beam of the frame using a SmallRig clamp on one end of a threaded rod, with the other end screwed into a plate which was mounted to the back end of the enclosure using Blue Robotics enclosure clamps. A pair of wooden rods were fastened to the sides of the enclosure, extending out past the front face to the focal plane of the camera, which was about 12 cm beyond the front face of the enclosure. When the frame was deployed on a growler, the rods would rest against the submerged ice face and hold the camera an appropriate distance from the ice face such as to place it within the focal plane of the camera. A GoPro Smart Remote was used to turn the camera on and start recording before putting the frame in the water, allowing the watertight enclosure to remain sealed.

An AS-1 hydrophone, from Aquarian Scientific, was used to make acoustic recordings at close proximity to the ice face. The sensitivity of the AS-1 hydrophone was -208 dB re 1 V per μPa. The hydrophone was mounted on one of the wooden standoff rods, about 7 cm from the ice face. The hydrophone cable was cut to a length of about 2 meters and spliced to an Impulse underwater connector. The recording system for the hydrophone consisted of a Tascam DR40-X handheld recorder, with a unity-gain, high-impedence buffer between the hydrophone output and the Tascam input. The recording system was housed in a 3-inch diameter Blue Robotics watertight enclosure. An external switch was connected to an Adafruit Feather microcontroller which emulated a Tascam RC-10 remote control (see github repository https://github.com/abbrev/tascam-rc-10-remote), allowing the Tascam to be turned on and start recording without opening the enclosure. The total cost of the hydrophone, recording system, and enclosure was about US$ 1000. The video and audio data from the camera and hydrophone were synchronized by starting recording of both instruments, then placing the hydrophone in the field of view of the camera and tapping it.

1.7.2 Thermistors

Another instrument configuration that was successfully deployed during this campaign was a thermistor array. The array consisted of 8 individual MF58 3950B 10 kΩ glass-encapsulated thermistors. The thermistors were glued to a 2 mm diameter carbon fiber rod. A silicone spacer about 2 mm thick was placed between the rod and each thermistor in order to help isolate the elements from the thermal mass and conductivity of the rod. AWG 30 wires were soldered to the ends of the thermistors. A common ground wire, and 8 signal wires, ran from the array to a Blue Robotics watertight enclosure containing the acquisition electronics. The exposed solder joints of the array were coated with polyurethane and then silicone in order to make the array waterproof. The data was recorded by an Adafruit Feather microcontroller, using two ADS1115 16-bit 4-channel analog-to-digital converters. For each channel, the output of a voltage regulator was connected by a 27.2 kΩ resistor to the appropriate analog-to-digital input, which was then connected to one of the resistor signal wires. The total cost of the thermistor array and housing was about US$ 500.

During deployment, the thermistor array was fastened to the bottom of the vertical beam of the frame using a pair of SmallRig clamps. The array was positioned to extend out from the frame towards the growler, perpendicular to the ice face. An aluminum rod was also connected to the bottom of the vertical beam, extending out towards the ice face but at an angle of about 20 degrees below horizontal. The rod and array were adjusted such that the rod would support the weight of the frame against the ice, while the array would just barely touch the ice face.

The Steinhart-Hart equation was used to compute the estimated temperature of each thermistor given the measured resistance. The optimal parameters for each individual element were determined by calibrating the array against an RBR Solo temperature logger. The array and the RBR Solo were both placed in a well-mixed bucket of seawater. This was done repeatedly with water temperatures ranging from about -1 °C to 10 °C in increments of about 0.5 °C. The computed temperature of each array element using the Steinhart-Hart equation was then fit to the "true" temperature measured by the RBR Solo using linear regression.

Chapter 2

Potential energy of air bubbles in glacier ice and its conversion into acoustic energy

Abstract

Air bubbles in glacier ice are released into the water and may generate sound as the ice melts. A major missing link in the study of this sound is an estimate of the sound energy radiated per unit of ice that melts. We present a theoretical upper bound for the sound energy that can be produced by the bubbles by computing their acoustically available potential energy. A more stringent upper bound based on a simple model for the behavior of the bubble upon release from the ice is then developed. These theory and model-based estimates are then compared to the results of experiments conducted with glacial ice collected from Hornsund Fjord, Svalbard. We find that the acoustic energy radiated by the melting ice in these experiments is less than the potential energy and the modeled maximum energy. However, we also find that there is substantial variability in the sound generated by the ice that is not explained by differences in the potential energy of the bubbles. We present some evidence that suggests this is a result of variation in the way in which individual bubbles are released, with bubbles that burst out suddenly generating more sound than those that escape gradually.

2.1 Introduction

The ice that makes up glaciers, ice sheets, and the icebergs that calve from marine-terminating glaciers contains many tiny bubbles of compressed air (Bader, 1950; Scholander and Nutt, 1960; Gow, 1968, 1971). When melting of the ice occurs beneath the surface of the water, the bubbles contained in the ice are released into the water. This process results in the production of underwater sound (Urick, 1971; Lee et al., 2013; Pettit et al., 2015; Glowacki et al., 2018; Deane et al., 2019; Zeh et al., 2018). Understanding this sound is important for two reasons.

First, the sound produced by melting glaciers influences the underwater soundscape of their environments. Glacial fjords and other regions near marine-terminating glacier and ice sheets can be important habitats for marine mammals that use sound to navigate and communicate. In the northern hemisphere, for example, this includes bearded seals (Lydersen et al., 2014). Noise generated by melting glacier ice is concentrated in the spectral band of $1-3$ kHz (Glowacki et al., 2018; Pettit et al., 2015), which overlaps with the vocalizations of some of the marine mammals present in these environments (Risch et al., 2007). The presence of melt noise in the soundscape, and changes to the soundscape resulting from changes in the acoustic emissions of melting glaciers, may therefore impact these marine mammals. Human activities that rely on underwater acoustic communication near marine-terminating glaciers may also be sensitive to melt noise.

Second, the noise generated by submarine melting could be a useful tool to study the melting itself. Submarine melt is difficult to measure directly, and observational studies generally infer submarine melt rates from observations of other variables (Straneo and Cenedese, 2015). However, recent studies have demonstrated that indirect estimates of submarine melt rates may be substantial underestimates (Sutherland et al., 2019; Jackson et al., 2020). The acoustic emissions of melting ice have the potential to be used to measure submarine melting (Deane et al., 2019), and provide an additional tool to measure submarine melting more precisely.

There is a great deal that is already understood about melt noise. The mechanism for the sound production has been identified to be bubbles being driven into breathing-mode oscillations upon their release from the ice (Urick, 1971). More recently, it has been demonstrated in observations that increased melting likely corresponds to elevated underwater sound levels in glacial fjords (Pettit et al., 2015; Vishnu et al., 2025). Observations of melting icebergs have shown that they do not radiate sound evenly in all directions (Glowacki et al., 2018). Observations in a glacial fjord with a vertical line array showed that the underwater sound field in a glacial bay has vertical directionality consistent with emission of sound from the submerged terminus and icebergs (Vishnu et al., 2020). The generation of sound due to melting has also been found to vary with depth (Vishnu et al., 2020, 2023). Similarly, Wengrove et al. (2023) suggested that the energy available from bubbles released from the ice to mix water near the ice-water boundary may vary with depth. Finally, it has been shown that bubbles can be released from the ice rapidly or slowly, and produce more sound if they are released rapidly (Grossman et al., 2024).

Recently, Vishnu et al. (2025) provided a mathematical framework for relating the sound produced at the terminus of a glacier with the sound level at a receiver some distance away. In general terms, the sound power $\mathscr{P}$ at the receiver, as a function of angular frequency ω and receiver position $\mathbf{r_0}$, is given by

$$\mathscr{P}(\omega,\mathbf{r_0}) = \int_{A_T} M(\mathbf{r})\mathscr{N}(\mathbf{r})S(\omega,\mathbf{r})|G(\omega,\mathbf{r},\mathbf{r_0})|^2 d\mathbf{r}. \tag{2.1}$$

Here, A_T is the area of the glacier terminus, $\mathbf{r}$ is position on the terminus, $M(\mathbf{r})$ is the melt rate, $\mathscr{N}(\mathbf{r})$ is the number of bubbles per unit volume of ice, $S(\omega,\mathbf{r})$ is the source spectrum of sound emitted by bubble releases, and $G(\omega,\mathbf{r},\mathbf{r_0})$ is the Green's Function describing propagation through the water between the terminus and receiver. Vishnu et al. (2025) outline the calculation of the Green's Function G in detail, and provide a more sophisticated description of this formulation.

In the context of this existing literature, a key question that remains to be answered is: quantitatively, how much sound is produced per unit of ice that melts? Or, in terms of Eq. 2.1, what is $\mathscr{N}S$? Previous results (Glowacki et al., 2018; Vishnu et al., 2023; Grossman et al., 2024) suggest that the answer is unlikely to be simple and universal. Nevertheless, having an estimate of this quantity is an essential step towards doing quantitative science with melt noise. Understanding the variability in the sound produced per unit ice is also crucial, even for applications which only seek to track changes in the total noise level in the environment.

This paper develops estimates for an upper bound on the acoustic energy radiated by melting glacier ice, and presents analysis of some laboratory measurements of this acoustic energy. Section 2.2 begins with an analysis of the potential energy stored in the bubbles in glacier ice. An estimate of this energy provides an estimate of a firm upper bound on the sound that can be emitted by melting ice. Section 2.3 then presents a simple model for the behavior of bubbles upon their release from ice, based on existing equations describing bubble oscillations and sound generation. This model offers some insight into the way in which the sound radiated by a bubble released from the ice can vary depending on the bubble properties and the timescale of its release, and provides a way to calculate a more stringent upper bound on the sound energy radiated by melting ice. Section 2.4 describes an experiment conducted with blocks of glacier ice collected from a glacier fjord. Section 2.5 presents comparisons of the theoretical limits on the acoustic energy described in Sections 2.2 and 2.3 with measurements made during the experiments. Finally, 2.6 presents a discussion of some implications of the upper bounds on the sound generated by melting glacier ice.

2.2 Calculation of gas potential energy in ice bubbles

The purpose of this section is to present a mathematical framework describing the energy stored in compressed gas bubbles in ice. Specifically what is of interest here is the energy that is available for the generation of sound, which we term the "acoustically available potential energy", though it shall often be referred to here simply as potential energy for the sake of brevity. We begin by defining the potential energy of a single bubble in Section 2.2.1. We then discuss the simplification and associated error introduced by neglecting the effects of surface tension in Section 2.2.2. Finally, we outline the calculation of the total potential energy of bubbles in a finite volume of ice in section 2.2.3.

2.2.1 Potential energy of an individual bubble

Consider an air bubble trapped in ice which is submerged beneath the surface of a body of water. If the ice melts and its face recedes beyond the location of the bubble, the bubble will be released into the water. We define the acoustically available potential energy, ϕ, of a bubble confined in ice to be the energy available to do work on the environment as the bubble expands to reach its equilibrium radius in the water. The units of ϕ are J. (Note that all variables and their units are listed in Tables 2.1 and 2.3, while all physical constants and their units and values are listed in Table 2.2.)

In order to compute ϕ, imagine starting with a bubble trapped in ice, removing it from the ice entirely, and then allowing it to expand in a controlled manner. The potential energy ϕ can then be computed as the work done by the bubble during its expansion. We make several simplifying assumptions:

1. The bubble is always spherical with radius R;
2. The pressure in the bubble p is uniform everywhere inside the bubble;
3. The vapor pressure of water inside the bubble is negligible;
4. The gas inside the bubble obeys a polytropic law, so pv^{κ} is constant for some polytropic index κ, where $v = \frac{4}{3}\pi R^3$ is the bubble volume;
5. Changes in the bubble radius occur in a quasi-static regime, such that forces related to viscosity and acceleration of the bubble wall can be neglected.

Suppose that the bubble within the ice has initial internal pressure $p = p_0$ and radius $R = R_0$. As the bubble expands in the water, the polytropic law can be used to express the bubble pressure p as a function of its radius R according to Eq. 2.2,

$$p = p_0 \left(\frac{R_0}{R}\right)^{3\kappa}. \tag{2.2}$$

When the bubble is surrounded by water, the pressure inside the bubble p will also be equal to the pressure on the liquid side of the bubble wall p_L plus the pressure due to surface tension,

$$p = p_\mathrm{L} + \frac{2\sigma}{R}, \tag{2.3}$$

where $\sigma = 0.076$ N m^{-1} is the approximate surface tension of water at 0 °C and with salinity in the range 0-35 g kg^{-1} (Nayar et al., 2014, 2016).

Once the bubble reaches equilibrium in the water, the pressure on the liquid side of the bubble wall will equal the hydrostatic pressure in the water, $p_\mathrm{L} = P_\infty$. Equation 2.3 can then be used to write the equilibrium pressure of the bubble as

$$p_\mathrm{eq} = P_\infty + \frac{2\sigma}{R_\mathrm{eq}}. \tag{2.4}$$

The equilibrium radius of the bubble R_eq will itself depend upon the equilibrium pressure, and Eq. 2.2 and Eq. 2.4 can be combined to obtain the relation

$$R_\mathrm{eq} = R_0 \left(\frac{p_0}{P_\infty + \frac{2\sigma}{R_\mathrm{eq}}}\right)^{\frac{1}{3\kappa}}. \tag{2.5}$$

In practice, Eq. 2.5 can be evaluated iteratively, with R_0 as the initial guess for R_eq, and this procedure requires very few iterations to converge satisfactorily. The equilibrium pressure can then be computed from Eq. 2.4.

The force acting on the water as a result of the presence of the bubble is given by the integral of the pressure on the liquid side of the bubble wall, p_{L}, over the surface of the bubble,

$$F = \oint p_{\mathrm{L}} dS = p_{\mathrm{L}} 4\pi R^2. \tag{2.6}$$

The work done by the bubble on the environment as it expands will then be the integral of this force,

$$\phi = \int_{R_0}^{R_{\mathrm{eq}}} p_{\mathrm{L}} 4\pi R^2 dR. \tag{2.7}$$

Making use of Eq. 2.2 and Eq. 2.3 and integrating results in the following expression for ϕ:

$$\phi = \begin{cases} \frac{4\pi R_0{}^3 p_0}{3(\kappa-1)} \left(1 - \left(\frac{R_0}{R_{\mathrm{eq}}}\right)^{3(\kappa-1)}\right) - 4\pi\sigma({R_{\mathrm{eq}}}^2 - {R_0}^2) & \text{if } \kappa \neq 1, \\ \frac{4}{3}\pi R_0{}^3 p_0 \ln\left(\frac{R_{\mathrm{eq}}}{R_0}\right)^3 - 4\pi\sigma({R_{\mathrm{eq}}}^2 - {R_0}^2) & \text{if } \kappa = 1 \end{cases} \tag{2.8}$$

(see Appendix 2.9 for a detailed derivation). As written in Eq. 2.8, ϕ depends on the properties of the bubble in the ice p_0 and R_0, as should be expected. It also depends on the equilibrium radius of the R_{eq}, which must be computed using Eq. 2.5, making ϕ an implicit function of the water hydrostatic pressure P_∞.

The appropriate value of the polytropic index κ depends on the ratio of the timescale of expansion of the bubble to the timescale of heat transfer across the bubble wall. If the expansion of the bubble to its equilibrium radius occurs much faster than the transfer of heat between the bubble and the water, then the expansion is effectively adiabatic. The appropriate choice in this case is $\kappa = \gamma$, where γ is the ratio of heat capacity at constant pressure to heat capacity at constant volume ($\gamma = 7/5$ for diatomic gases such as air). If the expansion of the bubble occurs much more slowly than the transfer of heat between the bubble and the water, then the expansion will be effectively isothermal. The appropriate choice in this case is $\kappa = 1$. The actual value will fall somewhere in the range $1 \leq \kappa \leq 7/5$, and may vary for varying bubble sizes. The results presented in Fig. 1 of Prosperetti (1977) suggest that an effective polytropic index of $\kappa = \gamma = 7/5$ is likely appropriate for the bubbles considered in this paper, which have radii in the

Table 2.1. Variables I.

Symbol	Units	Description
ϕ	J	Potential energy of a single bubble
Φ	J	Potential energy of all bubbles in a finite volume of ice
p_0	Pa	Initial pressure inside a single bubble encased in ice
p	Pa	Pressure inside an oscillating bubble in the water
p_{eq}	Pa	Pressure inside a single bubble at equilibrium
P_0	Pa	Average internal pressure of the bubbles inside a piece of ice
P_∞	Pa	Far-field, hydrostatic pressure in the water away from the bubble
R_0	m	Initial radius of a bubble in ice
R	m	Radius of an oscillating bubble in the water
R_{eq}	m	Radius of a bubble once it reaches equilibrium
t	s	Time
τ	s	Timescale of release of a bubble trapped in ice
κ	$-$	Polytropic index
$\mathscr{V}$	m^3	Volume of ice
$\mathscr{N}$	Count	Number of bubbles contained in a finite volume of ice
V_0	m^3	Total volume of bubbles contained in a finite volume of ice

range of $0.03 - 7$ mm. It is worth noting that we do not expect the choice of κ to substantially impact the results presented in this paper. For pressure ratios in the range of $1 < p_0/P_\infty < 20$, $\phi|_{p_0/P_\infty}$ varies by at most a factor of 2 as κ is varied in the range of $1 \leq \kappa \leq 7/5$. This factor of 2 turns out to be small relative to the uncertainty in our experimental data and the natural variability in the potential energy.

It should be noted that in neither the adiabatic nor isothermal case is the acoustically available potential energy ϕ representative of the true total potential energy of a bubble, because we have not accounted for the exchange of heat between the bubble and the environment. The absence of heat exchange in the adiabatic case $\kappa = \gamma$ means that the temperature of the bubble will decrease during the expansion and its final temperature when it reaches mechanical equilibrium will be less than that of the surrounding water. The bubble will eventually come to thermal equilibrium with its surroundings, and as it warms it will extract energy from the environment in the form of heat. It will also do additional mechanical work on the water as it expands further as a result of this warming. The total mechanical work done on the water after the bubble has

Table 2.2. Physical constants.

Symbol	Value	Units	Description
c	1490	m s^{-1}	Speed of sound in sea water
g	9.8	m s^{-2}	Acceleration due to gravity
p_{atm}	101325	Pa	Atmospheric pressure at sea level
γ	$\frac{7}{5}$	–	Ratio of heat capacity at constant pressure to heat capacity at constant volume for air
σ	0.076	N m^{-1}	Surface tension of water at 0 °C and salinity of 0-35 g kg^{-1}
ρ	1025	kg m^{-3}	Density of sea water

reached this final thermal equilibrium should be equal to the expression for ϕ with $\kappa = 1$. While the isothermal case includes the additional mechanical work done on the environment due to heat flux into the bubble, it does not include the energy lost from the environment as a result of this heat flux. If one were interested in the total energy for purposes other than the generation of sound, then a proper accounting of the heat flux would need to be included, but this lies beyond the scope of this work.

The two terms present in Eq. 2.8 each have a distinct physical meaning which can be understood. The first term, proportional to $p_0 v_0$ (where $v_0 = \frac{4}{3}\pi {R_0}^3$ is the initial bubble volume), is the total energy available due to the expansion of the gas in the bubble. The second term, proportional to surface tension σ and the change in surface area of the bubble, is the energy that goes into overcoming surface tension as the bubble expands, and is therefore not available to the environment.

Finally, we would like to comment on the possibility for Eq. 2.8 to give negative values for the potential energy. This occurs when $R_{eq} < R_0$, which implies that $p_{eq} < P_\infty + 2\sigma/R_0$. The physical interpretation of this would be that the bubble is compressed upon exposure to the higher pressure in the water, with the water therefore doing work on the bubble. For a free bubble in the water, this initial compression would drive the bubble into oscillation just as an initial expansion would, which would generate sound. However, a model of bubble contraction with no influence from the ice is even less realistic than our model of instantaneous bubble release from the ice. We therefore advise against the extension of Eq. 2.8 for values of $R_{\mathrm{eq}} < R_0$. At grounded glaciers, the ice overburden pressure, which at a given depth is given by the weight of the ice above this depth, should always be greater than the hydrostatic pressure in the water, so we expect that cases where $R_{\mathrm{eq}} < R_0$ should be relatively rare.

2.2.2 Effect of neglecting surface tension

Equation 2.8 for the potential energy of an individual bubble can be simplified by neglecting the effect of surface tension. Setting $\sigma = 0$ in Eq. 2.3 gives $\tilde{p}_{\mathrm{L}} = p$, which results in the elimination of the second term in Eq. 2.8 (the tilde is used to indicate a quantity computed with surface tension neglected). Setting $\sigma = 0$ in Eq. 2.4 and 2.5 gives $\tilde{p}_{\mathrm{eq}} = P_\infty$ and $\tilde{R}_{\mathrm{eq}} = R_0(p_0/P_\infty)^{\frac{1}{3\kappa}}$. This allows the potential energy with surface tension neglected, $\tilde{\phi}$, to be written directly in terms of the water hydrostatic pressure P_∞:

$$\tilde{\phi} = \begin{cases} \frac{v_0 p_0}{\kappa - 1}\left(1 - \left(\frac{P_\infty}{p_0}\right)^{\frac{\kappa-1}{\kappa}}\right) & \text{if } \kappa \neq 1, \\ v_0 p_0 \ln\left(\frac{p_0}{P_\infty}\right) & \text{if } \kappa = 1. \end{cases} \tag{2.9}$$

The error introduced by neglecting surface tension is generally small, and inversely proportional to the initial bubble radius R_0. However, the error can become arbitrarily large as the pressure differential between the bubble and the water approaches the pressure due to surface tension, $p_0 - P_\infty \to 2\sigma/R_0$. This effect is illustrated in Fig. 2.1. For the pieces of ice analyzed in this study, the overall effect of neglecting surface tension is negligible, but this may not be true in general.

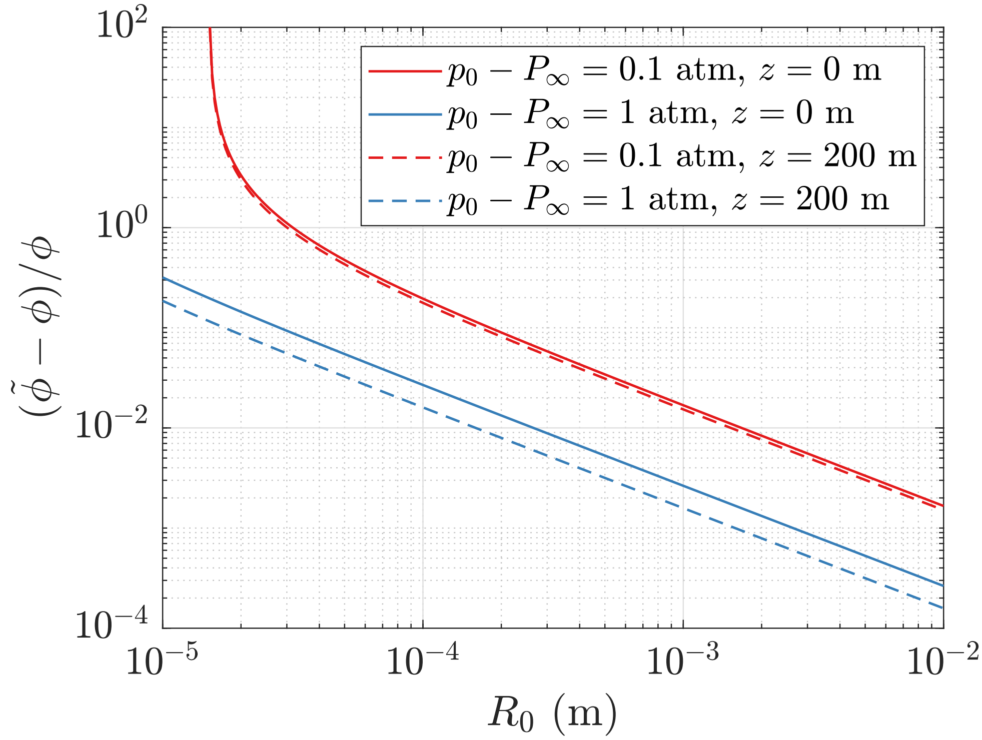

Figure 2.1. Relative error in the bubble potential energy ϕ introduced by neglecting surface tension as a function of bubble radius. The relative error is computed as $(\tilde{\phi}-\phi)/\phi$. The results are plotted for two different pressure differences $p_0 - P_\infty$, indicated by different colors. For each of these pressure differences, the results are plotted for two different depths beneath the water surface z, indicated by solid or dashed lines.

2.2.3 Potential energy in a finite volume of ice

We now consider the total potential energy of all bubbles contained within a finite volume of ice $\mathscr{V}$. This total can be computed as the sum of the individual bubble energies,

$$\Phi = \sum_{i=1}^{N} \phi(R_{0,i}, p_{0,i}), \tag{2.10}$$

where i is an index and N is the total number of bubbles contained within the volume $\mathscr{V}$. If the joint probability distribution of the pressures and radii of bubbles in a volume of ice is known, Φ can be written as an integral,

$$\Phi = \mathscr{V}\mathscr{N} \iint \phi(p_0, R_0)\mathbf{P}(p_0|R_0)\mathbf{P}(R_0)dp_0 dR_0, \tag{2.11}$$

where $\mathscr{N}$ is the number density of bubbles per unit volume, $\mathbf{P}(R_0)$ is the probability density that a bubble has radius R_0, and $\mathbf{P}(p_0|R_0)$ is the conditional probability density of a bubble with radius R_0 having pressure p_0.

Equation 2.11 is an exact expression for the total potential energy Φ. In practice, its utility is limited by the fact that the joint probability distributions of p_0 and R_0 are generally not known. However, by making several simplifying assumptions, it is possible to obtain simple closed-form expressions for Φ.

First, neglecting surface tension allows for the simplification of Eq. 2.8 to Eq. 2.9 for $\tilde{\phi}$, as discussed in Section 2.2.2. Second, we assume that the distributions of bubble radius and pressure are independent of one another. This assumption is consistent with the observations of Scholander and Nutt (1960) from Greenlandic icebergs. With this assumption, the two integrals in Eq. 2.11 can be separated. Defining the total volume of bubbles contained in the volume of ice $\mathscr{V}$ to be

$$V_0 = \sum_{i=1}^{N} v_{0,i} = \mathscr{V}\mathscr{N} \int v_0 \mathbf{P}(R_0)dR_0, \tag{2.12}$$

Φ is proportional to V_0 and an integral over the distribution of bubble pressures p_0,

$$\Phi = \begin{cases} \frac{V_0}{\kappa-1} \int p_0 \left(1 - \left(\frac{p_0}{P_\infty}\right)^{\frac{1-\kappa}{\kappa}}\right) \mathbf{P}(p_0) dp_0 & \text{if } \kappa \neq 1, \\ V_0 \int p_0 \ln\left(\frac{p_0}{P_\infty}\right) \mathbf{P}(p_0) dp_0 & \text{if } \kappa = 1. \end{cases} \tag{2.13}$$

In order to evaluate Eq. 2.13, we need to assume a distribution of bubble pressures $\mathbf{P}(p_0)$. The choice of a uniform distribution over a finite range between a minimum and maximum pressure p_{min} and p_{max},

$$\mathbf{P}(p_0) = \begin{cases} \frac{1}{p_{\text{max}} - p_{\text{min}}} & \text{for } p_{\text{min}} \leq p_0 \leq p_{\text{max}}, \\ 0 & \text{otherwise,} \end{cases} \tag{2.14}$$

is simple, and also consistent with the bubble pressure measurements presented by Scholander and Nutt (1960). With this choice of pressure distribution, it is possible to evaluate the integrals in Eq. 2.13 analytically and obtain the following expression for Φ:

$$\Phi = \begin{cases} \frac{V_0 P_\infty}{(\kappa-1)(p_{\text{max}} - p_{\text{min}})} \left[p_0 \left(\frac{p_0}{2P_\infty} - \frac{\kappa}{\kappa+1} \left(\frac{p_0}{P_\infty}\right)^{\frac{1}{\kappa}} \right) \right]_{p_0 = p_{\text{min}}}^{p_0 = p_{\text{max}}} & \text{if } \kappa \neq 1, \\ \frac{V_0}{4(p_{\text{max}} - p_{\text{min}})} \left[{p_0}^2 \left(2\ln\left(\frac{p_0}{P_\infty}\right) - 1 \right) \right]_{p_0 = p_{\text{min}}}^{p_0 = p_{\text{max}}} & \text{if } \kappa = 1. \end{cases} \tag{2.15}$$

(See Appendix 2.10 for a detailed derivation.)

In practice, the average bubble pressure in a finite volume of ice is much easier to measure than individual bubble pressures or the distribution of pressures. Assuming that all bubbles in a volume of ice are at the average pressure P_0, i.e. that $\mathbf{P}(p_0) = \delta(P_0)$, results in a simple expression for Φ,

$$\Phi = \begin{cases} \frac{V_0 P_0}{\kappa-1} \left(1 - \left(\frac{P_\infty}{P_0}\right)^{\frac{\kappa-1}{\kappa}}\right) & \text{if } \kappa \neq 1, \\ V_0 P_0 \ln\left(\frac{P_0}{P_\infty}\right) & \text{if } \kappa = 1. \end{cases} \tag{2.16}$$

The error introduced by this assumption can be estimated by comparing Eq. 2.15 and Eq. 2.16, with $P_0 = (p_{\max} - p_{\min})/2$. Performing this exercise with the bubble pressure data presented in Scholander and Nutt (1960) results in a difference between the two expressions of at most 6% or 4% for $\kappa = 1$ or $\kappa = 7/5$, respectively.

Equation 2.16 gives an accurate value for the total potential energy Φ of the bubbles in a finite volume of ice, with reasonable assumptions based on the sparsely available data. However, its derivation depends upon the fact that the potential energy ϕ is a linear function of bubble volume v_0 and weakly nonlinear function of bubble pressure p_0. There is no guarantee that the fraction of a bubble's potential energy that is converted to sound when it is released from the ice will not depend upon v_0 or p_0 in a nonlinear fashion. Therefore, while Eq. 2.16 can be taken as a realistic upper bound on the energy that can be radiated as sound when a volume of ice melts, it cannot be assumed that the total energy radiated as sound E will always be proportional to the total potential energy Φ with a constant factor of proportionality. In the following sections, we attempt to quantify this effect.

2.3 An idealized model for sound radiated by released bubbles

In Section 2.2, expressions for the potential energy of compressed air bubbles were derived. However, not all of this energy will be converted into sound when a bubble is released into the water. Moreover, the fraction of energy that is converted into sound is likely to depend upon properties of the bubble, or the way in which the gas is released (Grossman et al., 2024). In this section, an attempt is made to quantify this effect through the creation of a simple model for the bubble release.

The model of bubble release used here is based upon the Rayleigh-Plesset equation. The Rayleigh-Plesset equation is an approximate nonlinear equation of motion that describes the oscillations of a spherical bubble in an incompressible and viscous fluid (see Section 4.2.1 of Leighton (1994) for a derivation). The model used here has two distinguishing features. First, we use an effective viscosity μ_{eff} which, in addition to viscous damping, incorporates losses due to radiation and thermal damping in an ad hoc way. The effective viscosity is defined as

$$\mu_{\text{eff}} = \frac{1}{2}\rho {R_{\text{eq}}}^2 (b_{\text{th}} + b_{\text{ac}} + b_{\text{vs}}), \tag{2.17}$$

where $\rho = 1025$ kg m^{-3} is the density of sea water, R_{eq} is the equilibrium radius of the bubble, and b_{th}, b_{ac}, and b_{vs} are the thermal, acoustic, and viscous damping coefficients, with units of s^{-1}. These coefficients are calculated as described in Prosperetti (1977). Second, we include a time-varying externally imposed pressure which is designed to simulate the removal of the bubble from the ice. This pressure is given by

$$p_{\text{ext}}(t) = \left(p_0 - \frac{2\sigma}{R_0} - P_\infty\right) e^{\frac{-t}{\tau}}, \tag{2.18}$$

where p_0 is the initial pressure in the bubble, $\sigma = 0.076$ N m^{-1} is the surface tension of water, R_0 is the initial radius of the bubble, P_∞ is the far-field pressure in the water, and t is time since the release of the bubble. The pressure p_{ext} is equal to the difference between the water pressure and bubble pressure at time $t = 0$, and then decays to zero with exponential time constant τ. We will refer to τ as the "timescale of release" of the bubble.

The Rayleigh-Plesset equation, written with our notation, is

$$R\ddot{R} + \frac{3\dot{R}^2}{2} = \frac{1}{\rho}\left(\left(P_\infty + \frac{2\sigma}{R}\right)\left(\frac{R_{\text{eq}}}{R}\right)^{3\kappa} - \frac{2\sigma}{R} - P_\infty - p_{\text{ext}} - \frac{4\mu_{\text{eff}}\dot{R}}{R}\right), \tag{2.19}$$

where p_{ext} is a prescribed function of time. $\dot{R}$ and $\ddot{R}$ are the first and second derivatives of R with respect to time, respectively. (All other variables and constants are defined above and in Tables 2.1, 2.3, and 2.2.) Equation 2.19 is a nonlinear second order ordinary differential equation for R, which must be integrated numerically, using initial conditions $R(0) = R_0$ and $\dot{R}(0) = 0$.

Once Equation 2.19 has been solved to obtain R, $\dot{R}$, and $\ddot{R}$, the radiated acoustic pressure, normalized to its value at a distance of $r = 1$ m from the bubble, as a result of the motion of the bubble wall can be computed using Eq. 2.20,

$$p_{\text{rad}}(t)\bigg|_{r=1\text{m}} = \rho R\left(\ddot{R}R + 2\dot{R}^2\right). \tag{2.20}$$

This expression is obtained from Equation 3.126 in Leighton (1994).

It should be noted that this model for bubble release has several serious limitations. First, it assumes spherical symmetry at all times during the process of bubble release, which cannot physically be true for a bubble escaping from ice. In reality, the bubbles will be initially non-spherical as a result of their asymmetric release into the water, resulting in shape mode oscillations that can contribute to the total sound produced by the bubble (Longuet-Higgins, 1989a,b). The presence of the ice wall immediately adjacent to the oscillating bubble in the water also affects the frequency of the sound produced (Strasberg, 1953). Second, the model also assumes that the bubble remains intact as a single bubble. However, we have observed examples in our own experimental data where a single bubble in the ice breaks up into multiple smaller bubbles in the water upon its release, and this processes cannot be described by our model. Third, the exponentially decaying external pressure is a gross simplification of the various physical processes which may allow for gas to escape from the ice more quickly or slowly. Fourth, the acoustic signatures of some bubbles released from ice are not well-described by the Rayleigh-Plesset equation, as discussed by Grossman et al. (2024). Despite these shortcomings, the model presented here provides a tool to address the question of how the efficiency of the conversion of bubble potential energy to acoustic energy may vary as a function of the bubble properties and the timescale of release, with the minimum amount of added complexity that is necessary to do so.

The behavior of the model is illustrated by Fig. 2.2 for three different values of the release timescale τ, normalized by the bubble natural period T. The natural period is calculated

Table 2.3. Variables II.

Symbol	Units	Description
r	m	Distance between bubble and hydrophone
m	kg	Mass of a piece of ice
V_m	$\mathrm{m^3\ kg^{-1}}$	Volume of bubbles per unit mass of ice
ε	J	Acoustic energy radiated by a single bubble
E	J	Total acoustic energy radiated by a finite volume of melting ice
E_m	$\mathrm{J\ kg^{-1}}$	Acoustic energy per unit mass radiated by melting ice
Φ_m	$\mathrm{J\ kg^{-1}}$	Potential energy of bubbles per unit mass of ice
ψ	J	modeled energy released by a single bubble assuming a rapid release form the ice
Ψ	J	modeled energy released by bubbles in a finite volume of ice
Ψ_m	$\mathrm{J\ kg^{-1}}$	modeled energy released by bubbles in the ice assuming rapid release per unit mass
μ_{eff}	$\mathrm{kg\ m^{-1}\ s^{-1}}$	Effective viscosity for an oscillating bubble
f_n	Hz	Natural frequency of an air bubble in water

as $T = 1/f_n$, where the undamped natural angular frequency of the bubble is given by Eq. 2.21,

$$f_n = \frac{1}{2\pi R_{\text{eq}}}\sqrt{\frac{1}{\rho}\left(3\kappa P_\infty + (3\kappa - 1)\frac{2\sigma}{R_{\text{eq}}}\right)}. \tag{2.21}$$

For $\tau/T \gg 1$, the bubble expands gradually over the course of many periods, resulting in small-amplitude oscillations. Conversely, for $\tau/T \ll 1$, the bubble overshoots its equilibrium radius during the first cycle and is driven into large-amplitude oscillations.

We define the modeled radiated acoustic energy, ψ_τ to be the total energy in the acoustic pressure wave radiated by the bubble as it expands to reach its equilibrium radius. This is calculated by integrating the power of the acoustic pressure wave over the surface of the unit sphere centered at the bubble, and integrating this power over time,

$$\psi_\tau(R_0, p_0, \tau) = \frac{4\pi}{\rho c}\int_0^\infty {p_{\text{rad}}}^2 dt. \tag{2.22}$$

To evaluate Eq. 2.22 in practice, the upper bound of the integral must be taken to be a finite time

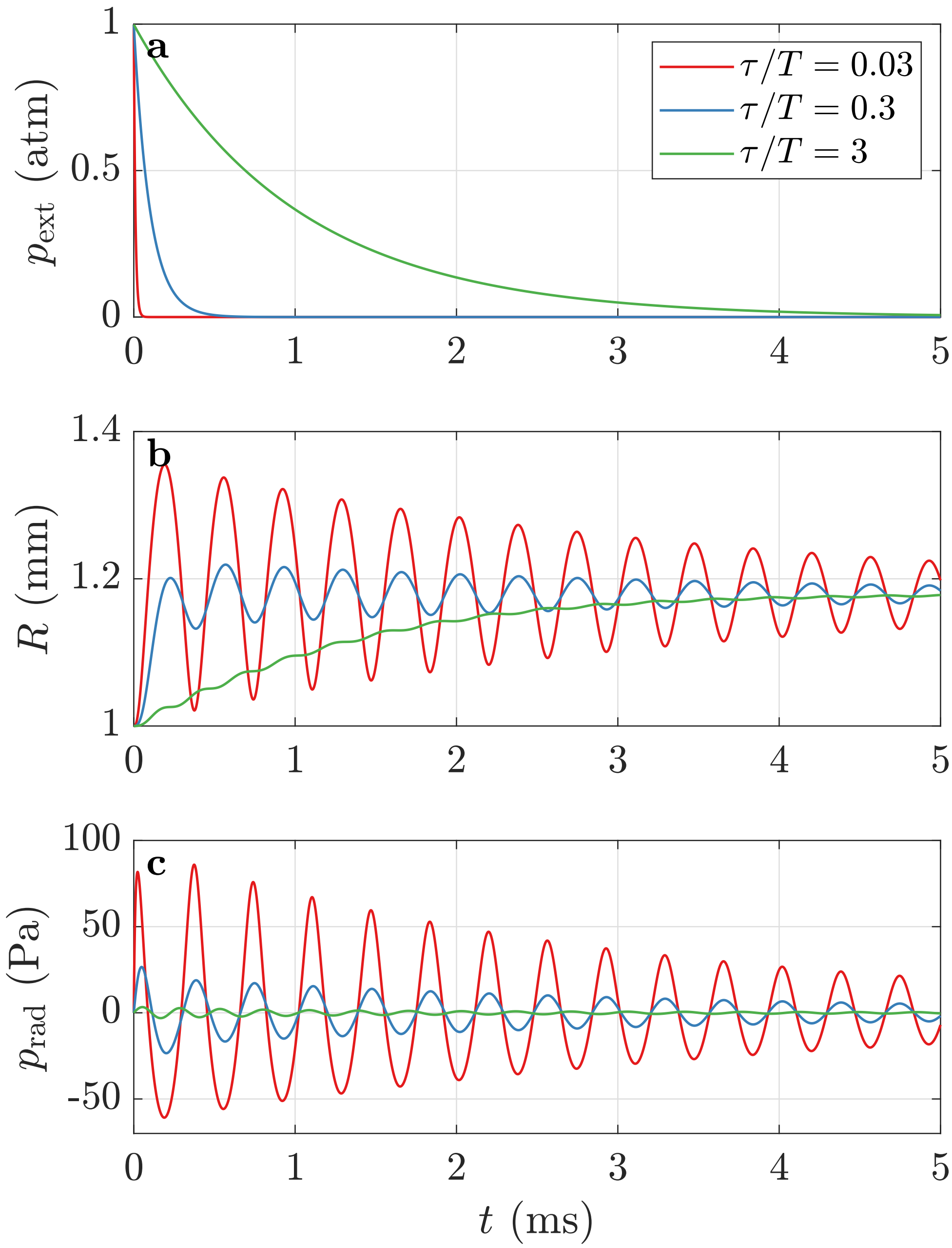

Figure 2.2. Timeseries plots demonstrating the behavior of the model for bubble release and sound generation outlined in Eq. 2.17-2.20. These plots are generated for a bubble with initial radius $R_0 = 1$ mm and pressure $p_0 = 2P_{\text{atm}}$, with $P_\infty = P_{\text{atm}}$. The output is shown for three different values of the ratio of the release timescale τ to the bubble natural period T. **a** The imposed external pressure $p_{\text{ext}}(t)$ simulating the release of the gas. **b** Bubble radius $R(t)$, which expands towards R_{eq} and oscillates. **c** The radiated acoustic pressure $p_{\text{rad}}(t)$ scaled to its value at a distance of $r = 1$ m from the bubble.

after which the energy content of p_{rad} is negligible. The radiated acoustic pressure timeseries p_{rad} is a function of R_0, p_0, and τ, making ψ_τ a function of these three quantities.

The efficiency of the conversion from potential energy to radiated acoustic energy in the model, ψ_τ/ϕ, is presented in Fig. 2.3 for two different bubble radii and pressures. For each combination of R_0 and p_0, the conversion efficiency increases for decreasing τ/T, where τ/T is the normalized release timescale, and asymptotically approaches a maximum value for $\tau/T \ll 1$. This observation motivates the definition of the maximum modeled acoustic energy,

$$\psi(R_0, p_0) = \lim_{\tau/T \to 0} \psi_\tau(R_0, p_0, \tau), \tag{2.23}$$

which is independent of the release timescale τ. Physically, this means that the conversion of potential energy to sound in the model is most efficient when the release of the gas occurs on timescales much shorter than the natural period of the bubble, and this behavior is consistent with the observations presented in Grossman et al. (2024).

The maximum modeled acoustic energy ψ must be computed numerically for each combination of p_0 and R_0, by running the bubble release model with $\tau \ll T$. Figure 2.4 shows the conversion efficiency ψ/ϕ over the range of initial bubble pressures and radii observed in our experimental data. The conversion efficiency varies by 2 orders of magnitude over these ranges. It is higher for larger bubbles and higher bubble pressures. The efficiency reaches as high as about 0.4 for a bubble with $R_0 = 1$ cm and $p_0 = 4$ atm.

The maximum modeled acoustic energy of individual bubbles can be summed over a finite volume of ice containing many bubbles in the same way that the potential energy can. The total maximum modeled acoustic energy of a finite volume of ice containing N bubbles can be computed as

$$\Psi = \sum_{i=1}^{N} \psi(R_{0,i}, p_{0,i}). \tag{2.24}$$

Alternatively, Ψ can be written as an integral over the probability distributions of bubble size

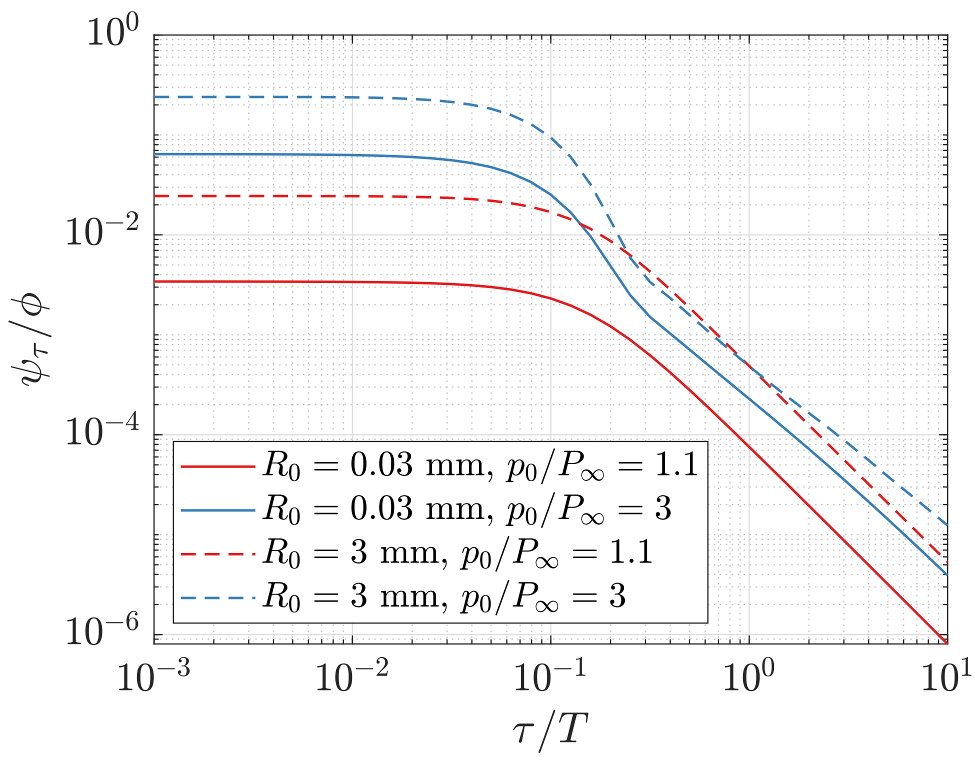

Figure 2.3. Efficiency of the conversion of potential energy ϕ into radiated acoustic energy ψ_τ as a function of release timescale τ for two different initial bubble radii and pressures. ψ_τ/ϕ increases as τ/T decreases, before asymptotically approaching a constant value for $\tau/T \ll 1$.

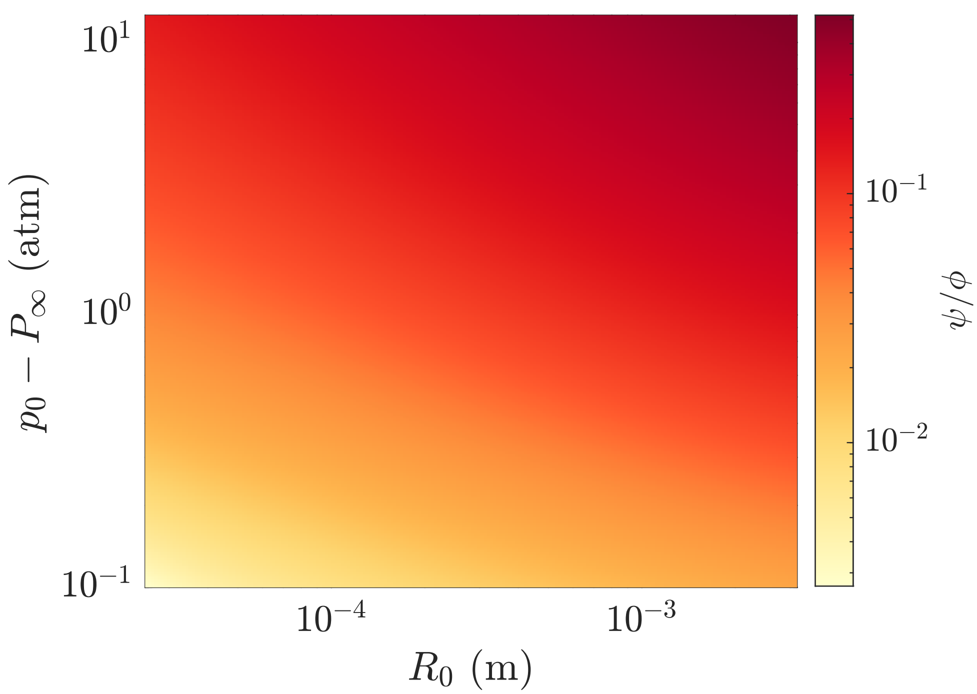

Figure 2.4. Plot of the modeled conversion efficiency ψ/ϕ of bubble potential energy ϕ into maximum modeled radiated acoustic energy ψ, as a function of initial bubble radius R_0 and pressure p_0. The conversion efficiency increases with increasing radius and pressure, and varies by multiple orders of magnitude over the range of radii and pressures tested here. ψ/ϕ reaches as high as about 0.5 for the largest radius ($R = 3.2$ mm) and pressure ($p_0 = 14$ atm) tested.

and pressure,

$$\Psi = \mathscr{V}\mathscr{N} \iint \psi(p_0, R_0)\mathbf{P}(p_0|R_0)\mathbf{P}(R_0)dp_0dR_0. \tag{2.25}$$

Here $\mathscr{V}$ is a finite volume of ice, $\mathscr{N}$ is the number of bubbles contained in this finite volume of ice, $\mathbf{P}(R_0)$ is the probability density of a bubble having radius R_0, and $\mathbf{P}(p_0|R_0)$ is the probability density of a bubble with radius R_0 having pressure p_0. Unlike with the total potential energy, there is no way to obtain a simple analytical expression for the maximum modeled acoustic energy.

2.4 Experiment

Sections 2.2 and 2.3 described methods to calculate the potential energy and modeled maximum acoustic energy of air bubbles trapped in glacier ice. This section describes an experiment performed using blocks of glacier ice in order to evaluate the predictive power of these quantities.

The data used here was collected in the summer of 2019 at the Polish Polar Station in Hornsund Fjord in the Norwegian territory of Svalbard. Floating pieces of ice were collected from bays in front of four different glaciers in the fjord: Hansbreen, Paierlbreen, Mulbacherbreen, and Samarinbreen. The majority of the pieces of ice used in the analysis presented here originated from Hansbreen, and there were no discernible patterns in the results relating to the glacier of origin. The pieces of ice were taken back to the station in a small boat, where they were cut, using electric chainsaws, into small blocks for processing. Each block was about 10-12 cm wide and tall, and the blocks were cut across their long axis to form slices of varying thickness to be used for different purposes. Measurement of bubble size distributions was done with thin slices of ice, while gas content and acoustic emissions where measured during controlled melting experiments performed with thicker slices of ice.

2.4.1 Bubble size

Measurement of the number density of bubbles and the distribution of their sizes was performed using thin (~5 mm) slices of ice. The pieces of ice were first weighed. They were then photographed on a backlit screen, with a scale present in the field of view to calibrate the images and measure absolute sizes. The numbers and sizes of bubbles within a slice were estimated from the photographs manually using the software ImageJ. This was done by first tracing the outlines of the the two-dimensional shapes of the bubbles in the images. The area of this shape a is then used to compute the cross-sectional area equivalent radius,

$$R_0 = \sqrt{\frac{a}{\pi}}, \tag{2.26}$$

which is taken as the estimate of bubble radius. The bubble volume is then given by

$$v_0 = \frac{4}{3}\pi R_0^3 \tag{2.27}$$

The total volume of all of the bubbles in the thin slice of the ice is then the sum of the individual bubble volumes, $V_0 = \sum v_0$. The total bubble volume per unit mass V_m, in units of m^3 kg^{-1}, can be calculated as $V_m = V_0/m$, where m is the mass of the piece of ice. It is also possible to estimate the density of the ice from V_m; this is discussed in Appendix 2.13.

2.4.2 Controlled melting experiments

Controlled melting experiments were performed with thick (~5 cm) slices of ice. These experiments enabled the collection of two types of data: the gas content of the ice, and the acoustic energy released during melting. The pieces of ice used in these experiments were weighed, then placed in a tub of water and allowed to melt. In some instances, the experiment was terminated before the piece of ice had melted completely; in these cases, any ice remaining at the end of the experiment was weighed. The difference between the initial and final masses of the piece of ice was used as the mass of ice melted, m.

The dimensions of the tub were 57 cm by 34 cm, and it was filled with water 40 cm deep. The water in the tub was taken from the fjord, and the temperature of the water, measured in the tub during each experiment, varied between about 5 and 10 °C. The salinity of the water was not measured, and may have varied and been somewhat fresher than ambient ocean values of $\sim$ 35 PSU on account of melting ice and freshwater outflow in the fjord. A small pump was used to generate recirculating flow in the tub and prevent stratification of the water. A picture of the experimental setup is presented in Fig. 2.5, and a schematic view describing the geometry of the tank is shown in Fig. 2.6.

Gas content

To measure the gas contained in the ice, the pieces of ice to be melted were placed under a funnel with its wide-end opening pointing downwards. The buoyancy of the ice held it in place within the cone of the funnel as it melted. The air bubbles released from the ice as it melted were collected by the funnel, and the spout of the funnel was connected to a volume gauge from which accumulating air displaced water held at atmospheric pressure. In this way, the total gas content of the melted ice, G, with units of m^3 at atmospheric pressure, was measured. Dividing this gas content by the mass of the ice that had melted m produces a gas content per unit mass of ice for each thick slice of ice, G_m, with units of m^3 kg^{-1} (at 1 atm).

Acoustic emissions

To measure the acoustic emissions of the bubbles released from the melting ice, an HTI 96-min hydrophone was placed in the tank. The hydrophone was at a distance of approximately $r = 23$ cm from the center of the nominal position of the ice in the funnel. In an effort to minimize the effects of multipath arrivals, the inside walls of the tank were lined with fabric, with a layer of plastic interior to the fabric lining containing the water. Acoustic data were collected in a quiet room inside one of the buildings of the research station. A high-pass filter

Figure 2.5. Picture of the controlled melting experiment setup. An aluminum box (right) was used as a tank for the experiment. The box was lined with towels and a large plastic bag to make it hold water and to reduce the effect of reflection of sound from the tank walls. The funnel that held the ice and collected the gas that was released was held in place by a scaffold of aluminum rods. This assembly can be seen sitting in the tank. A schematic of the tank showing the geometry of the funnel, ice, and hydrophone is shown in Fig. 2.6. An immersion pump was placed in a bucket next to the tank, and pumped water into the tank through one hose and out of the tank through a second hose in order to keep the water in the tank well-mixed.

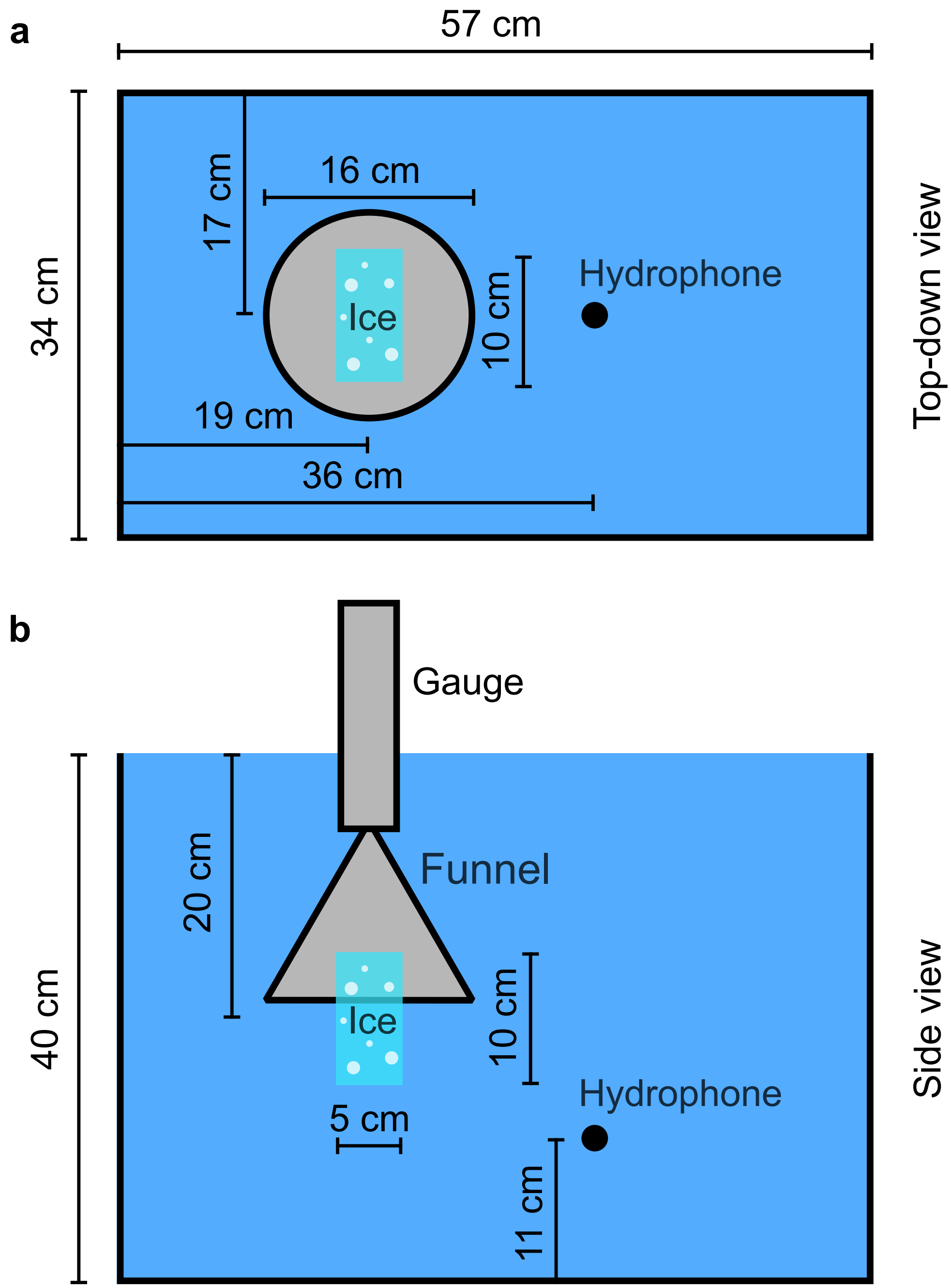

Figure 2.6. Schematic diagram of the setup for the controlled melting experiment. **a** Top-down view, **b** side view. The ice was positioned under the funnel and held in place by its own buoyancy. A hose ran from the funnel to a gauge used to measure the volume of air released from the bubble in the ice during melting. The funnel and hydrophone were held in place with a scaffold of metal rods, which is not shown here, but can be seen in Fig 2.5.

with a pass-band frequency of 1 kHz was applied to the hydrophone output to filter out noise from the recirculation pump.

The filtered acoustic data consists of a series of narrow-band decaying sinusoidal oscillations, the majority of which are expected to have been generated by the release of a bubble from the ice. An event detection algorithm was run on the acoustic recording for each piece of melted ice, truncating it into a collection of N shorter pressure time series p_i, each of which is assumed to be the result of a single bubble released from the ice.

The energy of an individual event, ε_i, is computed as

$$\varepsilon_i = \frac{4\pi r^2}{A(f_i)\rho c}\int_0^\infty {p_i}^2 dt, \tag{2.28}$$

and has units of J. In this expression, r is the nominal distance between the bubble and hydrophone, $\rho = 1025$ kg m^{-3} is the density of sea water, and $c = 1490$ m s^{-1} is the speed of sound. While the upper bound on this integral is written as ∞, in practice it must be taken to be a finite time after which the power in p_i has become negligible. The factor $A(f_i)$, where f_i is the peak frequency of the acoustic event, accounts for the expected difference in energy between the observation made in the tank and the estimated value of the energy in the absence of reflection from the tank walls. The uncertainty in the event energy is expected to be dominated by the asymmetric uncertainty in the correction factor A, and can be written as

$$\varepsilon_i + \Delta^+\varepsilon_i = \left(\frac{1}{A(f_i) - \Delta^- A(f_i)}\right)\frac{4\pi r^2}{\rho c}\int_0^\infty {p_i}^2 dt, \tag{2.29}$$

$$\varepsilon_i - \Delta^-\varepsilon_i = \left(\frac{1}{A(f_i) + \Delta^+ A(f_i)}\right)\frac{4\pi r^2}{\rho c}\int_0^\infty {p_i}^2 dt. \tag{2.30}$$

The superscripts $^+$ and $^-$ on Δ indicate the positive or negative uncertainty in ε and A, for which the uncertainty is asymmetric. The calculation of A, $\Delta^+ A$, and $\Delta^- A$ is discussed in detail in Appendix 2.11.

The total acoustic energy radiated by a piece of ice as it melted, E, is the sum of the individual event energies,

$$E = \sum_{i=1}^{N} \varepsilon_i. \tag{2.31}$$

The uncertainty in the total energy is computed with a worst-case assumption that errors in the individual energies are correlated,

$$E \pm \Delta_{\pm} E = \sum_{i=1}^{N} (\varepsilon_i \pm \Delta_{\pm} \varepsilon_i). \tag{2.32}$$

The mass-normalized acoustic energy is $E_m = E/m$, with units of J kg^{-1}, and with an error similarly normalized by the mass of the ice, $\Delta_{\pm} E_m = \Delta_{\pm} E/m$.

2.5 Results

In this section, we make use of the experiments discussed in Section 2.4 to test the theory and modeling constructs presented in Sections 2.2 and 2.3.

In the experiments conducted here, gas content G_m and acoustic energy E_m were measured for some slices of ice, while bubble volume V_m were measured for other slices. Calculating the potential energy Φ_m and Ψ_m requires both the gas content G_m and the bubble volume in the ice V_m. We therefore make use of instances where V_m was measured for thin slices of ice that were immediately adjacent to thick slices for which G_m and E_m were measured. There were 12 unique thick slices of ice for which G_m and E_m were measured and which were immediately adjacent to at least one thin slice of ice for which V_m was measured. We assume that the measurement of V_m from this thin slice of ice is representative of the adjacent thick slice of ice in order to make the desired comparisons. There was one thin slice of ice which was adjacent to two thick slices of ice that were melted (one on each side). We use this to estimate the error introduced by the assumption that the properties of the adjacent thin and thick slices of ice are the same. The difference between the two measurements of G_m for the two thick slices of ice was about 10%. Since G_m is a precisely measured quantity for the block of ice that melted, whereas V_m

is the quantity estimated from the adjacent piece of ice, we assign this 10% uncertainty due to variability in the ice to V_m, and let $\Delta V_m = 0.1V_m$.

2.5.1 Gas pressure

Estimates of the average gas pressure in bubbles in the ice, P_0, can be obtained by combining the measurements of the mass-normalized bubble volume V_m and gas content G_m. Since G_m is the volume occupied by the gas contained in 1 kg of ice when the gas is brought to atmospheric pressure, and V_m is the volume of the bubbles in 1 kg of ice, the average pressure of the gas in the ice can be computed from the ratio of the two quantities,

$$P_0 = P_{\text{atm}} \frac{G_m}{V_m}. \tag{2.33}$$

The relative error in the measurements of the gas content of the ice G_m is small compared to the error in estimates of the bubble volume V_m. The error in Eq. 2.33 is therefore dominated by the error in bubble volume V_m, so the relative error in the pressure P_0 is

$$\frac{\Delta P_0}{P_0} = \frac{\Delta V_m}{V_m}. \tag{2.34}$$

2.5.2 Potential and maximum modeled energy

From the estimates of bubble pressure P_0 and volume V_m, the mass-normalized potential energy can be computed for the 29 thick slices of ice using Eq. 2.35:

$$\Phi_m = \frac{V_m P_0}{\gamma - 1} \left(1 - \left(\frac{P_\infty}{P_0} \right)^{\frac{\gamma-1}{\gamma}} \right). \tag{2.35}$$

The units of Φ_m are J kg^{-1}. P_∞ is the far-field pressure in the water, and $\gamma = 7/5$ is the ratio of heat capacity at constant pressure to heat capacity at constant volume for air. The uncertainty in the mass-normalized potential energy (assuming $P_\infty = P_{\text{atm}}$) is

$$\Delta\Phi_m = \frac{P_\infty}{\gamma}\left(\frac{P_0}{P_\infty}\right)^{\frac{1}{\gamma}}\Delta V_m \tag{2.36}$$

(see Appendix 2.12 for a detailed explanation).

The maximum modeled acoustic energy Ψ_m, with units of J kg^{-1}, can also be estimated for the 12 thick slices of ice with the assumption that all bubbles in the ice are at the average pressure P_0. Ψ_m can then be computed by summing the individual maximum modeled energies $\psi(R_{0,i}, P_0)$ of the bubbles in the thin slice of ice, and dividing by the mass of the thin slice of ice m,

$$\Psi_m = \frac{1}{m}\sum_{i=1}^{N}\psi(R_{0,i}, P_0). \tag{2.37}$$

The two thick blocks of ice that share an adjacent thin slice of ice, the calculated value of Ψ_m differs by about 50%, as a result of the difference in estimated bubble pressure P_0. We therefore assign an estimated uncertainty of $\Delta\Psi_m = 0.5\Psi_m$ to all values of Ψ_m.

It should be noted that this estimate of $\Delta\Psi$ does not account for the error introduced by the assumption that $p_0 = P_0$ for all bubbles. An estimate of the additional error resulting from this assumption would require an assumption about the joint distribution of bubble pressures and radii $\mathbf{P}(p_0|R_0)$. The value of Ψ calculated assuming $p_0 = P_0$ could then be compared to that calculated with the assumed distribution. However, given that the true joint distribution $\mathbf{P}(p_0|R_0)$ remains unknown, and the scatter in the data presented (see Fig. 2.8) is large, we believe this exercise to be of limited utility.

A comparison of Ψ_m and Φ_m for the 12 pieces of ice studied in the experiment is presented in Fig. 2.7. The two quantities are highly correlated. Since Ψ_m is a more strict upper bound on the acoustic energy than Φ_m, it should be expected that $\Psi_m < \Phi_m$ for all blocks of ice, and indeed this is the case. The ratio of Ψ_m/Φ_m is about 0.03 for the lowest values of Φ_m, and rises to about 0.3 for the highest values of Φ_m. For a given value of potential energy Φ_m, pieces of ice

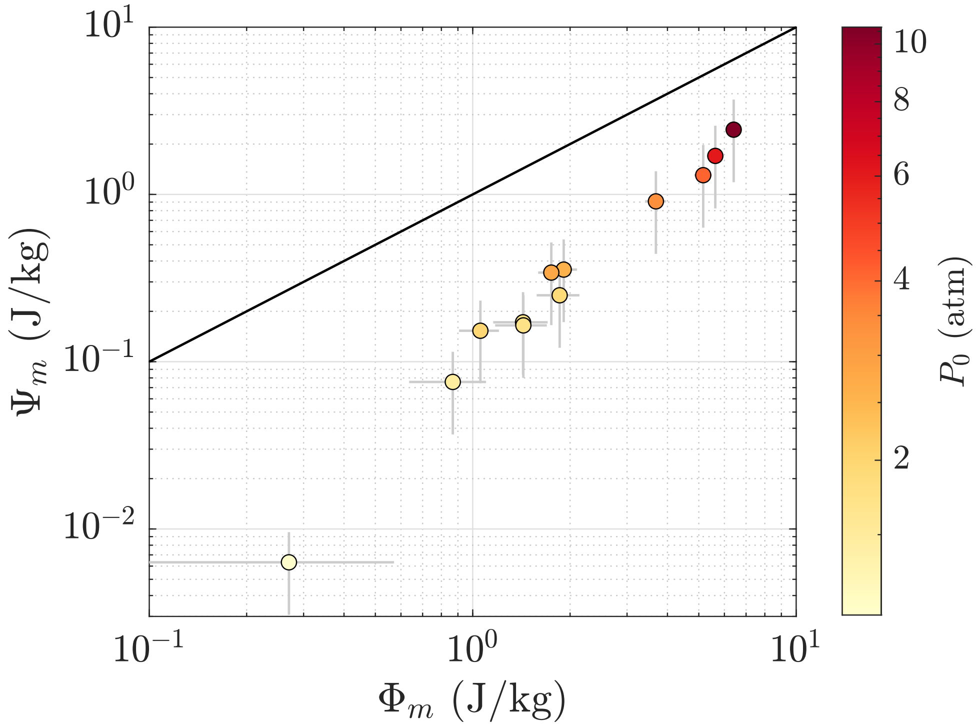

Figure 2.7. Estimates of the total mass-normalized modeled acoustic energy Ψ_m vs. total mass-normalized potential energy Φ_m for pieces of ice in the controlled melting experiments. Each point represents one piece of ice that was melted. The points are colored by the average bubble pressure P_0. The solid black line represents a one-to-one ratio of maximum modeled energy Ψ_m to potential energy Φ_m. All of the points fall below this line, indicating that Ψ_m is a more strict upper bound for the radiated acoustic energy than Φ_m.

with a higher average bubble pressure P_0 (indicated by color in Fig. 2.7) tend to have slightly higher maximum modeled energy Ψ_m. These behaviors are expected, since the ratio ψ/ϕ for an individual bubble is greater for bubbles with higher pressure and larger radii, as shown in Fig. 2.4.

2.5.3 Predicting the acoustic energy of the ice

A comparison of the acoustic energy E_m (the calculation of which is described in Section 2.4.2) and maximum modeled energy Ψ_m for the 12 pieces of ice studied in the experiment is presented in Fig. 2.8. The points all fall below the solid black 1:1 line, indicating that $E_m < \Psi_m$ for all blocks of ice in the experiment, and Ψ_m (and therefore Φ_m) are indeed upper bounds for the acoustic energy E_m. However, while the greatest value of E_m for a given value of Ψ_m is typically greater for greater values of Ψ_m, there is not a strong correlation between E_m and Ψ_m. In fact, E_m varies by multiple orders of magnitude for pieces of ice with similar values of Ψ_m. While Ψ_m sets an upper bound for the amount of acoustic energy E_m that can be radiated by ice when it melts, the lower bound on E_m is independent of Ψ_m.

The modeling work presented in Section 2.3 provides a possible explanation for the low correlation between E_m and Ψ_m. Ψ_m is the maximum acoustic energy expected based on modeling that assumes rapid release ($\tau \ll T$) of all bubbles from the ice. Figure 2.3 suggests that bubbles released on slower timescales ($\tau > T$) will release less energy. A larger fraction of bubbles released slowly would be expected to make E_m a smaller fraction of Ψ_m. Based on Fig. 2.3, longer timescales of release can result in a reduction of the radiated energy by several orders of magnitude relative to the modeled energy with rapid release ψ. This can explain the orders of magnitude of variability seen in E_m among blocks of ice with similar values of Ψ_m in Fig. 2.8.

It is possible to make a quantitative estimate of the fraction of bubbles in our data that were released rapidly. An analysis of individual bubble release events for a subset of the same dataset used here was presented in Grossman et al. (2024), and found a division between rapid and slow bubble release events, with the former generally having energies greater than 10 μJ (Fig. 5 in Grossman et al. (2024)). We therefore use this individual bubble energy threshold as a proxy for delineating between bubbles released rapidly and slowly. The points in Fig. 2.8 are colored by the fraction of acoustic events with an individual event energy above this threshold. For a given value of Ψ_m, the points are generally sorted vertically, with blocks containing a higher fraction of events above the threshold corresponding to greater values of E_m. This supports the hypothesis that the fraction of bubbles released rapidly is varying between blocks of ice, and this variation is what is driving the variability in the radiated acoustic energy E_m. A direct comparison of E_m to this fraction of events with $\varepsilon > 10$ μJ is presented in Fig. 2.9, which demonstrates that the two quantities are correlated (with coefficient of determination of 0.87, evaluated in log-log space).

We have also investigated the possibility that the density of the ice and the corresponding estimated depth of origin are responsible for controlling the fraction of modeled energy Ψ_m that

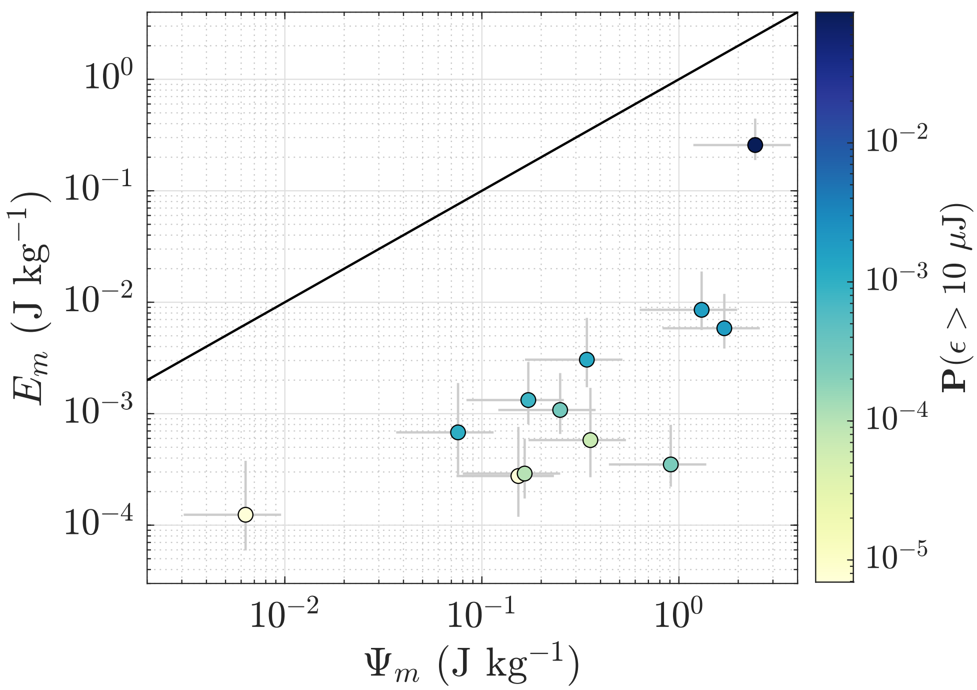

Figure 2.8. Estimates of the total mass-normalized acoustic energy E_m vs. the total mass-normalized modeled energy Ψ_m for pieces of ice in the controlled melting experiments. Each point represents one piece of ice that was melted. The points are colored by the fraction of individual events with acoustic energies greater than 10 μJ, which is a proxy for the fraction of rapid release events. The solid black line represents 100% conversion of maximum modeled energy Ψ_m into acoustic energy E_m. All of the points fall below this line, indicating that Ψ_m is an upper bound for E_m.

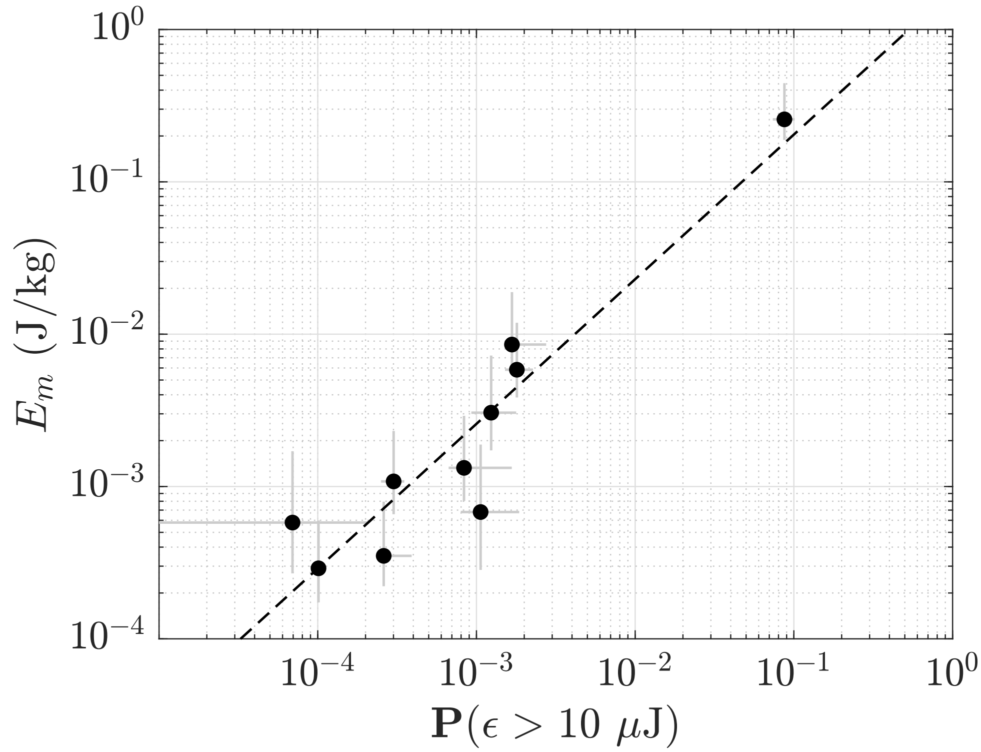

Figure 2.9. Estimates of the total mass-normalized acoustic energy E_m vs. the fraction of individual bubble release events that emitted more than 10 μJ of acoustic energy. Several points which have zero events above 10 μJ are excluded. The upper and lower error bars on $\mathbf{P}(\varepsilon > 10$ μJ) is estimated by taking the fraction of events for which the upper and lower uncertainty bounds on ε are greater than 10 μJ, respectively. The dotted black line shows a linear least squares line of best fit (in log-log space, neglecting error bars) which has a coefficient of determination of 0.87.

is actually converted into sound energy by the bubbles. This analysis is presented in detail in Appendix 2.13. While the depth of origin of the ice is correlated with the modeled energy Ψ_m of the ice, and therefore with the acoustic energy E_m, it does not offer any additional explanatory power with regards to the variability in E_m among pieces of ice with similar values of Ψ_m.

2.6 Discussion

The results presented in Section 2.5 demonstrate that the acoustic energy per unit mass E_m radiated by melting glacier ice can vary by multiple orders of magnitude. The analysis presented here suggests that the total bubble potential energy Φ_m and maximum modeled energy Ψ_m do provide upper bounds for the acoustic energy E_m radiated by melting glacier ice. This is a useful step towards making quantitative predictions of the acoustic energy radiated by melting glacier ice. It has also been shown that the timescale of release of the bubbles from the ice may control the efficiency with which the energy stored in the bubbles is converted into sound. This relationship provides both reasons for caution and possible future directions for research.

The quantitative upper bounds on the sound energy radiated by melting glacier ice developed here offer some predictive power. In particular, the mathematical expression for the potential energy presented in Eq. 2.16 and Eq. 2.35 provides some insight with regards to the dependence of melt noise on depth. Based on observations collected from ice cores, increasing overburden pressure with increasing depth causes the compression of the bubbles in ice. This results in a comparable number of bubbles, but with the ice at greater depths containing bubbles with smaller radii and higher internal pressures (Gow, 1968, 1971). If this compression occurs isothermally, as suggested by Bader (1950), the quantity P_0V_m may be expected to be roughly constant within a given glacier. The variability in the potential energy Φ_m will then be driven by

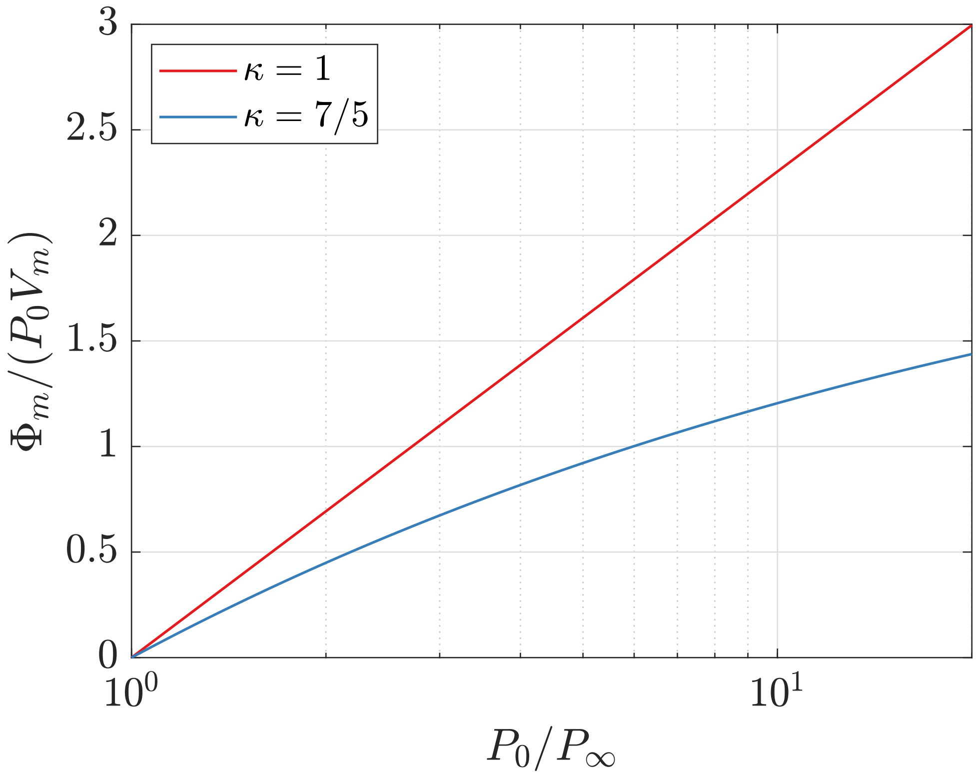

Figure 2.10. Potential energy per unit mass normalized by the product of bubble pressure and volume, $\Phi_m/(P_0 V_m)$, as a function of the ratio of bubble pressure to far-field pressure, P_0/P_∞. If $P_0 V_m$ is roughly constant, these curves describe the dependence of Φ_m on the ratio P_0/P_∞. $\Phi_m = 0$ when $P_0/P_\infty = 1$, and increases sub-linearly as P_0/P_∞ increases.

the ratio of bubble pressure to ambient pressure P_0/P_∞,

$$\Phi_m \propto \begin{cases} \frac{1}{\kappa-1}\left(1-\left(\frac{P_\infty}{P_0}\right)^{\frac{\kappa-1}{\kappa}}\right) & \text{if } \kappa \neq 1, \\ \ln\left(\frac{P_0}{P_\infty}\right) & \text{if } \kappa = 1. \end{cases} \tag{2.38}$$

Here, κ is the polytropic index for the expansion (typically $\kappa = \gamma = 7/5$). The potential energy normalized by $P_0 V_m$ increases as a function of P_0/P_∞, and is plotted in Fig. 2.10.

In the observations presented in Vishnu et al. (2023), blocks of glacier ice were lowered to a depth up 20 m and their acoustic emissions were observed to decline sharply with increasing depth. The ambient water pressure P_∞ increases linearly with depth beneath the water surface z as $P_\infty = P_{atm} + \rho g z$. Lowering ice into the water in this way therefore increases P_∞ while keeping

P_0 constant, thus decreasing the ratio P_0/P_∞. These observations are therefore qualitatively consistent with the formulation of bubble potential energy presented here.

The depth dependence of bubble pressure at a vertical glacier terminus may be more complicated. To the authors' knowledge, no observations of internal bubble pressures as a function of depth at the terminus of a tidewater glacier exist in the published literature. Observations of bubble pressures made from ice cores drilled in low-flow regions of ice sheets where ice is accumulating show that the bubble pressure there is atmospheric at the pore close-off depth, and then increases with increasing depth (Gow, 1968; Gow and Williamson, 1975). The initial rate of increasing pressure with increasing depth is faster than $\rho_{\text{ice}}g$, until the bubble pressure catches up to the overburden pressure at a depth of about 150-200 m. Below this depth the bubble pressure is expected to be roughly equal to the overburden pressure. In the ablation zone of a glacier, were surface melting exceeds surface accumulation of snow and there is no firn layer, the sorting of bubble pressure with depth will depend upon the timescale of equilibration of the bubbles in the ice, and may also be influenced by the flow of the glacier. If the bubbles have had time to equilibrate to the local overburden pressure, or if the region of pressure increase at a rate faster than the overburden pressure beneath the firn layer has completely melted, then we may expect the bubble pressure to increase more slowly than the hydrostatic pressure in the water with increasing depth. This would result in decreasing bubble potential and modeled energy with increasing depth, and, based on the results presented here, decreasing acoustic emissions with increasing depth. The observations presented by Vishnu et al. (2020) show that the melt noise generated at the terminus of Hansbreen (a glacier in Hornsund Fjord) decreases rapidly with increasing depth. This suggests that the bubble pressures P_0 are indeed increasing more slowly with increasing depth than the hydrostatic pressure P_∞, at least at this specific glacier.

The results of this study also suggest a need for caution in the pursuit of quantitative science with melt noise. While we have been able to establish upper bounds for the sound energy radiated by melting ice, we have also shown that the acoustic emissions of pieces of ice which had similar potential energy and maximum modeled energy contents can vary by orders of magnitude. Variation in the timescale of release of the bubbles from the ice is thought to be the driving force in this variability that is not explained by variation in energy stored in the bubbles. However, we are not aware of any method that can be used to predict what fraction of bubbles will be released from the ice rapidly. Moreover, this variability resulted in several orders of magnitude of variability in the acoustic energy radiated per unit of ice melted in our laboratory experiments conducted with pieces of ice that originated from a single fjord, and primarily from a single glacier. The acoustic energy radiated per unit mass of ice melted in a natural setting might vary similarly, which has the potential to be problematic for efforts to study even relative changes in melt noise.

We would like to close with a remark about anecdotal observations made in the field and during the experiments, which we believe may be relevant to the problem of variability in the acoustic energy radiated by melting ice. The acoustic emissions of the ice melted in the experiments were found to be time-sensitive. While it was not always possible to determine the exact time elapsed between calving of the ice from the terminus and its collection and processing, we found that ice that had calved from the terminus more recently tended to produce more sound when it was melted. Evidently this occurred as a result of changes in the conditions experienced by the ice after it calved off the terminus. While pressure melting around the bubbles, as described by Bader (1950), or the escape of gas through small cracks, as described by Scholander and Nutt (1960), could help explain this phenomenon, both of these processes should also result in a reduction in the potential energy Φ_m and maximum modeled energy Ψ_m. We believe it is also possible that the exposure of the ice to warmer water and air, sunlight, and reduced pressure alters the microcrystalline structure of the ice in such a way as to change the fraction of bubbles that are released rapidly, and thus the efficiency of conversion of this energy into sound.

In particular, the piece of ice with the highest value of E_m in Fig. 2.8 was collected from the melange produced by a calving event that was observed by the collection team, and was processed for the experiment within about an hour of its calving from the terminus. While this piece of ice had a maximum modeled energy and potential energy comparable to that of several other pieces of ice included in the experiment, it has the highest estimated fraction of rapidly released bubbles of any of the pieces of ice studied here. This offers some anecdotal support for the hypothesis that changes in the ice microcrystalline structure after it is removed from the terminus may be resulting in a decrease in the fraction of bubbles released rapidly, and therefore in the acoustic energy emitted as the ice melts.

If the hypothesis that change in the microcrystalline structure of the ice is contributing to change in the fraction of bubbles released rapidly is correct, it would have implications for efforts to quantify melt noise. It is possible that the variability in the fraction of bubbles released rapidly that is seen in our data is largely a result of variability in the time elapsed between when the ice calved from the terminus and when the experiment was conducted. In that case, the variability in the fraction of bubbles released rapidly might be lower for ice at the terminus than what we observe in our experimental data. The variability in the acoustic energy released per unit mass of ice at the terminus would also be less that what is observed in our experimental data. On the other hand, processes that alter the microcrystalline structure of the ice and cause the fraction of bubbles released rapidly to vary may also occur at the terminus, for instance after a submarine calving event or when the water temperature changes. In this case, this variability may make it difficult to disentangle changes in the sound level due to changes in submarine melt rate from changes in the sound level due to changes in the fraction of bubbles released rapidly.

Recent observational results offer some evidence that the variability in acoustic emissions at the termini of glaciers may be more regular than what is seen in our data. The results of Vishnu et al. (2025) show that the melt noise averaged over the entire terminus at several of the glaciers in Hornsund Fjord is correlated with ablation rates. This suggests that either the variability in acoustic emissions observed in our data is exaggerated relative to what is occurring at the terminus, or that there is sufficient averaging across the terminus to negate this variability, at least at these glaciers on the days when the measurements were collected. More observations of melt noise at glacier termini in conjunction with measurements of submarine melting, as well as detailed studies of the processes controlling the variability in the fraction of bubbles released rapidly, are needed in order to answer these questions more fully.

2.7 Conclusion

The goal of this paper has been to advance efforts to quantify the underwater acoustic emissions of melting glaciers. An estimate for the acoustically available potential energy stored in bubbles in glacier ice was presented. A model-based estimate of the maximum fraction of energy that may be expected to actually be radiated as sound was then developed. The results of experiments conducted with pieces of glacier ice were presented, and shown to be consistent with the theory and model-based upper bounds for the acoustic energy radiated by melting glacier ice. The results of the experiment also show substantial variability among different pieces of ice in the fraction of the available energy that is converted into sound. At least some of this variability seems to be connected to changes in the fraction of bubbles that are released from the ice rapidly. We speculate that the variability in the fraction of bubbles released rapidly in our data may not be representative of what is true at glacier termini, but more work is required to investigate this possibility.

2.8 Acknowledgements

This work was supported by Office of Naval Research Ocean Acoustics Division, Grant Nos. N00014-24-1–2394 and N00014-21-1-2316, the National Science Centre, Poland (grant 2021/43/D/ST10/00616), the Institute of Geophysics, Polish Academy of Sciences Grant 2a/IGF PAN/2017, and a subsidy for the Institute of Geophysics, Polish Academy of Sciences provided by the Ministry of Science and Higher Education of Poland. All data collection was staged at the Polish Polar Station, which is owned and operated by the Institute of Geophysics at the Polish Academy of Sciences. The color maps used in this publication were developed by Cynthia Brewer (http://colorbrewer.org) and ported to MATLAB by Scott Lowe (Lowe, 2016).

This chapter is in preparation for submission to ASA's *Journal of the Acoustical Society of America* with H. A. Johnson, G. B. Deane, M. D. Stokes, O. Glowacki, M. Moskalik, M. Chitre, H. Vishnu, and C. Powell as co-authors. The dissertation author was the primary investigator and author of this paper.

2.9 Appendix A: Derivation of potential energy expression

Substituting Eq. 2.2 and Eq. 2.3 into the integral in Eq. 2.7 results in the expression

$$\phi = \int_{R_0}^{R_{\mathrm{eq}}} \left(p_0 \left(\frac{R_0}{R_{\mathrm{eq}}} \right)^{3\kappa} - \frac{2\sigma}{R} \right) 4\pi R^2 dR. \tag{2.39}$$

Here, R is the radius of the bubble, R_0 is the initial radius of the bubble, R_{eq} is the equilibrium radius of the bubble, p_0 is the initial pressure of the bubble, κ is the polytropic index for the expansion of the gas, and $\sigma = 0.076$ N m^{-1} is the surface tension of sea water. This can be separated into two terms,

$$\phi = 4\pi p_0 {R_0}^{3\kappa} \int_{R_0}^{R_{\mathrm{eq}}} R^{2-3\kappa} dR - 8\pi\sigma \int_{R_0}^{R_{\mathrm{eq}}} R dR. \tag{2.40}$$

The first term in Eq. 2.40 needs to be treated separately for $\kappa \neq 1$ and $\kappa = 1$. If $\kappa \neq 1$, the first term can be evaluated to give

$$\begin{aligned} 1^{\mathrm{st}} \text{ term} &= \frac{4\pi p_0 {R_0}^{3\kappa}}{3-3\kappa} \left({R_{\mathrm{eq}}}^{3-3\kappa} - {R_0}^{3-3\kappa} \right), && (2.41) \\ &= \frac{4\pi p_0}{3(\kappa-1)} \left({R_0}^3 - {R_0}^{3\kappa} {R_{\mathrm{eq}}}^{3-3\kappa} \right), && (2.42) \\ &= \frac{4\pi p_0 {R_0}^3}{3(\kappa-1)} \left(1 - \left(\frac{R_0}{R_{\mathrm{eq}}} \right)^{3(\kappa-1)} \right). && (2.43) \end{aligned}$$

If $\kappa = 1$, the first term becomes

$$1^{\mathrm{st}} \text{ term} = 4\pi p_0 {R_0}^3 \int_{R_0}^{R_{\mathrm{eq}}} R^{-1} dR. \tag{2.44}$$

This integral can be evaluated using the natural logarithm, to give

$$1^{\text{st}} \text{ term} = 4\pi p_0 {R_0}^3 \left(\ln(R_{\text{eq}}) - \ln(R_0)\right), \tag{2.45}$$

$$= 4\pi p_0 {R_0}^3 \ln\left(\frac{R_{\text{eq}}}{R_0}\right), \tag{2.46}$$

$$= \frac{4}{3}\pi p_0 {R_0}^3 \ln\left(\frac{R_{\text{eq}}}{R_0}\right)^3. \tag{2.47}$$

The second term in Eq. 2.40 is independent of κ, and can be evaluated to give

$$2^{\text{nd}} \text{ term} = -4\pi\sigma\left({R_{\text{eq}}}^2 - {R_0}^2\right). \tag{2.48}$$

Note that, while the case of $\kappa = 1$ requires special consideration,

$$\lim_{\kappa\to 1} \frac{1}{\kappa - 1}\left(1 - \left(\frac{1}{x}\right)^{\kappa-1}\right) = \ln x, \tag{2.49}$$

so ϕ varies continuously as a function of κ.

2.10 Appendix B: Potential energy of finite volume of ice

We first consider the case of $\kappa \neq 1$. Beginning with Eq. 2.13, we have

$$\Phi = \frac{V_0}{\kappa - 1}\int p_0\left(1 - \left(\frac{p_0}{P_\infty}\right)^{\frac{1-\kappa}{\kappa}}\right)\mathbf{P}(p_0)dp_0. \tag{2.50}$$

Here, V_0 is the total volume of bubbles contained in a finite volume of ice, κ is the polytropic index for the expansion of the gas, p_0 is the initial pressure in the bubble, P_∞ is the far-field pressure in the water, and $\mathbf{P}(p_0)$ is the probability density of a bubble having pressure p_0. Substituting Eq. 2.14 for $\mathbf{P}(p_0)$ yields

$$\Phi = \frac{V_0}{(\kappa - 1)(p_{\max} - p_{\min})}\int_{p_{\min}}^{p_{\max}} p_0\left(1 - \left(\frac{p_0}{P_\infty}\right)^{\frac{1-\kappa}{\kappa}}\right)dp_0, \tag{2.51}$$

where $p_{\min}$ is the minimum bubble pressure and $p_{\max}$ is the maximum bubble pressure within the ice. Making the substitution $\zeta = p_0/P_\infty$, this expression becomes

$$\Phi = \frac{V_0 P_\infty}{(\kappa-1)(\zeta_{\max}-\zeta_{\min})} \int_{\zeta_{\min}}^{\zeta_{\max}} \zeta \left(1-\zeta^{\frac{1-\kappa}{\kappa}}\right) d\zeta. \tag{2.52}$$

The integral can then be evaluated,

$$\int_{\zeta_{\min}}^{\zeta_{\max}} \zeta \left(1-\zeta^{\frac{1-\kappa}{\kappa}}\right) d\zeta = \int_{\zeta_{\min}}^{\zeta_{\max}} \left(\zeta-\zeta^{\frac{1}{\kappa}}\right) d\zeta, \tag{2.53}$$

$$= \left[\frac{\zeta^2}{2} - \left(\frac{1}{\kappa}+1\right)^{-1} \zeta^{\frac{1}{\kappa}+1}\right]_{\zeta_{\min}}^{\zeta_{\max}}, \tag{2.54}$$

$$= \left[\zeta\left(\frac{\zeta}{2} - \frac{\kappa}{\kappa+1}\zeta^{\frac{1}{\kappa}}\right)\right]_{\zeta_{\min}}^{\zeta_{\max}}. \tag{2.55}$$

Inserting this expression back into Eq. 2.52 and replacing $\zeta = p_0/P_\infty$ gives

$$\Phi = \frac{V_0 P_\infty}{(\kappa-1)(p_{\max}-p_{\min})} \left[p_0\left(\frac{p_0}{2P_\infty} - \frac{\kappa}{\kappa+1}\left(\frac{p_0}{P_\infty}\right)^{\frac{1}{\kappa}}\right)\right]_{p_0=p_{\min}}^{p_0=p_{\max}} \tag{2.56}$$

For $\kappa = 1$, we proceed similarly. Equation 2.13 is

$$\Phi = V_0 \int p_0 \ln\left(\frac{p_0}{P_\infty}\right) \mathbf{P}(p_0) dp_0, \tag{2.57}$$

which, with the use of Eq. 2.14 for $\mathbf{P}(p_0)$, becomes

$$\Phi = \frac{V_0}{p_{\max}-p_{\min}} \int_{p_{\min}}^{p_{\max}} p_0 \ln\left(\frac{p_0}{P_\infty}\right) dp_0. \tag{2.58}$$

Making the same substitution $\zeta = p_0/P\infty$, we get

$$\Phi = \frac{V_0 P_\infty}{\zeta_{\max}-\zeta_{\min}} \int_{\zeta_{\min}}^{\zeta_{\max}} \zeta \ln(\zeta) d\zeta. \tag{2.59}$$

This integral can then be evaluated,

$$\int_{\zeta_{\min}}^{\zeta_{\max}} \zeta \ln(\zeta) d\zeta = \left[\frac{1}{2}\zeta^2 \ln(\zeta) - \frac{1}{4}\zeta^2 \right]_{\zeta_{\min}}^{\zeta_{\max}}. \tag{2.60}$$

Inserting this expression back into Eq. 2.59 and replacing $\zeta = p_0/P_\infty$ gives

$$\Phi = \frac{V_0}{4(p_{\max} - p_{\min})} \left[{p_0}^2 \left(2\ln\left(\frac{p_0}{P_\infty}\right) - 1 \right) \right]_{p_0=p_{\min}}^{p_0=p_{\max}}. \tag{2.61}$$

2.11 Appendix C: Reverberation in the tank

The measurements of acoustic emissions described in Section 2.4.2 were conducted in a tank. The acoustic signal measured at the receiver is a combination of the direct path arrival and paths which involve reflection from the surface and tank walls. The dimensions of the tank (57 cm by 34 cm and 40 cm deep) are such that the energy in the reflected arrivals may be substantial, and cannot be ignored. This effect is quantified through the introduction of a scaling factor A in Eq. 2.28. This scaling factor describes the ratio of the energy in the signal at the receiver in the tank to the energy in the signal that would be received in the absence of any reflection from tank boundaries. In other words, A is the ratio of the energy in the coherent sum of all arrival paths to the energy in the direct path arrival.

In order to calculate the correction factor A, we use an image method model based on the mathematical framework presented by Allen and Berkley (1979) for the reflection of sound in a rectangular enclosure. A detailed description of the model is presented in the appendix of Grossman et al. (2024). Experiments conducted with a tank of similar dimensions to the one used here and with similar lining of the walls are also described in the appendix of Grossman et al. (2024). The authors of that study determined that $\beta = -0.7$ was an appropriate reflection coefficient for the lined tank walls, and we use that same value here.

The value of $A(f_n)$ is computed separately for each bubble natural frequency f_n. A bubble with natural frequency satisfying Eq. 2.21 is simulated in a free-field environment and driven into oscillation with an initial pressure perturbation. The pressure time series at the receiver distance r is calculated, $p_{\text{free}}(t)$, and the total acoustic energy radiated is then computed as

$$\varepsilon_{\text{free}} = \frac{4\pi r^2}{\rho c} \int_0^\infty {p_{\text{free}}}^2 dt. \tag{2.62}$$

Here, r is the nominal distance between the bubble and the hydrophone, $\rho = 1025$ kg m^{-3} is the density of sea water, $c = 1490$ m s^{-1} is the speed of sound, and t is time since the start of the bubble release. The same procedure is then repeated, including the influence of reflections from the tank walls and surface, to compute the pressure time series at the receiver $p_{\text{tank}}(t)$ and the acoustic energy that would be measured at the receiver,

$$\varepsilon_{\text{tank}} = \frac{4\pi r^2}{\rho c} \int_0^\infty {p_{\text{tank}}}^2 dt. \tag{2.63}$$

The correction factor $A(f_n)$ that can be used to relate the acoustic energy measured in the tank to the actual acoustic energy radiated is then

$$A(f_n) = \frac{\varepsilon_{\text{tank}}}{\varepsilon_{\text{free}}}. \tag{2.64}$$

This factor allows for the radiated acoustic energy to be estimated from data collected in the tank as in Eq. 2.28. The value of $A(f_n)$ is presented for a range of values of the bubble natural frequency f_n in Fig. 2.11.

In our estimation, the dominant source of uncertainty in the correction factor is the uncertainty in the position of the bubble. Since the pieces of ice used in the controlled melting experiments were approximately 10 cm across, the position of the bubble radiating sound may vary by as much as 5 cm in any direction from the center of the piece of ice, which is taken as the nominal source location. To quantify this effect, the model for sound production in the tank was run a total of 9 times for each value of f_n: once with the bubble positioned at the nominal source

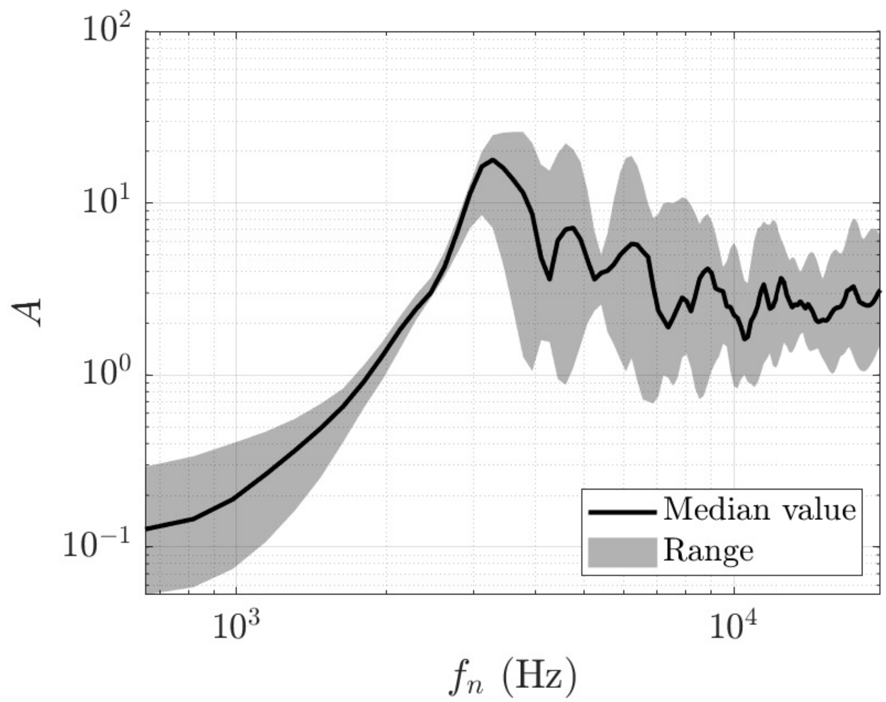

Figure 2.11. Ratio of the energy at the receiver location with modeled reflection from the tank walls and surface to the energy that would be expected from free-field propagation, A, as a function of the bubble natural frequency f_n. The shaded area shows the range of values obtained for the possible range of source locations on the surface of the ice. The solid line represents the median value among the tested source locations for each frequency f_n.

location, and once at each vertex of a cube with side length 10 cm centered at the nominal source location. The range of correction factor values A computed for the various source locations at each frequency f_n is indicated by the gray shaded area in Fig. 2.11, while the median value is indicated by the solid black line. This range is taken to be the asymmetric uncertainty in the correction factor $\Delta^{+}A(f_n)$ and $\Delta^{-}A(f_n)$.

The block of ice itself is not included in our propagation modeling. This omission is certain to result in some additional uncertainty in $A(f_n)$ which is not captured by our modeling efforts. However, the block of ice is small (10 cm) relative to the wavelength of the sound for the frequencies at which melt noise is concentrated (1-3 kHz (Pettit et al., 2015) corresponding to wavelengths of 0.5-1.5 m). Given the other uncertainties present and the scatter that exists in the data, we do not believe that the results presented here would be qualitatively altered by the inclusion of a more sophisticated model for the propagation of sound in the tank.

2.12 Appendix D: Potential energy uncertainty

Since the estimates of V_m and P_0 are not independent, we first use Eq. 2.33 to write Eq. 2.35 in terms of the measured variable V_m, the uncertainty of which is assumed to dominate. This gives the following equation for Φ_m:

$$\Phi_m = \frac{P_\infty G_m}{\gamma - 1}\left(1 - \left(\frac{V_m}{G_m}\right)^{\frac{\gamma-1}{\gamma}}\right). \tag{2.65}$$

Here, P_∞ is the far-field pressure in the water, G_m is the gas content per unit mass in the ice, and $\gamma = 7/5$ is the ratio of heat capacity at constant pressure to heat capacity at constant volume for air. Differentiating this expression with respect to V_m and making use of Eq. 2.33 yields:

$$\frac{\partial \Phi_m}{\partial V_m} = -\frac{P_\infty}{\gamma}\left(\frac{P_0}{P_\infty}\right)^{\frac{1}{\gamma}}. \tag{2.66}$$

The uncertainty in Φ_m can then be written as

$$\Delta\Phi_m = \left| \frac{\partial \Phi_m}{\partial V_m} \Delta V_m \right|, \tag{2.67}$$

$$= \frac{P_\infty}{\gamma} \left(\frac{P_0}{P_\infty} \right)^{\frac{1}{\gamma}} \Delta V_m. \tag{2.68}$$

2.13 Appendix E: Effect of origin depth of the ice

From the measurements of the bubble sizes in the ice described in Section 2.4.1, it is possible to estimate the density of the samples of ice ρ_{sample}. The density of a given sample of ice will be given by

$$\rho_{\text{sample}} = \frac{m_{\text{ice}} + m_{\text{air}}}{V_{\text{ice}} + V_{\text{air}}}, \tag{2.69}$$

where m_{ice} is the mass of the ice, m_{air} is the mass of the air contained in the ice, V_{ice} is the total volume occupied by ice (excluding the air bubbles), and V_{air} is the total volume of the air bubbles contained in the sample of ice. We assume that m_{air} is negligible, and set $m_{\text{ice}} = 1$ kg. We then note that $V_{\text{air}} = V_m m_{\text{ice}}$, where V_m is the total bubble volume in m^3 per kg of ice. Also, note that $V_{\text{ice}} = m_{\text{ice}}/\rho_{\text{pure}}$ where $\rho_{\text{pure}} = 917$ kg m^{-3} is the density of pure ice. The density of the sample of ice can then be computed as

$$\rho_{\text{sample}} = \left(\frac{1}{\rho_{\text{pure}}} + V_m \right)^{-1}. \tag{2.70}$$

Equation 2.70 can be used to estimate the density of each of the samples of ice used in the experiment.

An estimate of the depth of origin, D, in meters for the ice can be made from the estimates of the density. Table 1 of Gow (1968) presents depth vs. density data for ice from a core drilled at Byrd station in Greenland. We interpolate between the points on that table to generate a depth-vs-density curve which can then be used to estimate an origin depth, D, in meters for each of the samples of ice in our experiment. This depth vs. density data is from an accumulation zone

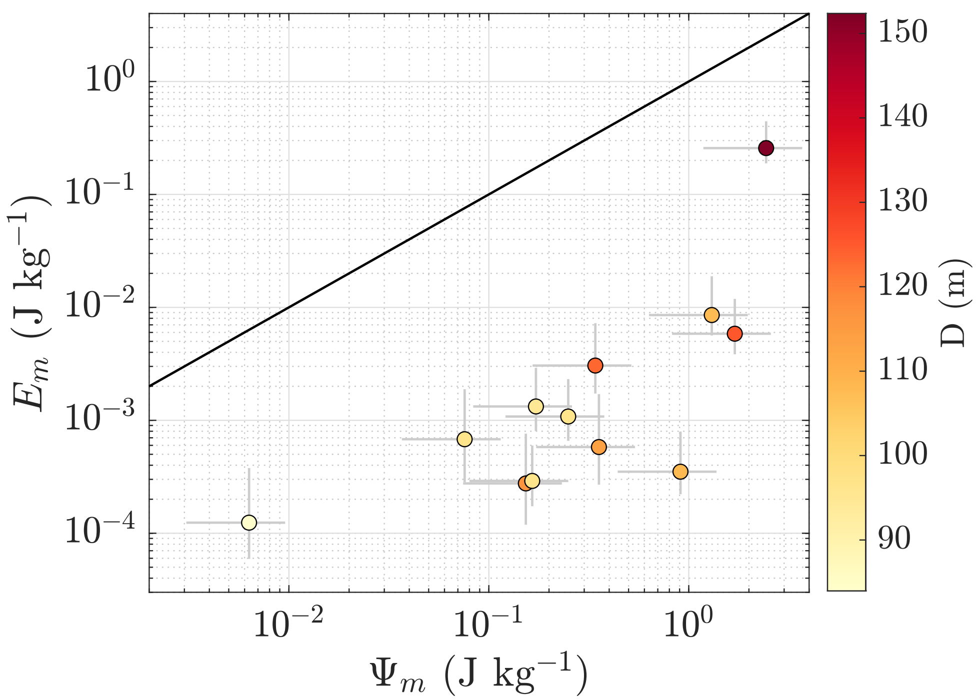

Figure 2.12. Estimates of the total mass-normalized acoustic energy E_m vs. the total mass-normalized modeled energy Ψ_m for pieces of ice in the controlled melting experiments, colored by estimated origin depth of the ice D. Each point represents one piece of ice that was melted. The solid black line represents 100% conversion of maximum modeled energy Ψ_m into acoustic energy E_m.

in Greenland, and may not be perfectly representative of the relationship at tidewater glaciers in Hornsund Fjord, Svalbard, where the ice analyzed here was collected from. However, we should expect the sorting of origin depths calculated using this data should at least be correct.

Figure 2.12 presents the acoustic energy E_m vs. the modeled energy Ψ_m for each of the pieces of ice studied here, as in Fig. 2.8, but colored by the estimated origin depth D. It is clear from this figure that the origin depth D is somewhat correlated with both the modeled energy Ψ_m and the acoustic energy E_m, with the loudest and most energetic piece of ice having the greatest estimated origin depth and the quietest and least energetic ice having the smallest estimated origin depth. However, for the rest of the pieces of ice, the origin depth D is more closely correlated with the modeled energy Ψ_m than it is with the acoustic energy E_m, and it does not in general explain the variability in E_m for points with comparable values of Ψ_m.

Chapter 3

Modification of the size distribution of bubbles upon their release from glacier ice into the water

3.1 Introduction

Air bubbles trapped in glacial ice are released into the water as the ice melts (Josberger, 1980; Urick, 1971). It has been demonstrated in laboratory experiments that the presence of these bubbles in the boundary layer enhances the turbulent kinetic energy in the water, resulting in enhanced heat flux across the boundary layer and increasing the rate of melting of the ice by a factor of 2 relative to a control test with bubble-free ice (Wengrove et al., 2023). It has also been shown that, for a fixed volume flux of gas, the size distribution of bubbles rising through water next to a vertical plate influences the heat transfer coefficient, with smaller bubbles resulting in increased heat transfer (Kitagawa et al., 2009). It therefore stands to reason that the size distribution of the bubbles released into the water from melting glacier ice will influence heat transfer across the boundary and submarine melt rates.

While there are examples of median or average bubble sizes (Scholander and Nutt, 1960; Gow, 1968, 1971; Gow and Williamson, 1975) and size distributions (Lipenkov, 1968; Bendel et al., 2013; Narita et al., 1999) for bubbles in glacial ice in the published literature, we are not aware of any published measurements of the size distributions of bubbles after they have

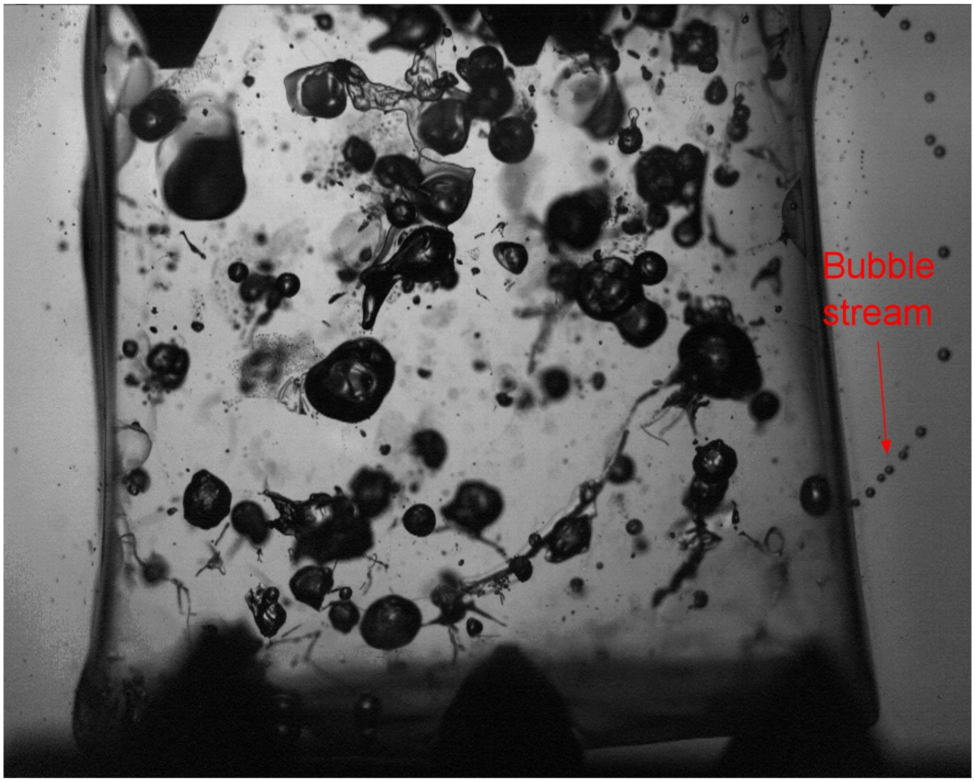

Figure 3.1. Example image of a piece of glacier ice in which a stream of small bubbles can be seen being released into the water. The piece of ice in the image is about 3 cm across.

been released into the water. An obvious first approximation is to take the size distributions and pressures of bubbles in the ice and assume that each bubble expands until it reaches equilibrium with the water. However, this precludes the possibility of bubbles being released as streams of smaller bubbles, or fragmenting upon their release into the water. Anecdotal observations of bubbles released from melting glacier ice made by the authors of this study (Fig. 3.1), and observations published in the supporting information of Pettit et al. (2015), suggest that at least some bubbles are released from the ice as streams of smaller bubbles, or fragment into multiple bubbles upon their release. Depending on how common these processes are, they have the potential to result in a substantial alteration in the size distribution of the bubbles in the water compared to the distribution that would be obtained by assuming every bubble remains intact upon its release into the water.

Bubbles released from glacier ice generate sound as a result of being driven into breathing-mode oscillations (Urick, 1971; Pettit et al., 2015; Deane et al., 2019). Because there is an established relationship between the radius of an air bubble in water and the frequency at which it oscillates (Minnaert, 1933), it is possible to use the acoustic emissions of bubbles to estimate their size. This technique was employed to measure the size distribution of bubbles released from a nozzle by. Vazquez et al. (2005), and was found to perform well when compared to more standard methods of bubble size estimation in water. In this paper, we make use of the acoustic emissions of bubbles released from glacier ice to measure the sizes of the resulting bubbles in the water.

The goal of this paper is not only to measure the size distributions of bubbles released from glacier ice in the water but also to investigate the extent to which they vary from what would be expected based on simple expansion of the bubbles. Section 3.2 provides a description of the data and methods used. This includes images of the ice analyzed to determine the size distributions in the ice (Section 3.2.2), and acoustic data used to measure the size distributions in the water (Section 3.2.5). The results are presented in Section 3.3, along with a comparison of the size distributions in the ice and water. The implications of these results are then discussed in 3.4, and Section 3.5 presents concluding remarks.

3.2 Data and methods

This chapter makes use of much of the same data that was described and used in Chapter 2. Portions of the data that are used only in this study are described here, and some aspects of the data that were described briefly in Chapter 2 but are of particular importance to the analysis of this chapter are described here in greater detail. For a full description of the experimental setup, refer to Section 2.4 in Chapter 2.

We shall often refer to the bubble size distribution, both in the ice and water. What is meant by this is the number of bubbles per radius increment per unit mass of ice (either containing the bubbles, or from which the bubbles were released). We refer to this quantity as

$n(R)$, with various subscripts, and its units are $\mathrm{m}^{-1}\ \mathrm{kg}^{-1}$.

3.2.1 Experiment overview

Small (liftable by hand) pieces of ice that were floating in the fjord near the termini of several glaciers in Hornsund Fjord, Svalbard were collected and brought back to the Polish Polar Station (20-60 minutes by small boat) to be used in the experiment. The pieces of ice were cut using an electric chainsaw, producing thick blocks about 10 cm by 10 cm by 5 cm and adjacent thin slices of ice about 10 cm by 10 cm by 0.5-1 cm. Backlit images of the thin slices of ice were used to estimate the bubble size distributions in the ice, and the total bubble volume per unit mass of ice. The thick blocks of ice were used in controlled melting experiments, in which the gas content of the ice was measured directly by collecting the gas with a funnel, and the acoustic emissions of the ice as it melted were recorded with a hydrophone placed in the tank.

3.2.2 Estimating bubble size distributions in the ice

The bubble size distributions in the ice were estimated by analyzing images of thin (0.5-1 cm thick) slices of ice. Each thin slice of ice was placed on a backlit stage with a camera positioned directly above it looking down. A scale bar was placed next to the ice, within the frame of the image, in order to calibrate the image and determine sizes in physical units. Using the software ImageJ, the outline of each bubble was traced manually, and the area bounded by this outline, a, and the position of the bubble within the image, were saved. Figure 3.2 shows an example image of a thin slice of ice with the outlines of identified bubbles overlaid in pink.

The radius of each bubble R is assumed to be given by the cross-sectional area equivalent radius, which can be computed from the identified area in the image as

$$R = \sqrt{\frac{a}{\pi}}. \tag{3.1}$$

The mass-normalized bubble size distribution $n_{\mathrm{ice}}(R)$, with units of $\mathrm{m}^{-1}\ \mathrm{kg}^{-1}$, can then be

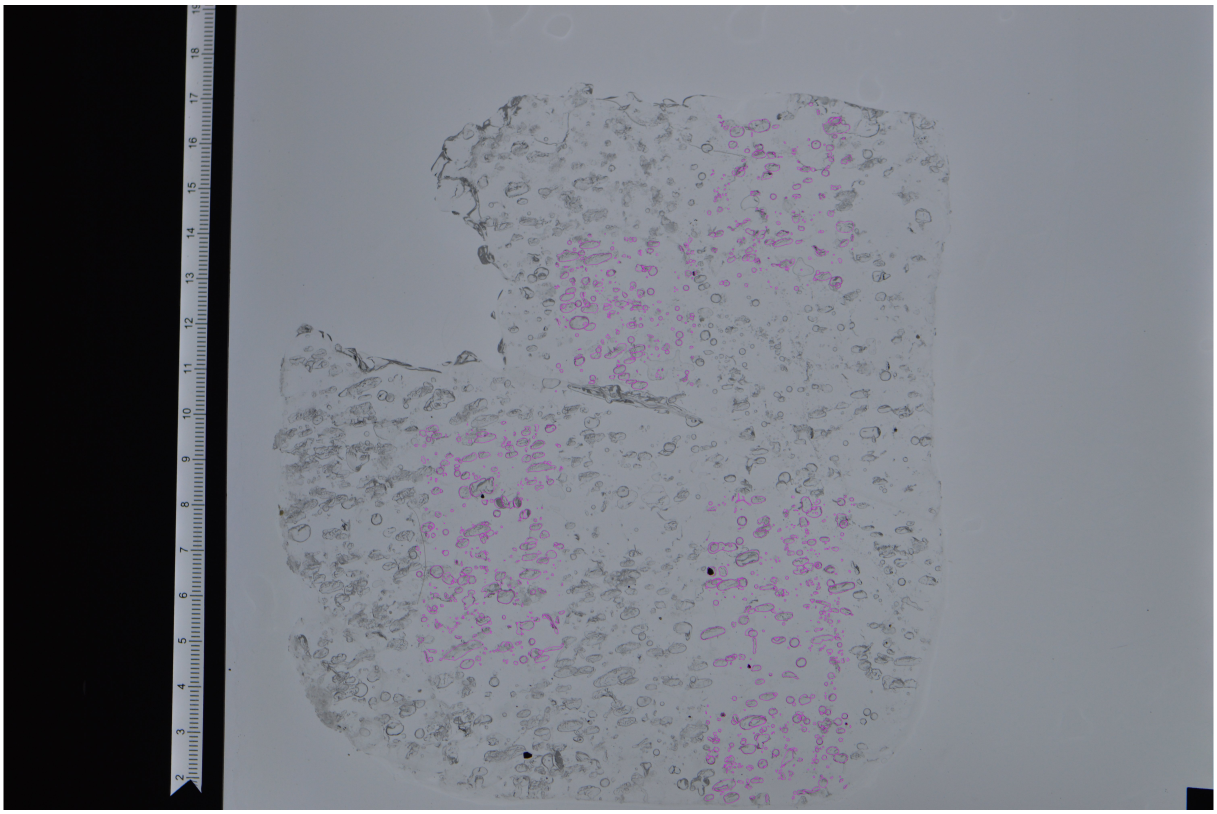

Figure 3.2. Example of a thin section of ice used to identify bubbles in the ice and estimate the distribution of their sizes. The scale bar used to calibrate the image to obtain bubble sizes in physical units is visible on the left side of the image. The outline of each identified bubble is drawn in pink and overlaid on the image. For this image, four distinct rectangular subsections were chosen to obtain a sample of the bubble size distribution, which is assumed to be representative of that for the whole piece of ice.

computed as

$$n_{\text{ice}}(R) = \frac{\mathbf{P}_{\text{c}}(R) N_c}{m_{\text{thin}} F_c}. \tag{3.2}$$

Here, $\mathbf{P}_{\text{ice}}(R)$ is the probability density function of the size distribution of the counted bubbles, N_c is the total number of counted bubbles, m_{thin} is the measured mass of the this slice of ice in which the bubbles were counted, and F_c is the fraction of the area of the thin slice of ice in which the bubbles were counted. Note that the units of n_{ice}, number of bubbles per m of radius increment and per kg of ice, are non-standard in acoustic bubble size literature; we have chosen these units for ease of comparison between size distributions in the ice and water.

For spherical bubbles, using the two-dimensional area to compute the bubble radius as in Eq. 3.1 results in the correct value for the radius of the bubble, and the formula

$$v = \frac{4}{3}\pi R^3 \tag{3.3}$$

gives an accurate calculation of the volume of the bubble. However, for non-spherical bubbles, the result can be either an over- or under-estimation of the bubble volume v. On average, there may be some cancellation of over- and under-estimation errors, but it is unlikely to be complete, and there may be some remaining bias in the size estimates of the bubbles. The resolution of the images was sufficient to reliably identify bubbles with radii $R \geq 0.2$ mm.

While many bubbles in the images can be identified with confidence, there are some cases in which it is not entirely obvious from the two-dimensional image which structures are bubbles filled with air and which are not. Phenomena such as water bags around bubbles, as described by Bader (1950), and the presence of irregularly shaped or overlapping bubbles sometimes make interpretation of the image challenging. Errors introduced as a result of incorrect interpretations of these scenarios are difficult to quantify. We have found that when two different people identify bubbles in the same image, the resulting size distributions agree within a factor of 2 at each increment of radius R, with a better agreement for the total volume of all bubbles. Of course, this does not account for instances in which the same incorrect interpretation was made by both people.

For two of the images of ice, every bubble visible in the image was identified (1870 in one image and 5247 in the other). This corresponds to $F_c = 1$ in Eq. 3.2. By generating hypothetical sub-samples of these two pieces of ice, it was determined that identifying about 1000 total bubbles across several rectangular sub-sections of the image produced a sufficiently accurate estimate of the bubble size distribution for the whole image. The bubble size distribution resulting from a sub-sample of this type was within a factor of 2 of the distribution for the whole image at any given radius increment R, and produced an estimate of the total bubble volume per unit area of image analyzed that was within 20% of that obtained from the full image analysis. This sub-sampling procedure was therefore applied to the remained of the images analyzed.

3.2.3 Estimating average bubble pressure

The average pressure of the gas contained within the bubbles in the ice can be calculated by combining the bubble size distribution measurements with the measurements of the gas content collected from the melting ice. The total bubble volume per unit mass of the ice for an imaged thin slice of ice can be computed by integrating the bubble size distribution,

$$V_m = \int_{R_{\min}}^{R_{\max}} \frac{4}{3}\pi R^3 n_{\text{ice}}(R)dR. \tag{3.4}$$

The total gas volume at atmospheric pressure released by a thick block of ice as it melted was measured directly by a gauge connected to funnel placed over the block of ice, and dividing this volume by the mass of the melted block of ice that melted during the experiment, m_{thick}, gives the gas content of the ice per unit mass, G_m. With the assumption that the bubble volume per unit mass V_m measured from a thin slice of ice is representative of V_m for the adjacent thick block of ice that was melted, the average pressure in the bubbles in the ice P_0 can be computed as

$$P_0 = P_{\mathrm{atm}} \frac{G_m}{V_m}. \tag{3.5}$$

One of the thin slices of ice for which the bubble size distribution, and bubble volume V_m, were estimated was adjacent to two thick blocks of ice that were melted (one on each side). The difference between the measured gas content of those two thick blocks of ice was about 10%, suggesting that the assumption of consistency in V_m and G_m between adjacent pieces of ice introduces an error of 10% into the estimate of pressure P_0.

3.2.4 Transformed bubble size distributions

The mass-normalized bubble size distributions in the ice $n_{\mathrm{ice}}(R)$ and the average bubble pressure P_0 can be combined to calculate expected bubble number distributions when the bubbles reach atmospheric pressure. This assumes that all bubbles in the ice were at the average pressure P_0, and that all of the bubbles remain intact as a single bubble as they expand. We calculate two such distributions: one representing the estimated bubble size distribution of the bubbles upon their formation, and a second representing the estimated bubble size distribution of the bubbles upon their release into the water. In both cases, we make use of Eq 3.6 to compute the bubble radius once it reaches equilibrium at atmospheric pressure P_{atm},

$$R_{\mathrm{eq}} = R \left(\frac{P_0}{P_{\mathrm{atm}} + \frac{2\sigma}{R_{\mathrm{eq}}}} \right)^{\frac{1}{3\kappa}} \tag{3.6}$$

(see Section 2.9 for a derivation). Here, R is the initial radius of the bubble in the ice, σ is the surface tension of water, and κ is the polytropic index for the expansion of the gas. In general, this equation must be solved iteratively for R_{eq}.

To estimate the bubble size distribution upon formation of the bubbles, we take $\kappa = 1$, corresponding to isothermal expansion of the gas, and set $\sigma = 0$, since there is no surface tension acting on the bubbles in the ice. This can be thought of as reversing the gradual isothermal compression of the bubbles under the overburden pressure acting on the ice as it flowed through the glacier and attained its eventual pressure. We refer to this size distribution, normalized per unit mass of ice, as $n_{\mathrm{iso}}(R)$. With R_eq computed from R using equation 3.6 with $\kappa = 1$ and $\sigma = 0$, n_{iso} can be computed as:

$$n_{\mathrm{iso}}(R_{\mathrm{eq}}) = n_{\mathrm{ice}}(R). \tag{3.7}$$

To estimate the bubble size distribution upon release of the bubbles into the water, we take $\kappa = 7/5$, corresponding to adiabatic expansion of the gas, and $\sigma = 0.076$ N m^{-1} as the surface tension of sea water at 0 °C (Nayar et al., 2014). We refer to this size distribution, normalized per unit mass of ice that contained the bubbles, as $n_{\mathrm{adi}}(R)$. With R_eq computed from R using equation 3.6 with $\kappa = 7/5$ and $\sigma = 0.076$ N m^{-1}, n_{adi} can be computed as:

$$n_{\mathrm{adi}}(R_{\mathrm{eq}}) = n_{\mathrm{ice}}(R). \tag{3.8}$$

3.2.5 Estimating bubble size distributions in the water

A hydrophone was placed in the tank during the melting experiments in order to record the acoustic emissions of the melting ice. This enabled the acoustic energy radiated by the ice per unit mass, E_m, to be calculated, as is described in detail in Sections 2.4.2 and 2.11 of Chapter 2. The acoustic data can also be used to estimate the size distribution of the bubbles that are released into the water as the ice melts. As was discussed at great length in Chapter 2, the release of pressurized bubbles from the ice into the water results in volume-mode oscillations of the bubble, which generate sound. The acoustic signatures generated by the release of bubbles are the primary feature visible in the acoustic pressure timeseries, as can be seen in Fig. 3.3 panels **a** and **b**. These acoustic signatures typically resemble a decaying sinusoidal pulse, as is expected for a bubble in water.

The sampling frequency of the acoustic recorder was 96 kHz. A high pass filter with a 1 kHz pass band frequency was applied to the acoustic data to eliminate low-frequency noise caused by a recirculation pump next to the tank and possible other sources in the environment. An event detection algorithm was then run on the filtered data. The start of an event was triggered when the variance in the signal computed over a 100 sample (1.04 ms) moving window exceeded a set threshold, and the end of the event was triggered when the variance over a 200 sample moving window fell below this same threshold. The window lengths and threshold level were tuned by iteratively adjusting them and inspecting the output. The final parameters used were chosen to include as many events as possible while avoiding the inclusion of low-amplitude fluctuations that do not visually resemble acoustic emissions of oscillating bubbles. An additional criterion applied to events with peak frequencies greater than 2 kHz was that events with a duration longer than 100 times the corresponding natural period of the peak frequency oscillation were excluded, on the grounds that the oscillations of large bubbles generally decay much more rapidly than this. This criterion resulted in the exclusion of a relatively small number of acoustic events, the timeseries of which did not resemble bubble pulses.

A spherical bubble in free space will oscillate at its undamped natural frequency, which is given by

$$f_n = \frac{1}{2\pi R_{\mathrm{eq}}}\sqrt{\frac{1}{\rho}\left(3\kappa P_\infty + (3\kappa - 1)\frac{2\sigma}{R_{\mathrm{eq}}}\right)}, \tag{3.9}$$

where R_{eq} is the equilibrium radius of the bubble, P_∞ is the far-field pressure in the water, $\rho = 1025$ kg m^{-3} is the density of the water, $\kappa = 7/5$ is the polytropic index of the gas, and $\sigma = 0.076$ N m^{-1} is the surface tension of sea water (Minnaert, 1933; Leighton, 1994). The influence of damping on the natural frequency has been neglected here. By computing the power spectral density of each individual acoustic event in the timeseries and determining its peak frequency, as demonstrated in Fig. 3.3c, the natural frequency of each bubble can be estimated. The equilibrium radius R_{eq} of the bubble in the water can be calculated iteratively using Eq. 3.9. Performing this procedure for every acoustic event in the acoustic timeseries for each block of ice that was melted, we can obtain the probability density function of the bubble sizes from the acoustic estimate, $\mathbf{P}_a(R)$. The bubble size distribution in the water, normalized by the mass of ice that melted m_{thick}, can then be computed as

$$n_{\text{water}}(R) = \frac{\mathbf{P}_a(R) N_a}{m_{\text{thick}}}. \tag{3.10}$$

The units of $n_{\text{water}}(R)$ are $\mathrm{m}^{-1}\ \mathrm{kg}^{-1}$, or number of bubbles per meter radius increment per kilogram of ice that melted to release the bubbles. We use these units to enable direct comparison with the actual and transformed bubble size distributions in the ice. An estimate of the bubble size distribution normalized per unit volume in the water could be made by dividing n_{water} by the density of the ice to get bubble number density per unit volume of ice, multiplying by the melt rate to get the number density of bubbles released from the ice per unit area per unit time, and then incorporating the bubble rise speeds in the water as a function of bubble radius.

The acoustic technique for determining the bubble size distribution in the water has several limitations. First, it requires a bubble to generate sound in order to be detected. The results presented in Section 3.3.3 suggest that, for loud ice with high values of acoustic energy E_m and average bubble pressure P_0, most of the bubbles do radiate enough sound to be detected. However, for ice that is quieter and has lower average bubble pressures, it is likely that some bubbles are released too quietly to be detected, resulting in an underestimate of $n_{\text{water}}(R)$.

Second, it is also possible for noise generated by non-bubble sources to be erroneously detected as bubbles. While the data was filtered and the event detector parameters were selected in an effort to minimize false positives, there is an inherent tradeoff between detecting quiet bubbles and excluding non-bubble noise that must be balanced.

Third, it assumes that each acoustic event in the timeseries is the result of a single oscillating bubble. In reality, a single bubble in the ice can turn into multiple bubbles in the water. If a large bubble escapes from the ice as a sequential stream of smaller bubbles, one after the other, then the acoustic technique can successfully identify these bubbles. However, if a large bubble in the ice explodes into the water and fractures into multiple bubbles that oscillate

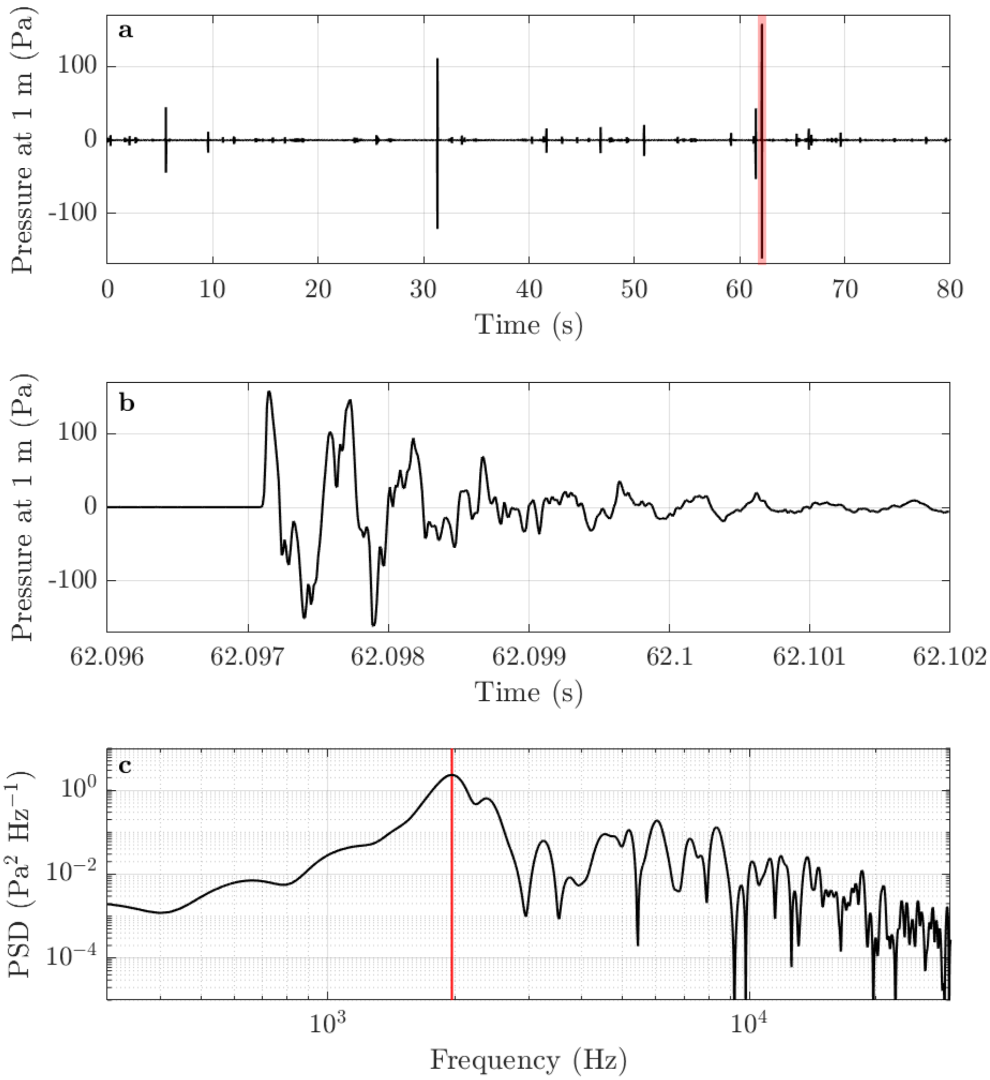

Figure 3.3. Example showing the identification of an acoustic event in the pressure timeseries and the determination of its peak frequency. **a** An 80 second segment of the pressure timeseries recorded by the hydrophone during one of the melting experiments, with one acoustic event highlighted in red. **b** An expanded view of the highlighted event. While there are additional frequency components present, the overall behavior resembles a decaying sinusoidal pulse, which is consistent with the expected acoustic emissions from an oscillating bubble. **c** The power spectral density of this acoustic event, which exhibits a clear peak at about $f_p = 2.0$ kHz, denoted by the vertical red line. This corresponds to a bubble with an equilibrium radius of about $R = 1.6$ mm.

simultaneously, this will be counted as a single bubble with a radius corresponding to whatever frequency is dominant in the resulting superposition of acoustic signatures, also resulting in an underestimate of $n_{\text{water}}(R)$.

Fourth, the acoustic technique can produce an incorrect estimate of the size of a successfully detected bubble for two reasons. Equation 3.9 assumes a spherical bubble oscillating in free space, but the presence of a solid boundary (the ice) next to a bubble can result in a reduction in its natural frequency of up to about 10% depending on its distance from the wall (Strasberg, 1953). This will result in an overestimate of the bubble radius R of up to 10%, and an overestimate of the bubble volume v of up to 30%. There is also resonant structure in the tank which results in the amplification of some frequencies and the suppression of others, as described in detail in Sections 2.4.2 and 2.11 of Chapter 2. While we have corrected for the influence of this reverberation on the observed energy of the acoustic events, as described in those sections, we have not made an attempt to correct for shifts in the peak frequency of acoustic events that may occur as a result of reverberation in the tank. We believe that the uncertainty in the position of each bubble when it is released, combined with the effects of the nearby solid boundary, would make this a fraught exercise. We have, however, denoted and commented on the peaks in the resonant structure in the following analysis.

3.3 Results

3.3.1 Bubble size distributions in the ice

The mass-normalized bubble size distributions in the ice $n_{\text{ice}}(R)$ are shown in Fig. 3.4a. For all blocks of ice, the density of bubbles decreases with increasing bubble radius R. The size distributions display a clear relationship with the estimated bubble pressure P_0. Blocks of ice with lower bubble pressure have less steeply sloped distribution curves, and both more bubbles at a given radius for $R > 0.8$ mm and a larger maximum bubble radius.

The estimated mass-normalized bubble size distributions of the ice upon formation $n_{\text{iso}}(R)$

are shown in Fig. 3.4b. These size distribution curves show more consistency between blocks than $n_{\text{ice}}(R)$, and no clear sorting with pressure. Instead, the $n\text{iso}(R)$ curves have collapsed onto a common size distribution resembling that of $n_{\text{ice}}(R)$ for the blocks of ice with $P_0 \approx P_{\text{atm}}$.

3.3.2 Bubble size distributions in the water

The expected mass-normalized bubble size distributions in the water $n_{\text{adi}}(R)$, for each block are shown in Fig. 3.5a. These curves are similar to those for the isothermally expanded bubbles $n_{\text{iso}}(R)$ in Fig. 3.4b, but the adiabatic expansion results in slightly smaller final bubble sizes for $n_{\text{adi}}(R)$. This means that the blocks with higher bubble pressure (which are also generally louder, with higher values of E_m) tend to have a slightly lower density of larger ($R > 1$ mm) bubbles than the quieter, lower pressure blocks.

The bubble size distributions measured in the water with the acoustic technique normalized by the mass of the ice melted, $n_{\text{water}}(R)$, are shown in Fig. 3.5b. These curves display the opposite sorting to those for $n_{\text{adi}}(R)$ for large bubbles, with the louder blocks of ice having more larger bubbles and quieter blocks of ice having fewer. The single loudest block in particular stands apart from the others in this regard.

There are consistent peaks in the distributions $n_{\text{water}}(R)$ across many of the blocks at radii of $R = 0.7$ mm and $R = 1$ mm. The size distributions in the ice $n_{\text{ice}}(R)$, and the expanded distributions, do not exhibit this behavior, suggesting that it may be an artifact of the acoustic technique for bubble size estimates. Indeed, these radii correspond to acoustic event peak frequencies of about 4.7 kHz and 3.3 kHz respectively, which coincide with the first two peaks of the resonant structure in the tank, as can be seen in Fig. 2.11 of Chapter 2. The dips in $n_{\text{water}}(R)$ around these two peaks suggest that the apparent center frequency of acoustic events generated by bubbles with radii close to $R = 0.7$ mm and $R = 1$ mm is being shifted by tank resonance effects to lie on these peaks, as discussed in Section 3.2.5.

The mass-normalized bubble size distributions in the ice and water $n_{\text{ice}}(R)$ and $n_{\text{water}}(R)$, and the expected distribution in the water $n_{\text{adi}}(R)$, are all shown on the same plot for each

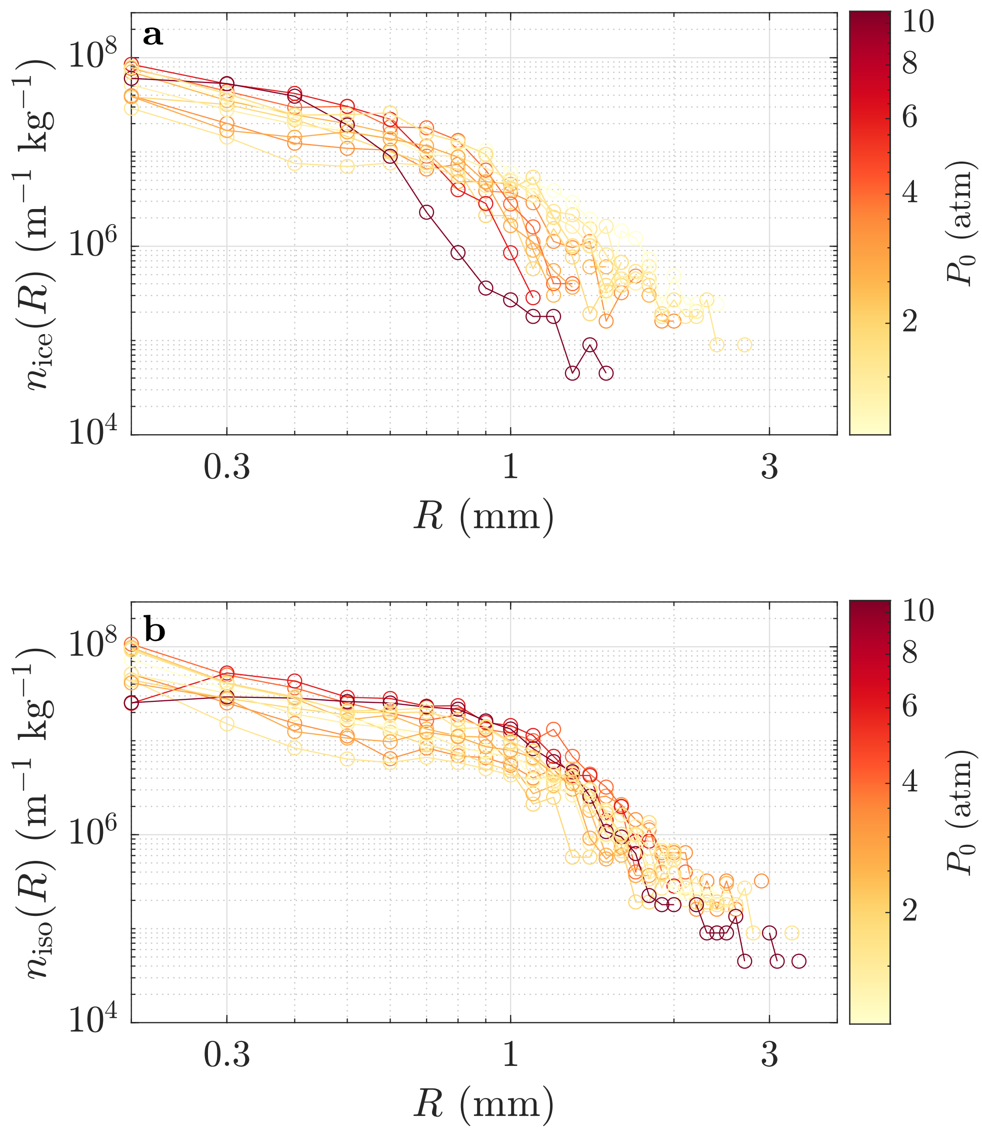

Figure 3.4. **a** Bubble size distribution curves normalized per unit mass of ice $n_{ice}(R)$, for each of the images of ice analyzed as described in Section 3.2.2. The curve for each image is colored by the average pressure in the bubbles P_0 calculated from the bubble volume in the image and the gas collected from the adjacent block as it melted, as described in section 3.2.3. The ice with higher bubble pressures tends to have fewer larger bubbles. **b** The mass-normalized bubble size distribution $n_{iso}(R)$ for each image that is obtained by taking the size distribution in the ice, $n_{ice}(R)$, and expanding each bubble isothermally ($\kappa = 1$) to its equilibrium radius at atmospheric pressure P_{atm} (with no surface tension, $\sigma = 0$). This represents the expected original size distribution when the ice was formed, if all of the bubbles were compressed equally as the ice was subjected to overburden pressure. The sorting of the distributions with pressure that is visible for $n_{ice}(R)$ is diminished for $n_{iso}(R)$.

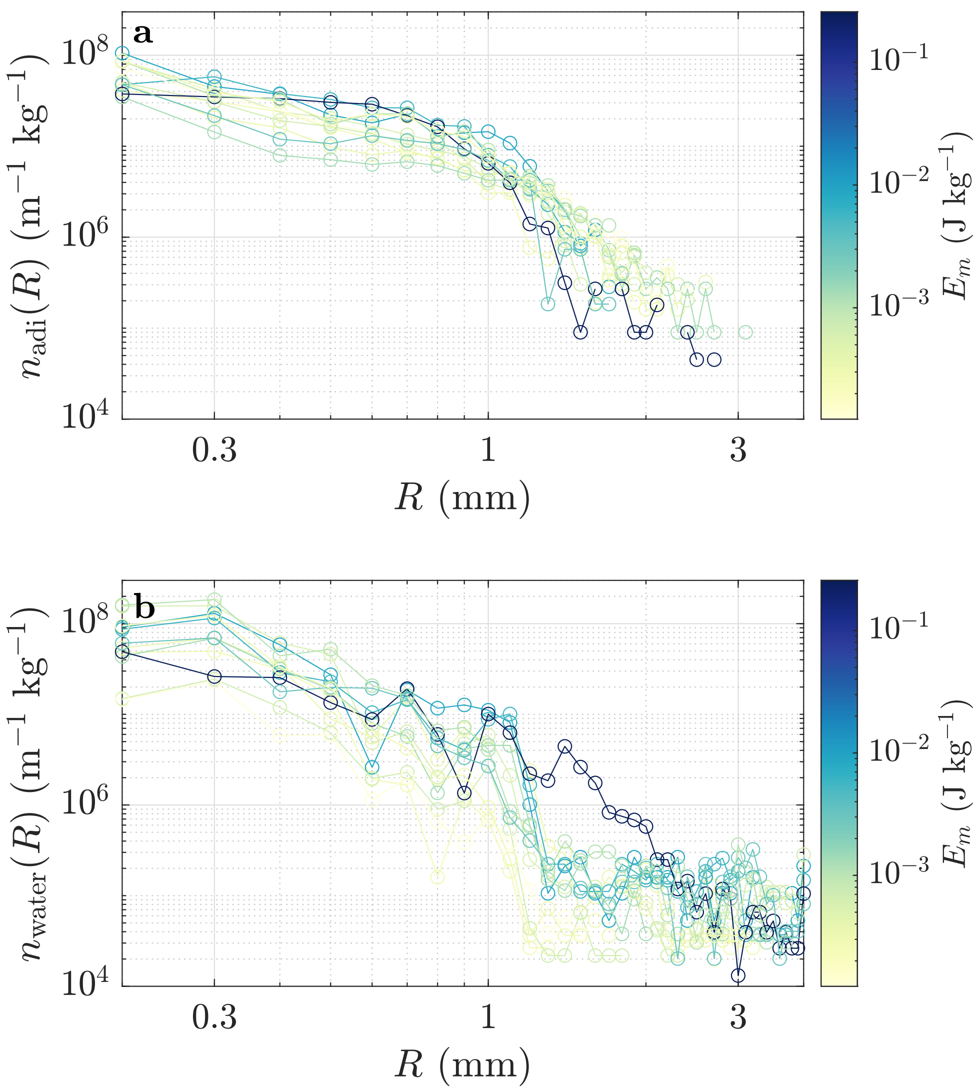

Figure 3.5. a The mass-normalized bubble size distribution $n_{\mathrm{adi}}(R)$ for each image that is obtained by taking the size distribution in the ice, $n_{\mathrm{ice}}(R)$, and expanding each bubble adiabatically ($\kappa = 7/5$) to its equilibrium radius in the water with far-field pressure $P_\infty = P_{\mathrm{atm}}$. This represents the expected size distribution of bubbles in the water if every bubble remained intact as a single bubble upon its release from the ice. **b** The bubble size distribution in the water per unit mass of ice melted, $n_{\mathrm{water}}(R)$, estimated from the acoustic emissions of the ice as it melts, as described in Section 3.2.5. There is more variability in $n_{\mathrm{water}}(R)$ than in $n_{\mathrm{adi}}(R)$ among the blocks of ice analyzed, with the loudest block of ice in particular producing many more bubbles in the range of $R = 1-2$ mm in the water than the other blocks of ice.

individual block of ice in Fig. 3.6. For the loudest blocks (earlier panels), the measured distribution in the water $n_{\text{water}}(R)$ agrees relatively well with the expected distribution in the water $n_{\text{adi}}(R)$. The quieter blocks (later panels) show a tendency for fewer larger bubbles ($R > 1$) mm in the water than the expected distribution, and more smaller bubbles ($R < 0.5$ mm) in the water than the expected distribution. This suggests that, for these quieter blocks of ice, some of the larger bubbles in the ice are breaking up into multiple smaller bubbles upon their release into the water. Panels **g** and **l** are an exception to this trend, with $n_{\text{water}}(R) < n_{\text{adi}}(R)$ for all values of R, suggesting that the acoustic technique must be undercounting the bubbles for these blocks of ice.

The largest bubbles present in the water distribution $n_{\text{water}}(R)$ are often larger than the largest bubbles present in the expected distribution $n_{\text{adi}}(R)$; there are several possible reasons for this. One explanation is that, while both distributions are normalized per unit mass of ice, the block of ice that was melted was 5-10 times larger than the adjacent thin slice of ice that was imaged, and as much as 40 times larger than the equivalent volume of that image that was analyzed to generate the $n_{\text{ice}}(R)$ and $n_{\text{adi}}(R)$ curves. It is therefore likely that the size distribution in the water captures bubbles farther along the tail of the size distribution than the distributions derived from the analysis of the ice. A second explanation is that variability in the pressure in the bubbles within a block of ice results in some bubbles in the water that are larger than expected and others that are smaller than expected. The other possibility is that some of these larger bubbles were incorrectly identified by the acoustic sizing technique.

The ratios of the measured size distributions in the water to the expected size distributions in the water, $n_{\text{water}}(R)/n_{\text{adi}}(R)$, are shown in Fig. 3.7. The blocks are divided into three groups: the loudest block (panel **a** in Fig. 3.6) is shown as its own curve in dark blue; the next two loudest blocks (panels **b** and **c** in Fig. 3.6) are combined and shown in lighter blue; and the rest of the blocks (panels **d**, **e**, **f**, **h**, **i**, **j**, and **k** in Fig. 3.6) are combined and shown in pale green. The blocks from panels **g** and **l** are excluded from this analysis on the grounds that the acoustic sizing technique is believed to have substantially undercounted the bubbles in the water for those

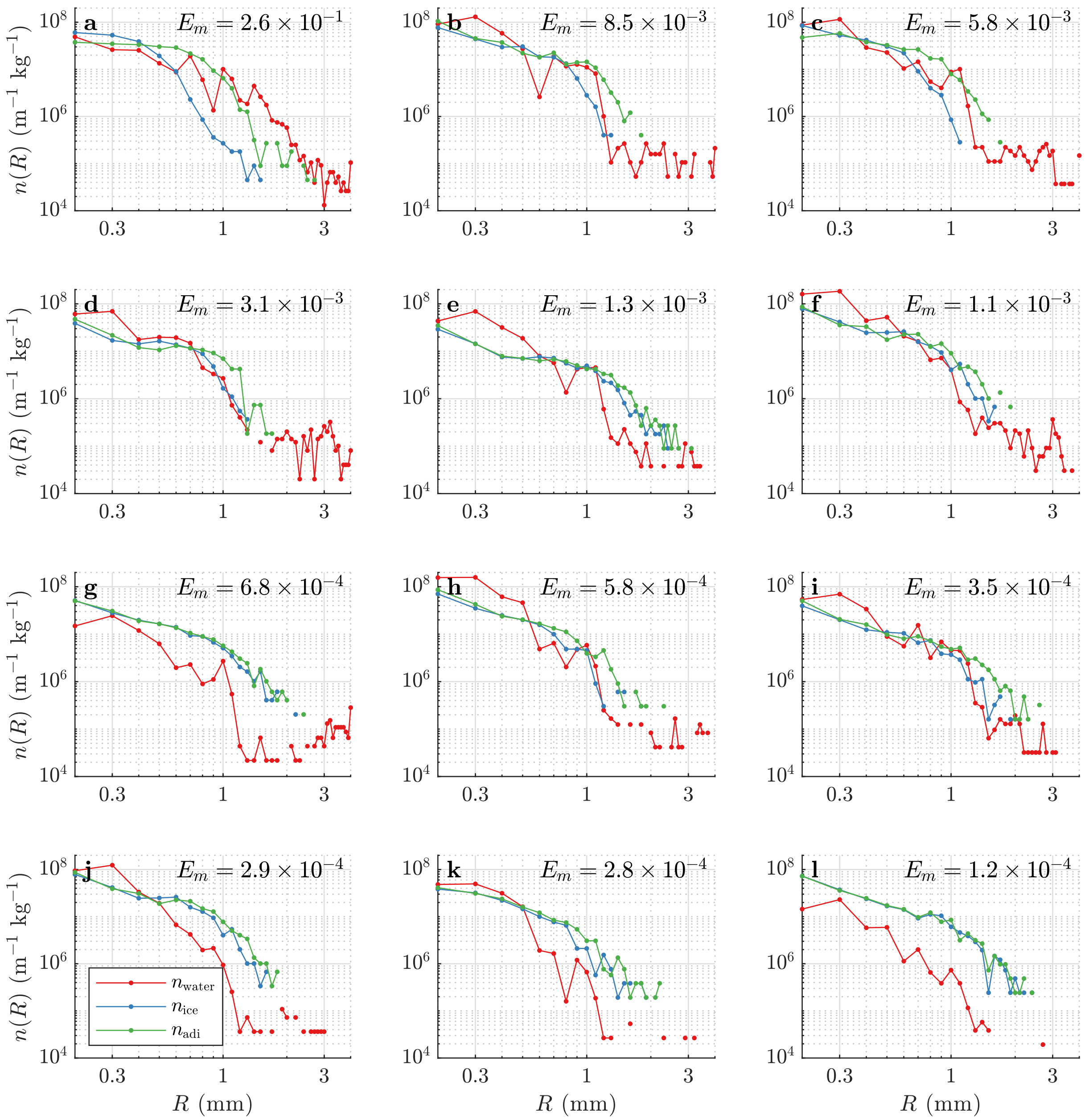

Figure 3.6. The measured mass-normalized bubble size distribution in the ice ($n_{\text{ice}}(R)$, blue), expected mass-normalized bubble size distribution in the water ($n_{\text{adi}}(R)$, green), and measured mass-normalized bubble size distribution in the water ($n_{\text{water}}(R)$, red) for each individual block of ice analyzed. The blocks are sorted by the acoustic energy radiated per unit mass of ice melted E_m, with panel **a** being the loudest and panel **l** being the quietest. The louder blocks generally show good agreement between $n_{\text{water}}(R)$ and $n_{adi}(R)$, while the quieter blocks generally show a tendency for fewer larger bubbles and more smaller bubbles in the water than expected from $n_{\text{adi}}(R)$.

blocks.

The general trend in the data is that louder blocks of ice have a ratio of $n_{\text{water}}(R)/n_{\text{adi}}(R)$ close to 1 across all radii, while quieter blocks have a ratio of $n_{\text{water}}(R)/n_{\text{adi}}(R) > 1$ for smaller bubbles (particularly around $R = 0.3$ mm) and $n_{\text{water}}(R)/n_{\text{adi}}(R) < 1$ for larger bubbles ($R > 1$ mm). This is consistent with the hypothesis that, for the louder blocks of ice, a large fraction of the bubbles in the ice are released as a single bubble into the water, while for the quieter blocks of ice, many of the larger bubbles in the ice are instead released into the water as multiple smaller bubbles. There is some noise in the data, which we attribute to a combination of tank resonances, nonuniform pressure in the bubbles, and the small number of bubbles observed with large radii.

3.3.3 Performance of the acoustic technique

As discussed in Section 3.2.5, the acoustic technique for determination of the bubble size distribution in the water has several potential sources of error. The release of bubbles silently, or of multiple bubbles simultaneously, can result in undercounting of the total number of bubbles. Conversely, the erroneous detection of noise can result in an overcounting of the number of bubbles.

The ratio of the total number of bubbles per unit mass of ice,

$$N = \int_{R_{\min}}^{R_{\max}} n(R)dR, \tag{3.11}$$

in the water to the total number per unit mass in the water for each block of ice melted is shown in Fig. 3.8a. If all of the bubbles are correctly identified in the water, then we should always have $N_{\text{water}}/N_{\text{ice}} \geq 1$. If all bubbles in the ice are released into the water as a single bubble, then $N_{\text{water}}/N_{\text{ice}} = 1$. This is approximately true for the loudest block of ice. As the ice gets quieter and the fraction of bubbles released into the water slowly increases, we expect that more bubbles will be split into multiple smaller bubbles in the water, and $N_{\text{water}}/N_{\text{ice}}$ should increase. Indeed, the ratio does increase initially with decreasing acoustic energy E_m, but two of the quieter blocks

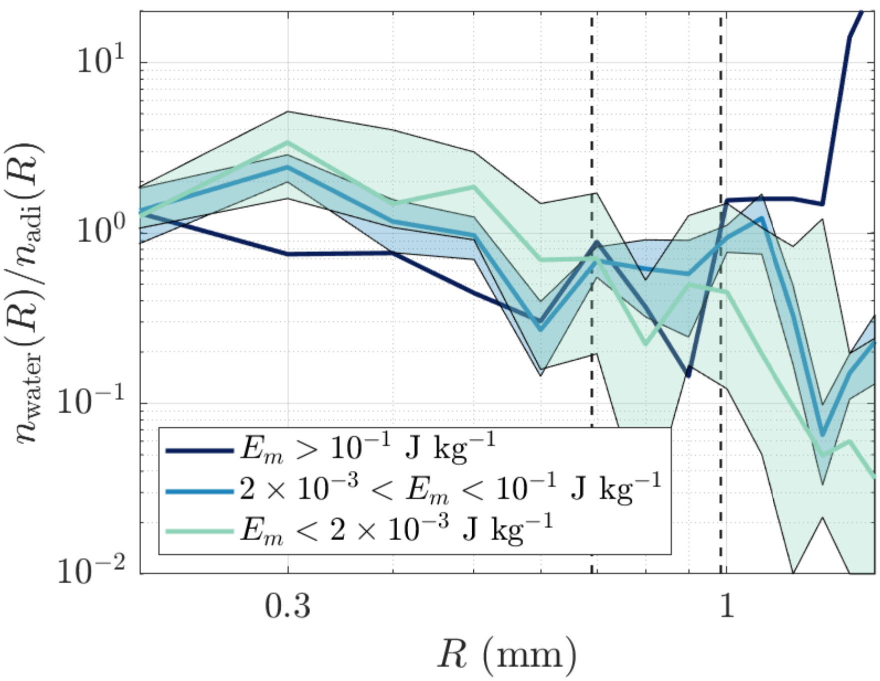

Figure 3.7. Ratio of the size distributions of the bubbles in the water to the expected distribution, $n_{\mathrm{water}}(R)/n_{\mathrm{adi}}(R)$. The single loudest block is shown as its own curve (dark blue). The next two loudest blocks, with acoustic energies in the range of $2 \times 10^{-3} < E_m < 10^{-1}$ J kg^{-1}, are represented by lighter blue, with their median (and average) shown as the solid line and their range represented by the shading. The quieter blocks, with acoustic energies of $E_m < 2 \times 10^{-3}$ J kg^{-1}, are shown in pale green, with their median represented by the solid line and their range represented by the shading. The two blocks of ice for which $N_{\mathrm{water}}/N_{\mathrm{ice}} < 0.5$, which correspond to panels **g** and **l** in Fig. 3.6, are excluded on the grounds that the acoustic bubble detection performed poorly for those blocks. The two most prominent resonances in the tank are denoted by the vertical dashed lines. The louder blocks of ice tend to have a ratio of $n_{\mathrm{water}}(R)/n_{\mathrm{adi}}(R)$ closer to 1 across all values of R, while quieter blocks tend to have lower values of $n_{\mathrm{water}}(R)/n_{\mathrm{adi}}(R)$ for $R > 1$ mm and higher values of $n_{\mathrm{water}}(R)/n_{\mathrm{adi}}(R)$ for $R < 0.5$ mm, suggesting that some large bubbles in the ice are being released as multiple smaller bubbles.

(panels **f** and **i**) have $N_{\text{water}}/N_{\text{ice}}$ substantially lower than 1. This suggests that, for quieter pieces of ice, the fraction of bubbles that are successfully detected acoustically decreases, resulting in an undercounting of bubbles.

The ratio of the total volume of bubbles per kg of ice melted in the water,

$$V_{\text{water}} = \int_{R_{\min}}^{R_{\max}} \frac{4}{3}\pi R^3 n_{\text{water}}(R)dR, \tag{3.12}$$

to the total volume of gas per kg of ice melted collected in the funnel is shown for each block of ice in Fig. 3.8b. If all bubbles are identified correctly in the water, then this ratio should be $V_{\text{water}}/V_{\text{collected}} = 1$. Bubbles with their frequencies incorrectly identified can contribute to either increasing or decreasing this ratio. The erroneous detection of noise will lead to $V_{\text{water}}/V_{\text{collected}} > 1$, while the failure to detect bubbles that are too quiet will lead to $V_{\text{water}}/V_{\text{collected}} < 1$. For the loudest block of ice, this ratio is very close to one, suggesting that the acoustic technique is performing well. For blocks with lower acoustic energy E_m, the ratio $V_{\text{water}}/V_{\text{collected}}$ tends to be lower, falling as low as 0.06 for the quietest block of ice. This suggest that, for these blocks of ice, many of the bubbles released into the water are too quiet to be detected.

3.4 Discussion

The bubble size distribution data presented in Fig. 3.4a show a trend in $n_{\text{ice}}(R)$ towards smaller bubbles for ice with higher bubble pressures, while the isothermally expanded bubble size distributions $n_{\text{iso}}(R)$ in Fig. 3.4 are relatively similar among all blocks of ice. This suggests that the bubble size distribution upon the formation of the bubbles in the ice is roughly consistent, and the bubbles then are compressed by the overburden pressure of ice above as it moves through the glacier. This is also consistent with observations of mean bubble pressures (Gow, 1968, 1971; Gow and Williamson, 1975) and bubble size distributions (Lipenkov, 1968; Bendel et al., 2013; Narita et al., 1999) from ice cores that are generally drilled in accumulation zones . However, Scholander and Nutt (1960) failed to observe a correlation between bubble size and bubble

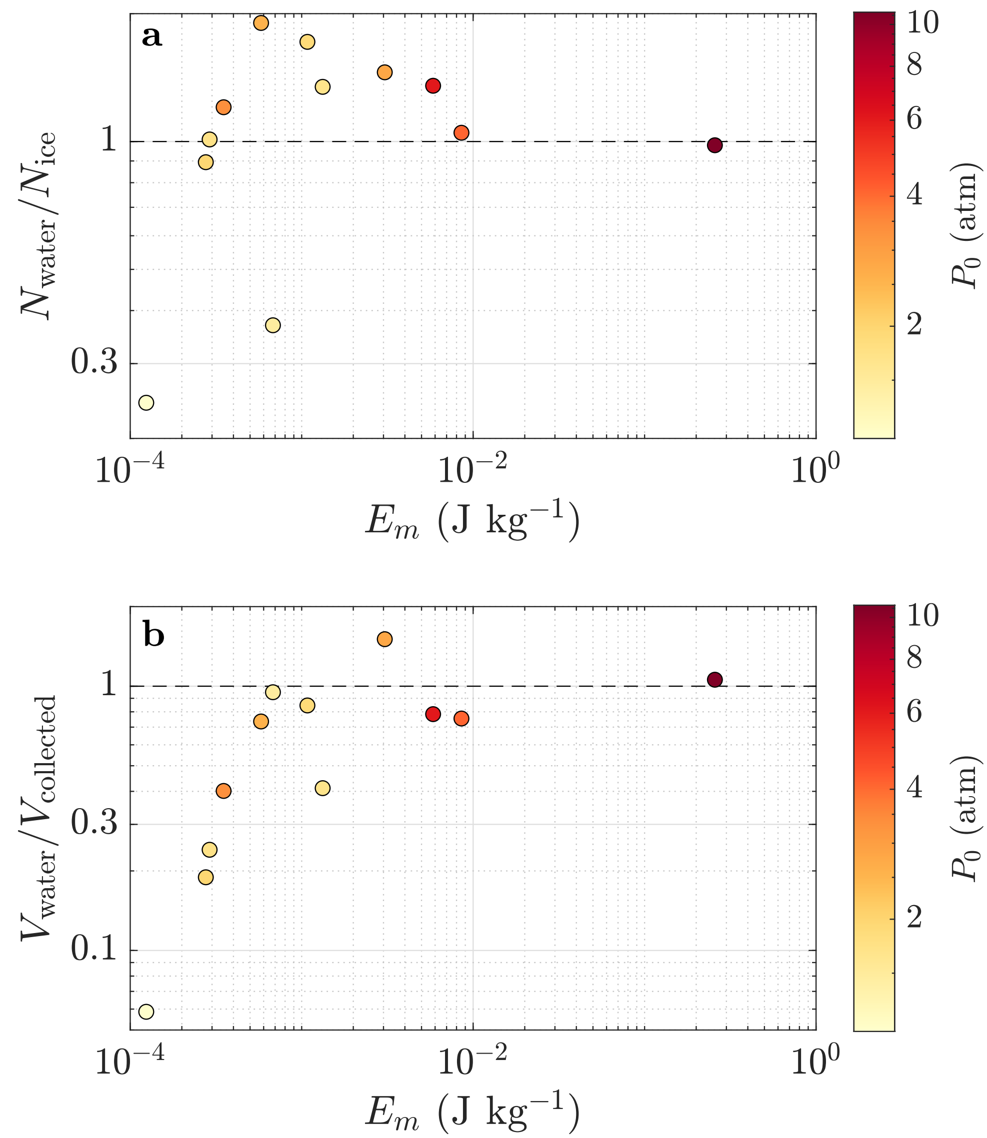

Figure 3.8. a Ratio of the total number of bubbles in the water per unit mass of ice melted, N_{water}, divided by the total number of bubbles per unit mass in the ice, N_{ice}. Each point represents a block of ice that was melted and its adjacent analyzed image. If every bubble in the ice is released into the water as a single bubble, and is successfully detected and recognized in the acoustic data, then this ratio will have a value of $N_{\text{water}}/N_{\text{ice}} = 1$. Values of $N_{\text{water}}/N_{\text{ice}} > 1$ suggest that at least some bubbles in the ice are released into the water as multiple smaller bubbles. Values of $N_{\text{water}}/N_{\text{ice}} < 1$ suggest that the acoustic technique is undercounting the bubbles in the water. **b** Ratio of the total volume of gas at $P_{\text{inf}} \approx P_{\text{atm}}$ contained in the bubbles in the water inferred from the acoustic measurements, V_{acoustic}, divided by the total volume of gas at P_{atm} released from the ice collected by the funnel. A ratio of $V_{\text{acoustic}}/V_{\text{collected}} = 1$ suggests that the acoustic technique is successfully measuring all of the bubbles released from the ice. A ratio of $V_{\text{acoustic}}/V_{\text{collected}} < 1$ suggests that some bubbles are released too quietly to be measured by the acoustic technique.

pressure in their measurements of bubble pressures in Greenlandic icebergs. We hypothesize that this may be because that study relied on measurements of individual bubbles, and the variability in pressure between individual bubbles may be large enough to obscure trends in average pressure that become apparent in our estimates based on thousands of bubbles each. The technique used by Scholander and Nutt (1960) also allowed only for the measurements of bubbles immediately adjacent to the ice face, which may be subject to the loss of gas through small cracks, as the authors themselves noted, or to pressure melting as a result of exposure to sunlight, as described by Bader (1950).

The acoustic technique presented in this study for determining bubble size distributions in the water has limitations, but, perhaps unsurprisingly, it performs well for louder blocks of ice in particular. Despite the clear tendency to undercount bubbles released from quieter blocks of ice, the results suggest that the bubbles released from quieter blocks of ice are more likely to end up as multiple smaller bubbles in the water. The relatively consistent ratio of $N_{\text{water}}/N_{\text{ice}} > 1$ for many of the blocks suggests that this is at least in part due to the slow release of streams of small bubbles from the ice. However, it is also possible that fragmentation into multiple small bubbles that are still released simultaneously contributes to this observed trend.

The findings that the size distribution of bubbles released from melting ice into the water a) can differ from that predicted by simple adiabatic expansion of the size distribution in the ice and b) can vary depending on the properties of the ice has implications for any attempt to describe the influence of bubbles on submarine melting at vertical termini of tidewater glaciers. In the context of the findings of Kitagawa et al. (2009) that a shift in bubble size distributions towards smaller bubbles rising along a heated plate in water results in increased heat transport, our results suggest that the influence of bubbles on submarine melt rates described by Wengrove et al. (2023) may vary, even between pieces of ice with bubble similar size distributions in the ice. A model of the the modification of the size distribution of the bubbles upon their release from the ice would be required in order to reliably predict the influence of the bubbles on melt rate.

The results presented here, and in Chapter 2, suggest a possible path forward to a predictive model, with some challenges that remain to be addressed. Since the modification of the bubble size distributions is linked to the acoustic energy radiated by the ice, predicting this modification is linked to predictions of the acoustic energy. The results of Chapter 2 suggest that considering the gas pressure and energy stored in the bubbles in the ice can explain some of this variability, but not all of it. Blocks of ice with similar bubble pressures and potential energies can behave differently, with a varying fraction of their bubbles released rapidly or slowly. The rapid release of a bubble in the ice is more likely to result in a single bubble in the water, while the slow release of a bubble in the ice is more likely to result in a stream of many smaller bubbles. More work on the relationship between the microcrystalline structure of the ice and the ways in which bubbles are released from the ice as it melts is needed in order to reliably predict resulting bubble size distributions in the water. More work is also required to quantify the impact of this shift in bubble size distribution on the enhancement of melting by bubbles in the water.

3.5 Conclusion

As glacier ice melts, the bubbles in the ice are released into the water, but the size distribution of the bubbles in the water is not the same as the size distribution in the ice. In addition to the expansion of the bubbles due to their internal pressure, some of the bubbles in the ice may be released into the water as many smaller bubbles. This can result in more smaller bubbles, and fewer large ones, in the water than expected based on simple expansion of the bubbles in the ice. The fraction of bubbles in the ice which turn into multiple smaller bubbles in the water also varies between blocks of ice. For louder blocks of ice with higher pressure, most bubbles in the ice are released into the water as a single bubble, while quieter blocks of ice with lower bubble pressures have more bubbles that are released into the water as many smaller bubbles. This variability in the size distribution of the bubbles in the water is expected to alter the impact that the bubbles have on the rate of submarine melting at vertical tidewater glacier termini.

3.6 Acknowledgements

This work was supported by Office of Naval Research Ocean Acoustics Division, Grant Nos. N00014-24-1–2394 and N00014-21-1-2316, the National Science Centre, Poland (grant 2021/43/D/ST10/00616), the Institute of Geophysics, Polish Academy of Sciences Grant 2a/IGF PAN/2017, and a subsidy for the Institute of Geophysics, Polish Academy of Sciences provided by the Ministry of Science and Higher Education of Poland. All data collection was staged at the Polish Polar Station, which is owned and operated by the Institute of Geophysics at the Polish Academy of Sciences. The color maps used in this publication were developed by Cynthia Brewer (http://colorbrewer.org) and ported to MATLAB by Scott Lowe (Lowe, 2016).

This chapter is in preparation for submission to AGU's *Geophysical Research Letters* with H. A. Johnson, G. B. Deane, M. D. Stokes, O. Glowacki, M. Moskalik, M. Chitre, and H. Vishnu as co-authors. The dissertation author was the primary investigator and author of this paper.

Conclusion

The chapters of this thesis have all been focused on the study of small-scale processes at the ice-water boundary of tidewater glaciers. However, they are somewhat disparate in terms of both their approach and content. Chapter 1 presented a new technique for making measurements at the ice-water boundary of small floating pieces of ice in glacial fjords. Chapter 2 presented a theory- and model-based description of the energy available to be radiated as sound from melting glacier ice, and demonstrated that it serves as an upper bound for the actual acoustic energy radiated and explains some, but not all, of the variability in this energy. Chapter 3 presented observations of the transformation of bubble size distribution that occurs as glacier ice melts and the bubbles are released into the water, and demonstrated that this modification varies depending on the state of the ice.

There are several possible directions for future work suggested by the results presented here. In terms of observational techniques for making in-situ measurements at the ice-water boundary, the next logical step is to increase the sophistication of instrumentation to include measurements of water velocity and salinity, and ideally direct measurements of submarine melting. Though the results have not been presented here, we have made some initial attempts to make these types of measurements with the ice frame. However, further refinement is necessary in order to reduce the experimental errors and uncertainty in those measurements. It would also be advantageous to move from manual deployment to a robotically deployed system that would allow for larger icebergs, and eventually the terminus itself, to be studied. Indeed, progress has already been made on this front by Nash et al. (2024).

The results of Chapters 2 and 3 have both established the need for further investigation into the effect of the microcrystalline structure of glacier ice on the way in which bubbles are released from the ice. The results of Chapter 2 suggest that variations in microscopic properties of the ice result in changes in the acoustic energy radiated by the ice as it melts. This complicates efforts to use melt noise to measure submarine melting, and has implications for variation in the ambient soundscape near tidewater glacier termini. The results of Chapter 3 suggest that these variations in ice microcrystalline structure may also mediate the transformation of the bubble size distribution upon release into the water, and influence heat flux across the boundary and submarine melt rates.

Bibliography

Allen, J. B. and Berkley, D. A. (1979). Image method for efficiently simulating small-room acoustics. *The Journal of the Acoustical Society of America*, 65(4):943–950.

Bader, H. (1950). The significance of air bubbles in glacier ice. *Journal of Glaciology*, 1(8):443–451.

Bendel, V., Ueltzhöffer, K. J., Freitag, J., Kipfstuhl, S., Kuhs, W. F., Garbe, C. S., and Faria, S. H. (2013). High-resolution variations in size, number and arrangement of air bubbles in the epica dml (antarctica) ice core. *Journal of Glaciology*, 59(217):972–980.

Cenedese, C. and Straneo, F. (2023). Icebergs melting. *Annual Review of Fluid Mechanics*, 55.

Chen, J., Cazenave, A., Dahle, C., Llovel, W., Panet, I., Pfeffer, J., and Moreira, L. (2022). Applications and challenges of grace and grace follow-on satellite gravimetry. *Surveys in Geophysics*, 43(1):305–345.

Cowton, T., Slater, D., Sole, A., Goldberg, D., and Nienow, P. (2015). Modeling the impact of glacial runoff on fjord circulation and submarine melt rate using a new subgrid-scale parameterization for glacial plumes. *Journal of Geophysical Research: Oceans*, 120(2):796–812.

Davis, P. E., Nicholls, K. W., Holland, D. M., Schmidt, B. E., Washam, P., Riverman, K. L., Arthern, R. J., Vaňková, I., Eayrs, C., Smith, J. A., et al. (2023). Suppressed basal melting in the eastern thwaites glacier grounding zone. *Nature*, 614(7948):479–485.

Davison, B., Cowton, T., Cottier, F. R., and Sole, A. (2020). Iceberg melting substantially modifies oceanic heat flux towards a major greenlandic tidewater glacier. *Nature communications*, 11(1):5983.

Deane, G. B., Glowacki, O., Stokes, M. D., and Pettit, E. C. (2019). The underwater sounds of glaciers. *Acoust. Today*, 15(4):12–19.

Gayen, B., Griffiths, R. W., and Kerr, R. C. (2016). Simulation of convection at a vertical ice face dissolving into saline water. *Journal of Fluid Mechanics*, 798:284–298.

Glowacki, O., Deane, G. B., and Moskalik, M. (2018). The intensity, directionality, and statistics of underwater noise from melting icebergs. *Geophysical Research Letters*, 45(9):4105–4113.

Gow, A. J. (1968). Bubbles and bubble pressures in antarctic glacier ice. *Journal of Glaciology*, 7(50):167–182.

Gow, A. J. (1971). Relaxation of ice in deep drill cores from antarctica. *Journal of Geophysical Research*, 76(11):2533–2541.

Gow, A. J. and Williamson, T. (1975). Gas inclusions in the antarctic ice sheet and their glaciological significance. *Journal of Geophysical Research*, 80(36):5101–5108.

Grossman, S., Johnson, H., Stokes, D., and Deane, G. (2024). Toward monitoring submarine glacier melt using hydroacoustics: The role of timescale in the signal of bubble release. *The Journal of the Acoustical Society of America*, 156(3):1820–1838.

Hellmer, H. H. and Olbers, D. J. (1989). A two-dimensional model for the thermohaline circulation under an ice shelf. *Antarctic Science*, 1(4):325–336.

Herrero, S. (2018). *Bear attacks: their causes and avoidance*. Rowman & Littlefield.

Holland, D. M. and Jenkins, A. (1999). Modeling thermodynamic ice–ocean interactions at the base of an ice shelf. *Journal of physical oceanography*, 29(8):1787–1800.

IPCC (2021). *Climate Change 2021: The Physical Science Basis. Contribution of Working Group I to the Sixth Assessment Report of the Intergovernmental Panel on Climate Change*, volume In Press. Cambridge University Press, Cambridge, United Kingdom and New York, NY, USA.

Jackson, R., Nash, J., Kienholz, C., Sutherland, D., Amundson, J., Motyka, R., Winters, D., Skyllingstad, E., and Pettit, E. (2020). Meltwater intrusions reveal mechanisms for rapid submarine melt at a tidewater glacier. *Geophysical Research Letters*, 47(2):e2019GL085335.

Jackson, R. H., Motyka, R. J., Amundson, J. M., Abib, N., Sutherland, D. A., Nash, J. D., and Kienholz, C. (2022). The relationship between submarine melt and subglacial discharge from observations at a tidewater glacier. *Journal of Geophysical Research: Oceans*, 127(10):e2021JC018204.

Jenkins, A. (2011). Convection-driven melting near the grounding lines of ice shelves and tidewater glaciers. *Journal of Physical Oceanography*, 41(12):2279–2294.

Jenkins, A., Dutrieux, P., Jacobs, S. S., McPhail, S. D., Perrett, J. R., Webb, A. T., and White, D. (2010). Observations beneath pine island glacier in west antarctica and implications for its retreat. *Nature Geoscience*, 3(7):468–472.

Josberger, E. G. (1980). The effect of bubbles released from a melting ice wall on the melt-driven convection in salt water. *Journal of Physical Oceanography*, 10(3):474–477.

Kitagawa, A., Uchida, K., and Hagiwara, Y. (2009). Effects of bubble size on heat transfer enhancement by sub-millimeter bubbles for laminar natural convection along a vertical plate. *International Journal of Heat and Fluid Flow*, 30(4):778–788.

Lee, K. M., Wilson, P. S., and Pettit, E. C. (2013). Underwater sound radiated by bubbles released by melting glacier ice. In *Proceedings of Meetings on Acoustics*, volume 20. AIP Publishing.

Leighton, T. G. (1994). *The acoustic bubble*. Academic press.

Lipenkov, V. Y. (1968). Air bubbles and air-hydrate crystals in the vostok. *Science*, 161:1011.

Longuet-Higgins, M. S. (1989a). Monopole emission of sound by asymmetric bubble oscillations. part 1. normal modes. *Journal of Fluid Mechanics*, 201:525–541.

Longuet-Higgins, M. S. (1989b). Monopole emission of sound by asymmetric bubble oscillations. part 2. an initial-value problem. *Journal of Fluid Mechanics*, 201:543–565.

Lowe, S. (2016). cbrewer2. https://github.com/scottclowe/cbrewer2.

Lydersen, C., Assmy, P., Falk-Petersen, S., Kohler, J., Kovacs, K. M., Reigstad, M., Steen, H., Strøm, H., Sundfjord, A., Varpe, Ø., et al. (2014). The importance of tidewater glaciers for marine mammals and seabirds in svalbard, norway. *Journal of Marine Systems*, 129:452–471.

McConnochie, C. and Kerr, R. (2017). Testing a common ice-ocean parameterization with laboratory experiments. *Journal of Geophysical Research: Oceans*, 122(7):5905–5915.

McCutchan, A. L. and Johnson, B. A. (2022). Laboratory experiments on ice melting: A need for understanding dynamics at the ice-water interface. *Journal of Marine Science and Engineering*, 10(8):1008.

Minnaert, M. (1933). Xvi. on musical air-bubbles and the sounds of running water. *The London, Edinburgh, and Dublin Philosophical Magazine and Journal of Science*, 16(104):235–248.

Narita, H., Azuma, N., Hondoh, T., Fujii, M., Kawaguchi, M., Mae, S., Shoji, H., Kameda, T., and Watanabe, O. (1999). Characteristics of air bubbles and hydrates in the dome fuji ice core, antarctica. *Annals of Glaciology*, 29:207–210.

Nash, J. D., Weiss, K., Wengrove, M. E., Osman, N., Pettit, E. C., Zhao, K., Jackson, R. H., Nahorniak, J., Jensen, K., Tindal, E., et al. (2024). Turbulent dynamics of buoyant melt plumes adjacent near-vertical glacier ice. *Geophysical Research Letters*, 51(9):e2024GL108790.

Nayar, K. G., Panchanathan, D., McKinley, G., and Lienhard, J. (2014). Surface tension of seawater. *Journal of Physical and Chemical Reference Data*, 43(4).

Nayar, K. G., Sharqawy, M. H., Banchik, L. D., et al. (2016). Thermophysical properties of seawater: A review and new correlations that include pressure dependence. *Desalination*, 390:1–24.

Nicholls, R. J. and Cazenave, A. (2010). Sea-level rise and its impact on coastal zones. *science*, 328(5985):1517–1520.

Pettit, E. C., Lee, K. M., Brann, J. P., Nystuen, J. A., Wilson, P. S., and O'Neel, S. (2015). Unusually loud ambient noise in tidewater glacier fjords: A signal of ice melt. *Geophysical Research Letters*, 42(7):2309–2316.

Poulsen, E., Eggertsen, M., Jepsen, E. H., Melvad, C., and Rysgaard, S. (2022). Lightweight drone-deployed autonomous ocean profiler for repeated measurements in hazardous areas–example from glacier fronts in ne greenland. *HardwareX*, 11:e00313.

Prosperetti, A. (1977). Thermal effects and damping mechanisms in the forced radial oscillations of gas bubbles in liquids. *The Journal of the Acoustical Society of America*, 61(1):17–27.

Risch, D., Clark, C. W., Corkeron, P. J., Elepfandt, A., Kovacs, K. M., Lydersen, C., Stirling, I., and Van Parijs, S. M. (2007). Vocalizations of male bearded seals, erignathus barbatus: classification and geographical variation. *Animal Behaviour*, 73(5):747–762.

Rosevear, M. G., Gayen, B., and Galton-Fenzi, B. K. (2022). Regimes and transitions in the basal melting of antarctic ice shelves. *Journal of Physical Oceanography*, 52(10):2589–2608.

Rosevear, M. G., Gayen, B., Vreugdenhil, C. A., and Galton-Fenzi, B. K. (2024). How does the ocean melt antarctic ice shelves? *Annual Review of Marine Science*, 17.

Rubinštein, L. (1971). The stefan problem, volume 27 of translations of mathematical monographs. *American Mathematical Society, Rhode Island*.

Schmidt, B. E., Washam, P., Davis, P. E., Nicholls, K. W., Holland, D. M., Lawrence, J. D., Riverman, K. L., Smith, J. A., Spears, A., Dichek, D., et al. (2023). Heterogeneous melting near the thwaites glacier grounding line. *Nature*, 614(7948):471–478.

Scholander, P. and Nutt, D. (1960). Bubble pressure in greenland icebergs. *Journal of Glaciology*, 3(28):671–678.

Schulz, K., Nguyen, A., and Pillar, H. (2022). An improved and observationally-constrained melt rate parameterization for vertical ice fronts of marine terminating glaciers. *Geophysical Research Letters*, 49(18):e2022GL100654.

Slater, D., Straneo, F., Das, S., Richards, C., Wagner, T., and Nienow, P. (2018). Localized plumes drive front-wide ocean melting of a greenlandic tidewater glacier. *Geophysical Research Letters*, 45(22):12–350.

Slater, D. A., Goldberg, D. N., Nienow, P. W., and Cowton, T. R. (2016). Scalings for submarine melting at tidewater glaciers from buoyant plume theory. *Journal of Physical Oceanography*, 46(6):1839–1855.

Slater, T., Hogg, A. E., and Mottram, R. (2020). Ice-sheet losses track high-end sea-level rise projections. *Nature Climate Change*, 10(10):879–881.

Straneo, F. and Cenedese, C. (2015). The dynamics of greenland's glacial fjords and their role in climate. *Annual review of marine science*, 7(1):89–112.

Strasberg, M. (1953). The pulsation frequency of nonspherical gas bubbles in liquids. *The Journal of the Acoustical Society of America*, 25(3):536–537.

Sutherland, D., Jackson, R. H., Kienholz, C., Amundson, J. M., Dryer, W., Duncan, D., Eidam, E., Motyka, R., and Nash, J. (2019). Direct observations of submarine melt and subsurface geometry at a tidewater glacier. *Science*, 365(6451):369–374.

Urick, R. (1971). The noise of melting icebergs. *The Journal of the Acoustical Society of America*, 50(1B):337–341.

Vazquez, A., Sanchez, R., Salinas-Rodriguez, E., Soria, A., and Manasseh, R. (2005). A look at three measurement techniques for bubble size determination. *Experimental thermal and fluid science*, 30(1):49–57.

Velicogna, I. (2009). Increasing rates of ice mass loss from the greenland and antarctic ice sheets revealed by grace. *Geophysical Research Letters*, 36(19).

Vishnu, H., Chitre, M., Glowacki, O., Stokes, D. M., Johnson, H. A., Moskalik, M., and Deane, G. B. (2025). Acoustic activity indicates submarine melt at tidewater glaciers. Accepted for publication at *Journal of Glaciology*.

Vishnu, H., Deane, G. B., Chitre, M., Glowacki, O., Stokes, D., and Moskalik, M. (2020). Vertical directionality and spatial coherence of the sound field in glacial bays in hornsund fjord. *The Journal of the Acoustical Society of America*, 148(6):3849–3862.

Vishnu, H., Deane, G. B., Glowacki, O., Chitre, M., Johnson, H., Moskalik, M., and Stokes, D. (2023). Depth-dependence of the underwater noise emission from melting glacier ice. *JASA Express Letters*, 3(2).

Washam, P., Lawrence, J. D., Stevens, C. L., Hulbe, C. L., Horgan, H. J., Robinson, N. J., Stewart, C. L., Spears, A., Quartini, E., Hurwitz, B., et al. (2023). Direct observations of melting, freezing, and ocean circulation in an ice shelf basal crevasse. *Science Advances*, 9(43):eadi7638.

Wells, A. J. and Worster, M. G. (2008). A geophysical-scale model of vertical natural convection boundary layers. *Journal of Fluid Mechanics*, 609:111–137.

Wells, A. J. and Worster, M. G. (2011). Melting and dissolving of a vertical solid surface with laminar compositional convection. *Journal of fluid mechanics*, 687:118–140.

Wengrove, M. E., Pettit, E. C., Nash, J. D., Jackson, R. H., and Skyllingstad, E. D. (2023). Melting of glacier ice enhanced by bursting air bubbles. *Nature Geoscience*, 16(10):871–876.

Zeh, M. C., Wilson, P. S., Lee, K. M., and Pettit, E. C. (2018). Acoustical characteristics and contributions of bubbles released from melting glacier ice. *The Journal of the Acoustical Society of America*, 143(3_Supplement):1832–1832.